The Dissertation Committee for Elisa Talcott Novelli Certifies that this is the approved version of the following Dissertation:

Measuring Electrostatics in Complex Protein Systems Using Vibrational Stark Effect Spectroscopy

Committee:

Lauren J. Webb, Supervisor

Carlos R. Baiz

Jennifer S. Brodbelt

Richard M. Crooks

Jennifer A. Maynard

Measuring Electrostatics in Complex Protein Systems Using Vibrational Stark Effect Spectroscopy

by

Elisa Talcott Novelli

Dissertation

Presented to the Faculty of the Graduate School of

The University of Texas at Austin

in Partial Fulfillment

of the Requirements

for the Degree of

Doctor of Philosophy

The University of Texas at Austin

May 2019

Dedication

For Ann Talcott Davis Bradley and Frances Marie Colameco Novelli

Acknowledgements

I would first like to acknowledge the laboratory staff in the mass spectrometry, proteomics, and DNA sequencing core facilities for their services enabling the research in this dissertation. I would like to especially thank the staff of the Texas Therapeutic Drug and Diagnostic Development Program for their instrumentation and advice in the development of the kinetic assays used in this research, especially John Veloria, who was very patient and full of good ideas.

Additionally, I would like to thank my dissertation committee, Dr. Carlos Baiz, Dr. Jennifer Brodbelt, Dr. Richard Crooks, and Dr. Jennifer Maynard, for their helpful discussions throughout the course of my graduate career. I have also had wonderful high school and undergraduate mentors who encouraged me to pursue chemistry early on. My high school chemistry teachers, Dr. Scott Best, and Derrick Wood, who gave me unprecedented opportunities (and free reign of their labs) to explore my chemistry interests. Dr. Linda McGown and Dr. Jim Kempf, my undergraduate research mentors at Rensselaer Polytechnic Institute, provided early research opportunities in biophysical and bioanalytical chemistry. I am truly grateful for the encouragement of all of these mentors.

Most importantly, I would like to thank my advisor, Dr. Lauren Webb, for her mentorship over the last six years. I am extremely grateful for her constant patience, support, and encouragement. There were several times during graduate school when I was close to giving up on projects, but ten minutes in her office discussing the challenges of the work left me with renewed motivation and many new ideas. I am indebted to my co-authors Jeremy First and Chris Crittenden, who were excellent collaborators, writing partners, and friends. In particular, Jeremy's efforts in computational modeling have been

a crucial component of the research presented in this dissertation. I would also like to thank the undergraduates who assisted me in research throughout my graduate career, Ben Chang, Lisa Strong, and Danielle Landry. They have taught me a great deal about mentorship and have been a genuine joy to work with over the past several years. My success in graduate school would not have been possible without the support of the entire Webb Group. In particular, I would like to thank Cari Anderson, Whitney Fies, and Josh Slocum for their support and friendship from the beginning, and without whom I would have never made it to the end.

I owe everything to my parents, John Novelli and Susan Bradley, for their endless support, as well as my sister, Ann Novelli, for being my oldest and best friend; without them, none of this would be possible. I would also like to thank my extended family for supporting my pursuit of higher education even though they did not necessarily understand it, as well as Kayla Sandler, Katherine Law, and Kiley Bense: friends who have been around long enough to be considered my extended family and were there to commiserate about higher education.

Finally, I thank John and Paxton Emery for sticking by me in the past, present, and future.

Abstract

Measuring Electrostatics in Complex Protein Systems Using Vibrational Stark Effect Spectroscopy

Elisa Talcott Novelli, Ph.D.

The University of Texas at Austin, 2019

Supervisor: Lauren J. Webb

The non-covalent interactions between and within proteins are important because of their specificity and their ability to control protein structure and function. The measurement of electric fields, which describe these complex interactions, is crucial to understanding the physical properties of proteins such as folding, catalysis, and multimolecular interactions. Our goal is to understand and ultimately exploit these complex interactions for therapeutic value. In particular, our group has been interested in small GTPase signaling proteins, such as Ras, because of their known oncogenic properties, complex network of binding partner proteins, and their difficulty as a drug target. In particular the highly specific protein-protein interactions inherent in the signaling role of Ras and other GTPase proteins are interesting potential drug targets that could avoid the toxicity of competitive inhibition at the GTP binding site. To this end, we have made use of vibrational Stark effect spectroscopy, a technique that directly reports on electrostatic environment, to measure the electric fields in Ras and other GTPases by site-specifically incorporating small nitrile vibrational probes into proteins. We have related the quantitative field measurements to protein activity to elucidate the role of electric fields in the intrinsic

hydrolysis mechanism of oncogenic Ras mutants. We also designed experiments to investigate the role of electrostatics in driving specific protein-protein interactions and their inhibition by the small molecule Brefeldin A in the GTPase protein Arf. Finally, we developed the *Staphylococcus aureus* protein staphylococcal nuclease as a robust model system for experiments aimed at better understanding how pK_a and nitrile probes respond to their local electrostatic environment. Together, this work demonstrates the importance of electrostatic forces in protein function and highlights how vibrational Stark effect spectroscopy can be applied effectively to interesting and relevant protein systems to observe and exploit the physical properties of proteins for therapeutic benefit.

Table of Contents

List of Tables

List of Figures

Chapter 1: Introduction

Electrostatic interactions in proteins arise from the complex arrangement of thousands of whole and partially charged atoms distributed throughout the structure of the protein. The precise magnitude and orientation of these interactions are crucial for complex biological functions such as protein folding, stability, docking, substrate binding, and membrane association.[1] The complex network of these interactions, determined by protein structure, can be quantified as an electric field, which describes the direction and magnitude of the force experienced by a positive test charge at a specific point in space. The measurement of a protein's electrostatic environment, which is a sum of all of the complex fields generated by the distribution of charge throughout the protein structure, has been a long-standing challenge, a complete understanding of which could lead to better drug design, improved understanding of diseases, and the creation of more efficient engineered proteins.

Towards this goal, one strategy that has been used extensively to estimate electrostatic environment in proteins is the perturbation of pK_a values. In these experiments, the pK_a of an ionizable residue or group is measured in a protein and compared to the pK_a of that residue or group in water.[2-6] The electrostatic environment around the titratable residue strongly influences the relative stability of the charged side chain relative to the neutral side chain. The change in equilibrium between these two states is thought to be a good reporter of the average protein environment around the ionizable residue. However, while the electrostatic environment contributes to an observed pK_a shift, convoluting effects such as solvation free energy, hydrogen bonding, ion pairing, and other local effects can also contribute. It is very difficult to quantify or spatially resolve these effects.

More recently, Stark effect spectroscopy has allowed for the direct measurement of electric fields in proteins with high sensitivity and spatial resolution. This method results in quantitative parameters that describe the effects of non-covalent interactions that are difficult to capture with other bioanalytical methods. This dissertation describes our efforts using vibrational Stark effect spectroscopy to measure electric fields in proteins directly, relate electrostatic measurements to protein structure and function, and improve experimental methodologies for such measurements. This information is necessary to begin to modulate biological processes that are dependent on non-covalent interactions, such as targeting electrostatically disruptive protein mutants or drugging disease pathways that rely on protein-protein interactions. Furthermore, essential to this long-term goal are better computational models for predicting electrostatic environments of proteins *in silico*. Robust experimental datasets of electric fields are crucial for benchmarking computational electrostatic models, and to that end we compare our experimental measurements of electric field with computational models of electrostatics. This introduction provides the background information necessary to understand the context of our work.

1.1: Measuring Electrostatics with Vibrational Stark Effect Spectroscopy

Central to our work is a useful method for measuring electrostatic effects in proteins: vibrational Stark effect (VSE) spectroscopy. The Stark effect, or electrochromic effect, is a phenomenon across the entire electromagnetic spectrum that describes the sensitivity of spectroscopic transitions to the local electrostatic environment of the chromophore. In principle, the change in energy of a chromophore transition in response to an electric field can be expressed as a Taylor expansion about the applied field as shown in equation 1.1:

$$E = -(\Delta\vec{\mu} \bullet \vec{F} + \Delta\alpha \bullet \vec{F} \bullet \Delta\alpha + \ldots) \qquad \text{[Equation 1.1]}$$

where E is the absorption energy of the transition, $\Delta\vec{\mu}$ is the difference between the ground and excited state dipole moments of the chromophore (called the difference dipole moment or Stark tuning rate), $\vec{F}$ is the applied electric field, and $\Delta\alpha$ is the change in polarizability due to the spectroscopic transition. $\Delta\vec{\mu}$ and $\Delta\alpha$ are material properties of specific probes and can be measured by calibrating the energy of transitions when a known field is applied.[7, 8] These values have been reported for a wide range of probes whose transitions occur over several regions of the electromagnetic spectrum.[9-15]

Small vibrational probes, such as nitrile, carbonyl, and azide groups, are commonly used for VSE because they offer several advantages: 1) for these probes, the Taylor series describing the Stark effect can be simplified to only the first term because there is a negligible change in polarizability,[16, 17] and 2) these probes are smaller and more biologically compatible with protein systems than larger molecules that experience electronic transitions.[18] Additionally, by irradiating in the infrared region, we can preserve delicate biological samples that could be damaged with the visible or ultraviolet light required for Stark probes that undergo higher energy electronic transitions, such as fluorescent dyes. Nitriles in particular, which are used in the work presented here, make convenient vibrational Stark probes because they: 1) have relatively large $\Delta\vec{\mu}$ values (0.4 - 0.8 cm^{-1} / MV cm^{-1}) which describe the shift in absorption energy in wavenumbers per unit of applied field, 2) have large absorptivities ($\epsilon \sim 500$ M^{-1} cm^{-1}), and 3) absorb in a transparent portion of the protein infrared spectrum ($\nu_{CN} \sim 2100$ -2400 cm^{-1}). [19, 20]

Once the Stark tuning rate is characterized, changes to the absorption energy of the transition can be related to field for probes in which $\Delta\alpha$ is negligible, such as nitriles, through the simplified linear Stark equation as shown in equation 1.2:

$$\Delta E = hc\Delta\nu = -\Delta\vec{\mu} \bullet \Delta\vec{F} \qquad \text{[Equation 1.2]}$$

where ΔE is the change in absorption energy of the vibrational transition and $\Delta\vec{F}$ is the change in electric field. Generally, this relationship is used to describe changes in field due to some biological event or perturbation such as an amino acid mutation, ligand binding, or protein-protein docking as described in Figure 1.1. The shift between the reference spectrum and the perturbed spectrum, $\Delta\nu$, is linearly related to the difference in field resulting from the perturbation through $\Delta\vec{\mu}$. An important consideration here is the dot product relationship between $\Delta\vec{\mu}$ and $\Delta\vec{F}$. To quantitatively measure field, structural data describing the orientation of the nitrile bond axis is necessary and can be estimated through a variety of methods. This is typically achieved through MD simulations, though crystal structures of probe-containing systems could also be used.

Occasionally, protein systems contain a useful native Stark probe.[9, 14, 21-23] In the absence of a native chromophore, however, VSE spectroscopy requires a non-native chromophore to be placed site-specifically in the system of interest. Several strategies are available to incorporate vibrational Stark probes into proteins. For carbonyl vibrational Stark probes, it is common to use isotope editing strategies to produce an isotope-labeled $C^{13}=O^{18}$ vibrational Stark probe or to label with metal-carbonyl complexes, either of which is required to distinguish the desired probe from the many other native carbonyl groups in proteins.[11, 24] Nitriles, which are not found natively in proteins, do not require isotope labeling and can be incorporated in proteins in several ways. Previous work in our group has succeeded in placing nitrile probes in proteins and peptides at the time of synthesis, either synthetically in the case of peptides or with nonsense suppression strategies in the recombinant *E. coli* expression of proteins.[25, 26] Nitrile probes can also be placed after proteins are expressed and purified by chemically modifying existing amino acids.

The work in this dissertation made use of a strategy devised by Fafarman et al. in which site-specifically placed cysteine residues were post-translationally modified to

thiocyanate groups according to the reaction in Figure 1.2.[27] The thiol group of the cysteine residue is first reacted with 5,5'-dithiobis-[2-nitrobenzoic acid] (DTNB) in a substitution reaction which results in a thionitrobenzoate (TNB-) leaving group attaching to the protein with a disulfide bond. The leaving group can then be displaced with potassium cyanide resulting in a thiocyanate Stark probe in the location of the cysteine residue. This strategy requires only simple modification of the codon of the wild type (WT) residue to the codon for a cysteine residue on the gene of a chosen protein with routine mutagenesis methodologies. The labeling reaction proceeds completely at room temperature in several hours and can be performed on protein that has already been purified. It is, therefore, the most expedient way to label cysteines which are solvent exposed in folded protein. Constructs in which the cysteine is not completely available to solvent can be labeled by first unfolding the protein with urea-containing buffer, performing the labeling reaction, and then refolding the protein during buffer exchange or dialysis back into the original buffer. For stable proteins, this can be accomplished with minimal loss of protein due to misfolding. Thus, the post-translational modification of cysteines to thiocyanates can be accomplished for both solvent-accessible and buried probe locations.

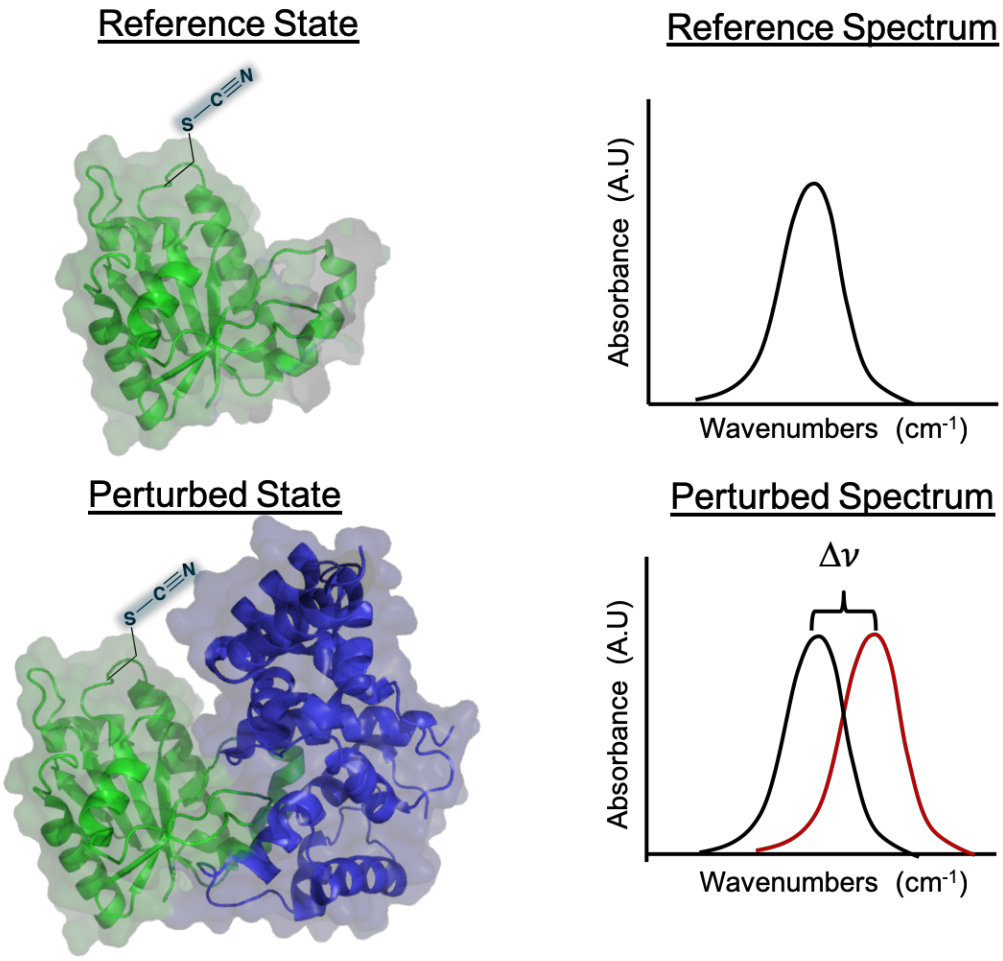

Figure 1.1: Cartoon of docking VSE experiment in which the reference state is a protein monomer and the perturbed state is the protein docked to a downstream effector. The shift between the reference spectrum and the perturbed spectrum, $\Delta\nu$, is related to $\Delta\vec{F}$ through eq. 1.2. Figure adapted from ref 20.

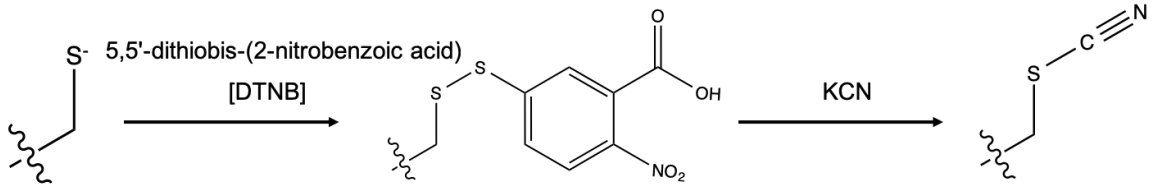

Figure 1.2: Scheme describing the labeling of a cysteine residue with a nitrile label producing cyanocysteine through two successive S_N2 reactions according to ref 27.

Several notable efforts to measure electric field with the VSE have been made using nitrile probes. One of the earliest examples used *p*-cyanophenylalanine as a label on calmodulin binding peptide to observe the vibrational spectra of the nitrile group before and after the peptide was bound to calmodulin.[28] Much of the previous work involving proteins in our group was based on observing electrostatic changes resulting from the docking of GTPase proteins with downstream effectors.[29-31] This effort is expanded upon in Chapter 5 of this dissertation. Nitrile VSE probes have also been used to observe electric fields at enzyme active sites. Boxer and coworkers have measured electric fields in the active site of human aldose reductase, by using native and synthetic nitrile probes on ligands.[15] More recent work in our group interrogated the active site of a GTPase protein with a nitrile probe positioned on a partner protein across the protein-protein interface aimed towards the GTP binding site and observed changes in the electric field due to known oncogenic mutations in the active site.[32] Aside from its use in proteins, further work in our group is concerned with using VSE spectroscopy to interrogate the electric field and resulting organization of lipid bilayer membranes.[25, 33]

In spite of recent progress made in the development of VSE spectroscopy with nitrile probes, the interpretation of changes in nitrile absorption energy in a biological system is somewhat complicated by the fact that the nitrogen atom in the nitrile group is capable of accepting a hydrogen bond. Hydrogen bonds are not well-described by the Stark equation because the hydrogen bond changes the force constant of the nitrile by withdrawing electron density from either the bonding or anti-bonding orbitals, which changes the bond order and the bond length. This can result in a higher or lower frequency (blue or red shift) that is unrelated to the dipole moment of the probe. Thus, any quantitative interpretation of a nitrile's absorption energy shift is convoluted by the presence of hydrogen bonding.[34-36] There has been considerable debate in the field about the

appropriate level of interpretation of nitrile frequency shifts. Arguments include, 1) considering hydrogen bonding as an additive effect,[37] 2) discounting any electrostatic interpretation and only interpreting nitrile shifts in proteins as reporters of solvent exposure due to their sensitivity to hydrogen bonding and the prevalence of such interactions in biological systems,[36, 38] and 3) rejecting any use of nitrile probes because of potential changes to hydrogen bonding networks upon the incorporation of a non-native probe. Previous work in our group has made efforts toward deconvoluting the two effects, and we have reported both *in vitro* and *in silico* strategies for quantifying hydrogen bonding to nitrile probes. We have shown that fixed charge force fields can report hydrogen bonding quantitatively through an estimation of solvent accessible surface area (SASA) or a simple count of hydrogen bonding interactions through the course of a trajectory. Experimentally, Adhikary et al. have demonstrated an empirical relationship between the red-shifting of nitrile peaks with increasing temperature and the amount of hydrogen bonding experienced by the probe. This is due to the more frequent exchange of hydrogen bonds as the temperature of the system increases. Our group has shown that this relationship, the frequency temperature line slope (FTLS), can quantitatively report the amount of hydrogen bonding experienced by a nitrile probe. These two strategies are instrumental in deconvoluting the effects of hydrogen bonding from the Stark effect in vibrational spectroscopy. As such, an analysis of hydrogen bonding to the probe, accomplished with MD simulations and experimental FTLS, is discussed in many of the systems described in this dissertation.

1.2: Oncogenic GTPase Proteins

An important protein of interest to us because of its oncogenic properties is H-Ras, the canonical member of the Ras superfamily. The Ras superfamily is a collection of more

than 150 small (~20kDa) GTPase proteins that function as molecular switches that turn on or off cellular signaling processes.[39] The superfamily, named for the canonical member Ras, contains several subfamilies that are distinguished from one another by structure and post-translational modifications, which result in their localization to different organelles.[40] All members of the Ras superfamily contain a conserved set of GTP/GDP binding motifs and which reorganize upon conversion from the GTP bound state to the GDP bound state and vice versa. This reorganization of protein structure either prevents or allows the protein to bind to effectors and perform signaling functions through their interactions with a vast network of other proteins in the cell.[41] The catalytic cycle is shown in Figure 1.3. Ras superfamily GTPase proteins are bound to GTP in the ON state, where their structures are oriented so they can interact with other downstream effector proteins which signal for specific cellular functions. Upon hydrolysis of GTP to GDP, either by the GTPases alone or with the assistance of GTPase activating proteins (GAPs), they undergo a structural change to convert to the GDP-bound OFF state, in which no signaling occurs. Partner proteins called guanosine nucleotide exchange factors (GEFs) bind to the GTPase to disrupt the binding site and remove GDP so that a new GTP molecule can then bind, restarting the cycle. A crystal structure (pdb:1LFD)[42] of the canonical member, Ras, is shown in Figure 1.4. The Switch I (red) and Switch II (blue) regions are reoriented during hydrolysis and nucleotide exchange to alter the structure of Ras, which either enables further downstream interaction in the ON state or prevents it in the OFF state. Between the switch regions is the nucleotide binding site. The nucleotide (shown in purple) is anchored by a Mg^{2+} ion (yellow).

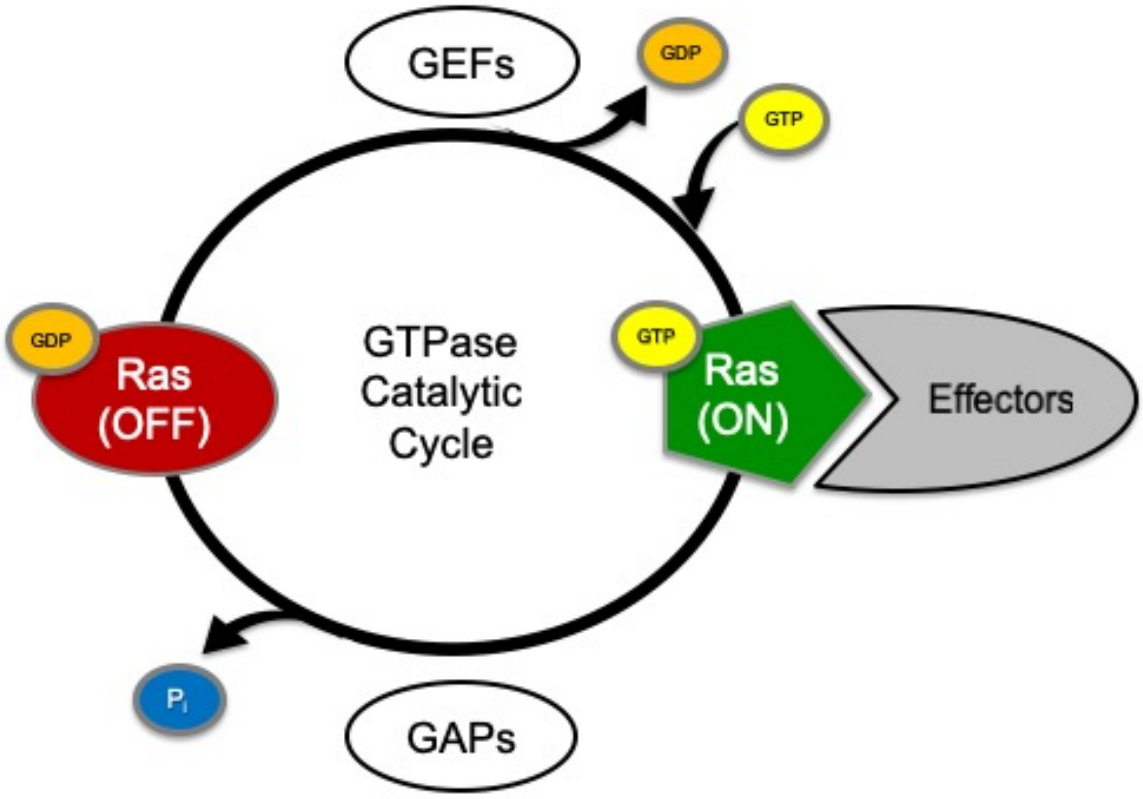

Figure 1.3: Catalytic Cycle of Ras Superfamily Proteins.

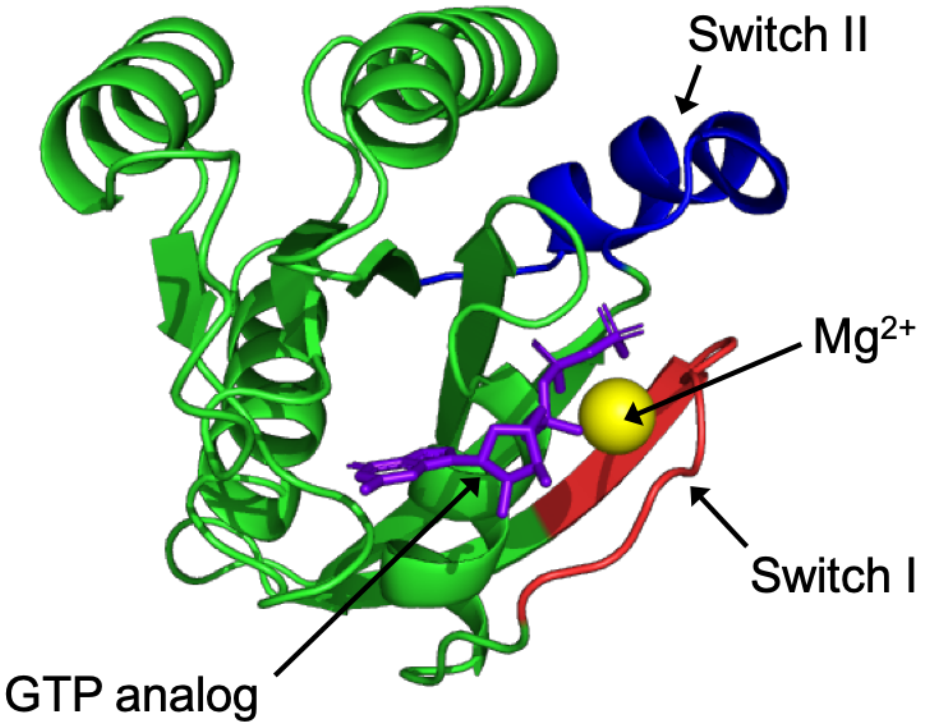

Figure 1.4: Crystal structure of Ras (pdb: 1LFD) in the GTP-bound state with important structural features identified. Switch I is colored in red, switch II is colored in blue, the catalytic Mg^{2+} ion is yellow, and the non-hydrolyzable GTP analog GppNHp is purple.

Much of the Ras superfamily signaling is regulated by the binding of the GAP and GEF partner proteins that promote the formation of either the GTP-bound or GDP-bound state depending on the needs of the cell as shown in Figure 1.3.[43] GTPases also possess much slower intrinsic GTP hydrolysis mechanisms to convert from the ON state to the OFF state, which do not require the assistance of GAPs. The intrinsic GTP hydrolysis mechanism of Ras and the interactions of a Ras superfamily member with a partner GEF protein to execute GDP exchange are the focus of Chapters 3 and 5 of this dissertation, respectively.

Our interest in the Ras superfamily is two-fold: 1) Ras superfamily members participate in rich and varied non-covalent interactions including protein-ligand interactions, protein-metal cofactor interactions, and protein-protein interactions, all with high specificity, and 2) when Ras superfamily members are mutated, the resulting effects are diverse and often cancer-causing. Several well-studied mutations which disrupt the nucleotide binding and hydrolysis activity in Ras are known to occur with high frequency in cancerous tumors. These mutations, discussed in Chapter 3, alter the rates at which Ras switches between the ON and OFF state, leading to disrupted signaling in the cell division pathway and uncontrolled cell growth. This has ensured that Ras superfamily proteins are well-studied in the literature, yet potential drug leads have been elusive.[44-46] The elaborate non-covalent interactions between the Ras superfamily members, all of their varied protein cofactors, and their interactions with the lipid scaffolding of the cell have made a unifying inhibition strategy very difficult with present drug development methodologies and technology. Detailed electrostatic interrogations of important Ras superfamily proteins and both their intrinsic functions and interactions with effector proteins are necessary to overcome this significant pharmacological challenge. VSE spectroscopy represents a relatively new approach to addressing this challenge. Our goal is to understand the non-

covalent interactions that allow wild-type GTPase proteins to execute their complex signaling roles in the cell and result in mutated GTPase proteins disrupting signaling in cells and causing cancer.

1.3: Model Staphylococcal Nuclease Proteins

While GTPases and the Ras superfamily are of significant interest to us for their diverse interactions and biological relevance, we can better investigate more fundamental properties and behavior of nitrile vibrational probes using well-studied model proteins like staphylococcal nuclease (SNase), an extracellular nuclease excreted by *Staphylococcus aureus*. SNase has been studied for over 50 years for its catalytic behavior and unusually stable structure. More recently, SNase variants have been engineered for specific experimental purposes, including increased stability and tolerance to mutation.[47, 48]

SNase is a 17 kDa extracellular nuclease of *Staphylococcus aureus* which contains a calcium binding site crucial for catalyzing the hydrolysis of DNA and RNA at the 5' position of the phosphodiester bond, producing mono- and dinucleotides.[49] The study of SNase goes back to the early work of Anfinsen and coworkers, who characterized two WT strains excreted by *S. Aureus*.[49, 50] The protein consists of 3 α-helix strands and a small barrel shaped β-sheet structure made up of 5 strands as illustrated by the crystal structure (pdb: 3BDC)[51] in Figure 1.5. The catalytic function of SNase requires Ca^{2+} in the active site, and it had been demonstrated that exchanging the calcium for other similarly sized ions maintains protein structure but completely halts protein function.[52] The stability of SNase comes from a characteristic oligonucleotide-binding fold (OB-fold) which is a common motif in proteins whose function involves cleaving DNA and RNA.[53] The particular variant used in our work is the Δ+PHS mutant, which denotes a deletion from

residues 44-49, and five mutations: P117G, H124L, S128A, G50F, and V51N. This particular strain was developed to increase the tolerance to subsequent mutations.[48]

Significant effort in the community has been dedicated to observing the properties of mutated SNase to investigate the role of charged amino acids buried in the hydrophobic core of proteins. SNase is also central to an effort to improve the accuracy of computational predictions of electrostatics. Embargoed experimental ΔpK_a data for SNase collected by the Garcia-Moreno group was used to test computational electrostatic models as part of the pK_a Cooperative, a collective effort to improve predictions of electrostatic environment in proteins.[54] VSE spectroscopy represents an alternative strategy for directly measuring electric field in proteins, and to test this we synthesized a collection of SNase proteins with nitrile probes in the same positions for which there was already pK_a shift data. We demonstrated that pK_a shift and the shift in nitrile frequency were not equivalently reporting on the electrostatic environment, and each probe has its own challenges with local effects that are not described by the Stark equation. To this end, we are continuing to build a large library of data involving specific SNase mutants to establish a reliable interpretation of nitrile shift in environments where local effects like hydrogen bonding are significant.

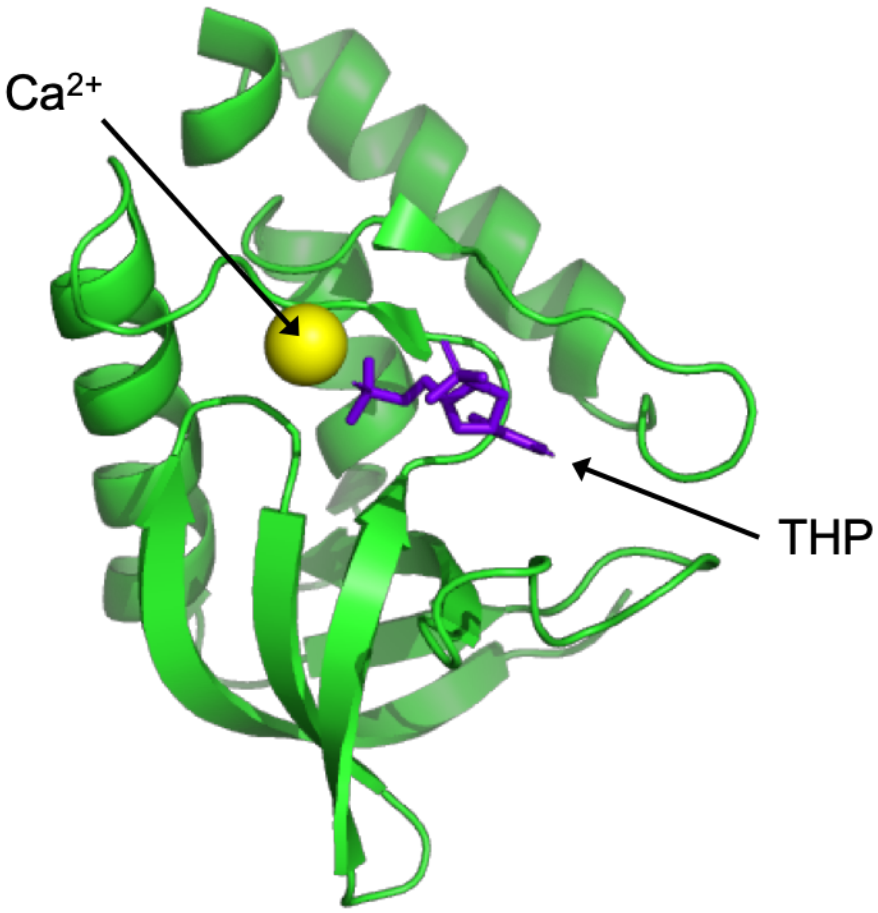

Figure 1.5: Crystal structure of the Δ+PHS variant of SNase (pdb: 3BDC). The catalytic Ca^{2+} ion is in yellow. The thymidine diphosphate (THP) inhibitor (purple) is bound in the active site, indicating the location of RNA or DNA binding.

1.4: Outline of Dissertation

This dissertation represents a body of work with the unifying goal of measuring and interpreting electric field information in proteins with VSE spectroscopy. Chapter 2 describes the methodologies used to mutate and synthesize proteins, observe the systems with a variety of spectroscopic techniques, and assess protein function with kinetic assays. Chapter 3 reports on the work we have done using the GTPase H-Ras towards understanding how electrostatics regulate function and macromolecular interactions. Chapter 4 discusses our work using SNase as a model system to investigate the relationship between pK_a and nitrile frequency as reporters of electrostatics. We also discuss the non-Coulombic forces that affect frequency and how they affect interpretation of VSE measurements. Chapter 5 discusses our preliminary work expanding VSE spectroscopy to protein-protein interactions of Arf, another GTPase, and the inhibition of protein-protein interfaces. Finally, Chapter 6 describes recent developments in mass spectrometry and their value to our measurements of non-covalent interactions in biological systems.

Chapter 2: Materials and Methods

2.1: Publication Note

Portions of the methods outlined in this chapter were adapted from the following publications:

Novelli, Elisa T.; First, Jeremy T.; Webb, Lauren J.; Quantitative Measurement of Intrinsic GTP Hydrolysis for Carcinogenic Glutamine 61 Mutants In H-Ras. *Biochemistry*. **2018**, 57 (44), 6356-6366 [ETN performed all experiments]

2.2: Mutagenesis, Transformation, and Plasmid Purification

The gene for His_6-tagged WT H-Ras, residues 1-166, was a gift from the Kuriyan laboratory. Five pET42a DNA plasmids containing the gene for the Δ+PHS variant of Staphylococcal Nuclease and a mutation, either V23C, L38C, T62C, V66C, or I92C, were generous gifts from the Garcia-Moreno laboratory. The Δ+PHS variant denotes a deletion of residues 44-49, and the mutations P117G, H124L, S128A, G50F, and V51N, as previously described.[48] Additional mutations were made by reverting the I92C mutant-containing plasmid to the wild type isoleucine, and then making five additional mutated constructs: L25C, A58C, A90C, A109C, and N118C.

A plasmid containing His_6-tagged tobacco etch virus protease (His-TEV) with the S219V mutation in *E. coli* Bl21(DE3)-RIL cells was a gift from David Waugh (Addgene plasmid 8827).[55] The gene for residues 1-166 of p^{21} H-Ras was a gift of the Kuriyan Laboratory. The 97-residue Ras-Binding Domain of Ralβ was taken from residues 790-886 of RalGDS and numbered according to the PDB entry 1LFD. The cysteines at positions 16 and 17 had previously been mutated to alanines, and the isoleucine at position 18 had previously been mutated to a cysteine. The genes for Ralβ, His_6-tagged WT c-Arf-1 (Arf), Gea1p (Gea), ARNO, and ARNO4M were synthesized and cloned into pET-15b vectors

by Genscript. The pET-15b vector contains an N-terminal His_6 tag separated from the protein by a thrombin cleavage site. In some genes synthesized by Genscript we included a TEV protease cleavage site sequence between the thrombin site sequence and the protein sequence so the His_6 tag could be cleaved with thrombin or TEV in the protein purification procedure.

Mutations to the glutamine at position 61 in Ras and the mutations in SNase were made using the QuikChange Lightning site-directed mutagenesis kit (Agilent) according to kit instructions. Short forward (5'-3') and reverse (3'-5') primers used for mutagenesis were purchased from Sigma. Varying concentrations of template DNA (usually between 10 and 100 ng/μL) were mixed with 125 ng of each primer, 5 μL of supplied buffer, 100 ng of nucleotide monomers, 1.5 μL of provided QuikSolution reagent, and high purity water to a total reaction volume of 50 μL. Reactions were pipetted up and down to gently mix after each step and then centrifuged for 30 s at 13,000 RPM when all reagents were added. Following centrifugation, 1 μL of the provided polymerase enzyme was added and the reactions were again pipetted and centrifuged to mix. Thermocycling was carried out by initially denaturing at 95 ºC for 2 min, followed by 18 cycles of a 20 s denaturing step at 95 ºC, a 10 s annealing step at 60 ºC, and an extension step at 68 ºC that lasted 5 min for Ras and 6 min 20 s for SNase. Following the 18 cycles, a final extension step at 68 ºC lasted for 5 min and then reactions were held at 4 ºC until digestion and transformation according to kit instructions.

The digestion step to degrade the original nonmutated plasmid was then carried out by adding 2 μL of the provided Dpn1 restriction enzyme to each reaction, pipetting up and down to mix thoroughly, centrifuging for 30 s at 13,000 RPM, and incubating at 37 ºC for 5 min. Immediately following digestion, the mutagenesis product was transformed into XL-10 Gold ultracompetent *E. coli* cells (Agilent) by combining 45 μL of cells per

mutagenesis reaction in pre-chilled culture tubes with 2 μL of β-mercaptoethanol and incubating on ice for 2 min. After incubation, 2 μL of mutagenesis product was added to the cell solution, and the combined solution was incubated on ice for 30 min. Each tube containing cells, β-mercaptoethanol, and mutagenesis product was then heat-shocked in a 42 ºC water bath for exactly 45 s followed by a 2 min incubation on ice to allow the mutagenesis DNA product to diffuse into the cells. After 2 min, 500 μL of Lysogeny Broth (LB) growth media was added to each tube and all tubes were incubated at 37 ºC with shaking at 250 RPM for 1 hr before plating individually on agar plates containing LB media and either 100 μg/mL ampicillin (GoldBio) for Ras mutants or 30 μg/mL kanamycin (Sigma) for SNase mutants. The plates were incubated overnight at 37 ºC, after which they were wrapped in parafilm and stored at 4 ºC for further use. Mutations to Arf and Gea were made using a similar kit, QuikChange II (Agilent), with a similar protocol.

In cases where no mutations were necessary, existing plasmid was transformed into XL-1 Blue supercompetent *E. coli* cells (Agilent) using the same procedure as above (excluding the β-mercaptoethanol), and were plated on agar plates containing LB broth and the appropriate antibiotic. For all plasmids, sequences were confirmed by Sanger sequencing carried out by the DNA sequencing core facility at the University of Texas at Austin. To generate enough DNA for sequencing, single colonies from agar plates containing transformed plasmid were used to seed 5 mL of LB media containing the appropriate antibiotic and grown overnight at 37 ºC with shaking at 250 RPM, after which cells were collected by centrifugation at 3000 RPM for 10 min. DNA plasmids were purified from the cell pellet using the Qiagen mini-prep kit exactly as described in the manual. The plasmid concentration was estimated using an ATR/UV-Vis nanodrop instrument, and the sequences were verified by submitting 11 μL of 45 ng/μL purified DNA plus 1 μL of the appropriate sequencing primer to the sequencing facility. All plasmids

described here use the T7 primer, except for Ras which uses an M13_Reverse 48-base primer.

Successfully sequenced plasmids were transformed into BL21-DE3 competent *E. coli* cells (New England Biolabs) for recombinant protein expression. 50 µL aliquots of cells were pipetted into chilled culture tubes and 2 µL of purified DNA was added before gently tapping tubes to mix and incubating on ice for 30 min. Cells were heat-shocked in a 42 ºC water bath for 45 s and then rested on ice for 2 min. 500 µL of LB media was then added, and tubes were incubated at 37 ºC with shaking at 250 RPM for 1 hr. Cells were then spread onto warmed agar plates containing LB and the appropriate antibiotic. Plates were incubated overnight at 37 ºC and then afterwards wrapped in parafilm and stored at 4 ºC for up to 1 month. The TEV protease gene was purchased from Addgene already transformed into BL21-RIL *E. coli* cells, so transformation steps were not necessary in that case. We streaked an agar plate containing LB media and 100 µg/mL ampicillin and 30 µg/mL chloramphenicol with the cells purchased from Addgene, which was incubated overnight at 37 ºC and then stored at 4 ºC before proceeding directly to protein expression.

2.3: Protein Expression

All media used in protein expression were prepared from purchased powdered media according to package instructions and autoclaved for 30 min to sterilize before use. All GTPases and related proteins (Ras, Ral, Arf, Gea, ARNO, ARNO4M) were expressed using the same strategy. A 5 mL culture was prepared by seeding 5 mL of LB broth containing 100 µg/mL ampicillin with 1 colony from an agar plate containing BL21-DE3 cells transformed with the desired plasmid. The 5 mL culture was grown overnight at 37 ºC with shaking at 250 RPM. The following morning, the 5 mL culture was added to a flask containing 2 L of autoclaved Terrific Broth (TB) media and 100 µg/mL ampicillin,

and the 2 L culture was incubated at 37 ºC with shaking at 200 RPM for approximately 8 hr, until the optical density at 600 nm (OD_{600}) reached 1.0. The temperature was then lowered to 18 ºC, and 0.5 g of isopropyl β-D-1-thiogalactopyranoside (IPTG) was added to initiate induction. Flasks continued to shake at 18 ºC overnight before cells were collected by centrifugation.

SNase was prepared by seeding a culture containing 5 mL of LB broth and 30 μg/mL kanamycin with a colony from an agar plate containing BL21-DE3 cells transformed with the desired plasmid. The 5 mL culture was grown overnight at 37 ºC with shaking at 250 RPM. The following morning, the 5 mL culture was added to a flask containing 2 L of autoclaved LB media and 30 μg/mL kanamycin. The 2 L culture was incubated at 37 ºC with shaking at 200 RPM for approximately 4 hr until OD_{600} reached 0.4-0.6. IPTG was then added to a final concentration of 1 mM to induce protein expression and shaking at 37 ºC was continued for an additional 4 hr before collecting cells by centrifugation.

TEV protease was prepared by seeding a culture containing 5 mL of LB broth, 100 μg/mL ampicillin, and 30 μg/mL chloramphenicol from a plate of BL21-RIL cells containing the TEV plasmids as provided by Addgene. The 5 mL culture was incubated overnight at 37 ºC with shaking at 250 RPM. The 5 mL culture was added to a flask containing 2 L of autoclaved LB media and 100 μg/mL ampicillin and 30 μg/mL chloramphenicol. The 2 L culture was incubated at 37 ºC with shaking at 200 RPM until an OD_{600} of 0.5 was achieved (approximately 4 hr). At this point the temperature was reduced to 30 ºC and IPTG was added to a final concentration of 1 mM. Induction proceeded at 30 ºC for 4 hr before cells were collected by centrifugation.

All cells were collected by centrifuging at 6000 RPM for 15 min. The supernatant was discarded and the cell pellet was collected into a 50 mL Falcon tube. The pellet, either dry or resuspended in buffer, was then stored at -80 ºC until use.

2.4: Protein Purification

Protein purification strategies varied and, in the case of the GTPase proteins, underwent significant optimization over the six years spanned by this work. What follows are the final established protocols for each set of proteins, though further optimization of the purification of Arf, ARNO, and ARNO4M is likely necessary. All buffer reagents were purchased from Sigma unless stated otherwise. The proteins purified in this work were, for the most part, purified in gravity columns prepared from chromatography bead resin. In some cases, fast protein liquid chromatography (FPLC) instrumentation was used (Akta, GE). Generally, either strategy could be used for any of these protein systems with the appropriate column resin.

Cell pellets containing Ras mutants were defrosted and resuspended in loading buffer (50 mM Tris-HCl, 250 mM NaCl, 40 mM imidazole, 10% glycerol, pH 7.5) for lysis by probe sonication. Cells underwent 3 rounds of sonication on ice in which the probe applied 100 W for 1 s followed by 4 s of rest for a total sonication time per round of 1 min. Between rounds cells rested on ice for 5 min. Sonication was followed by centrifugation at 19,000 RPM for 30 min to remove cell debris. The supernatant containing the protein was filtered with 10 μm Versapor syringe filters (Pall) before loading onto a nickel immobilized metal affinity column (Ni-IMAC, Fisher) equilibrated with 10x column volumes of loading buffer. After loading the protein, the column was washed with 8-10x column volumes of loading buffer. His_6-tagged Ras proteins were then eluted with an elution buffer (50 mM Tris-HCl, 250 mM NaCl, 500 mM imidazole, 10% glycerol, pH 7.5). Protein was

exchanged into a cleavage buffer (50 mM Tris, 50 mM KCl, 10% glycerol, pH 8) with a PD-10 size exclusion column (GE Healthcare) and cleaved with His_6-tagged TEV protease (His-TEV) at a ratio of approximately 1 mg His-TEV to 100 mg of His_6-Ras overnight at 4 °C. His-TEV and uncleaved Ras were removed by passing the solution through another Ni-IMAC column, and the cleaved protein in the flow through was exchanged into final buffer (50 mM Tris, 100 mM NaCl, 10% glycerol, pH 7.5) and either used immediately or flash frozen and stored at -80 °C for further use.

Ral, Arf, and Gea were purified with a similar strategy, except that the loading and elution buffers contained 50 mM sodium phosphate instead of Tris-HCl and 500 mM NaCl instead of 250 mM NaCl. After the first Ni-IMAC column, proteins were instead exchanged into a different cleavage buffer containing 20 mM Tris-base, 50 mM KCl, and 10% glycerol at pH 8. Tag cleavage was performed by thrombin at a concentration of 1-10 Units per mg of protein overnight at 4 ºC. After tags were cleaved, thrombin was removed by passing the solution through an affinity column containing benzamidine sepharose beads (GE) and the column was washed with a high salt buffer to remove any adsorbed target protein (50 mM Tris-base, 500 mM NaCl, pH 8). The flow through contained the target protein and the cleaved tag while thrombin remained bound to the column. Following thrombin removal, cleaved His_6 tag was removed by passing the solution through another Ni-IMAC column under the same conditions as the previous column. The cleaved protein eluted with the flow through and the cleaved tag was retained in the column. Purified protein was exchanged into storage buffer (50 mM Tris, 100 mM NaCl, 10% Glycerol, pH 7.5) and flash frozen and stored at -80 ºC until further use.

Because of stability challenges with Gea, we have used a similar protein, ARNO, that also binds to Arf as a guanosine nucleotide exchange factor. Based on purification challenges involving thrombin, we added a TEV protease cleavage site to the gene for new

plasmids containing Arf, ARNO, and ARNO4M. For these proteins, the TEV cleavage site allows for more streamlined purification strategies that put less stress on the protein, which is important for proteins that are inherently less stable. The newer Arf, ARNO, and ARNO4M genes can therefore also be purified according to the strategy outlined above for Ras.

The gene for SNase did not contain an affinity tag, so the purification strategy varied significantly from the previous methods described above. Additionally, because SNase is inherently toxic to cells, the *E. coli* confined the translated SNase protein in the cell in an unfolded, aggregated state called an inclusion body, and therefore purification was performed while SNase was still in the unfolded state. Cell pellets containing SNase were thawed and resuspended in Buffer A containing 6 M urea, 25 mM Tris-base, and 2.5 mM EDTA at pH8, by stirring together manually with a spatula to dissipate large chunks of the pellet before stirring together with a stir bar on a stir plate at 4 ºC for 20 min. This step used urea and EDTA to chemically break the *E. coli* cell walls instead of using mechanical methods like sonication. Cell debris and inclusion bodies were then separated from the supernatant by centrifugation at 7000 RPM for 25 min. In this case, the pellet contained both the cell debris and the inclusion bodies in which the target protein was sequestered. The supernatant was discarded and the pellet was resuspended in Buffer B containing 6 M urea, 25 mM Tris-base, 2.5 mM EDTA, and 400 mM NaCl, at pH 8. The high salt content in the second buffer freed the protein from the inclusion bodies. After manually resuspending the pellet with a spatula, the mixture was stirred on a stir plate at 4 ºC for 40 min. Once the protein was freed from the inclusion bodies, centrifugation was performed at 7000 RPM for 25 min to remove the cell debris. At this point, the target protein was contained in the supernatant which was poured off and the pellet was discarded.

The high stability of SNase allows for selective precipitation as a purification strategy, which was performed with two successive ethanol precipitation steps. First, the supernatant was combined with an equal volume of cold 100% ethanol and incubated at -20 ºC for approximately 3-5 hr. The mixture was then centrifuged at 7000 RPM for 30 min and the pellet containing unwanted precipitated protein was discarded. The supernatant containing SNase was then mixed with another equal volume of ethanol so that the final solution was 75% ethanol, and the mixture was incubated at -20 ºC overnight. This ethanol content was enough to precipitate SNase, which was collected by centrifuging the mixture at 7000 RPM for 30 min, and the supernatant was discarded. To collect the precipitated SNase, the centrifuge bottles were inverted to dry the pellet for approximately 5 min, and the pellet was transferred to a Falcon tube before resuspending in a small volume (10-20 mL) of Buffer A.

Cation-exchange chromatography was used for further purification. The resuspended protein was added to a column containing SP sepharose beads (GE) that was equilibrated with Buffer A. Once the protein was applied, the column was washed with 10 column volumes of Buffer A. The protein was then eluted with 15-20 mL of Buffer B. The eluent was mixed with 4 volumes of cold 100% ethanol and incubated for 30 min at -20 ºC to precipitate the protein. The protein was then collected by centrifugation at 8000 RPM for 15 min after which the supernatant was discarded. The protein pellet was resuspended in Buffer 2 before refolding.

Following purification, the protein was refolded by first dialyzing overnight in 4 L of 1 M KCl. Next, the dialysis solution was changed to deionized H_2O and the protein was allowed to dialyze again for 2 hr. After 2 hr, the deionized H_2O was replaced and the protein continued to dialyze for an additional 2 hr. Finally, the dialysis solution was replaced with either fresh deionized H_2O or 2 mM $CaCl_2$, and the protein was again dialyzed overnight.

The protein solution was then removed from the dialysis setup and transferred to a Falcon tube before centrifuging at 3000 RPM for 5 min to remove any aggregates due to misfolding of protein. The protein was flash frozen and stored at -80 ºC until further use.

2.5: Labeling Proteins with Thiocyanate Vibrational Probes

In many cases, these proteins included mutations from a WT residue to a cysteine residue so that nitrile probes could be introduced to purified protein. Except for SNase, all proteins were labeled with the following strategy adapted from Fafarman et al.[27] after the protein had been purified but before flash freezing or storage. The labeling reaction could also be carried out after a protein has been frozen and stored by defrosting the protein first. In the case of SNase, whose target nitrile locations were buried in the core of the protein, the labeling reaction was carried out after purification but just before the protein was refolded by dialysis. This reaction can proceed as long as the protein is in a buffer with a pH greater than 7. No difference in labeling efficiency was observed when the reaction was carried out in the high urea content in SNase Buffer B.

To label the cysteines in a protein with nitrile probes, the protein solution was mixed with a 3-10x molar excess of solid 5,5'-dithio-bis-nitrobenzoic acid (DTNB, Sigma) and inverted several times to mix. Generally, the solution turned a vibrant yellow color because the TNB^- byproduct of the solution absorbs strongly at 412 nm. If no color or only a pale yellow color was observed, this suggested an incomplete reaction due to a problem with the mutation, poor protein yield, or an inaccessible cysteine residue which resulted in inefficient labeling. The reaction was allowed to proceed for at least 2-3 hr at room temperature or at 4 ºC overnight. In some cases, the reaction was monitored by measuring absorbance at 412 nm (ϵ_{412} ~ 13600 $M^{-1}cm^{-1}$). The solution was then buffer exchanged (PD-10 column, GE) into fresh buffer to remove as much excess DTNB or TNB^- as

possible, though the solution was sometimes still pale yellow due to remaining TNB^-. At this point, approximately 30x molar excess of KCN from a 1 M stock solution was added to the reaction which turned the solution a vibrant yellow again as the TNB leaving group on the cysteine was displaced by CN^- resulting in another yellow TNB^- byproduct. This reaction was also allowed to proceed for at least 2-3 hr at room temperature or overnight at 4 ºC, after which it was buffer exchanged again to remove the TNB^- byproduct. In some cases, the solution was still slightly yellow because of saturation of the buffer exchange column. In those cases, a third buffer exchange was performed to remove any remaining reaction byproducts.

2.6: Substrate Loading and Exchange in Proteins

Nucleotides were incorporated in the GTPase proteins by incubating the protein in its final buffer with 5 mM EDTA, 4 mM dithiothreitol (DTT) and 100x molar excess of the desired nucleotide for 90 min on ice. Following the incubation, 10 mM $MgCl_2$ was added, and the solution was incubated for an additional 30 min on ice. Following the second incubation, excess reagent was removed by buffer exchanging the solution into fresh final buffer or a different working buffer before further use. This reaction was generally carried out after purification but before flash freezing. In some cases, it was also performed on already prepared and frozen protein by first thawing the sample and then proceeding with the same procedure. A similar procedure was used to exchange the metal ion in the binding site of SNase. In those cases, 5 mM EDTA and 100-1000x molar excess of the desired metal salt dissolved in water were incubated with the protein for 90 min, before buffer exchanging to fresh final buffer to remove excess reagent. Metal chloride salts were used in all cases except where mass spectrometry required the use of metal acetate salts.

2.7: Protein Characterization

Protein purity was assessed qualitatively with SDS polyacrylamide gel electrophoresis (SDS-PAGE, BioRad). Protein concentration was estimated by measuring absorption at 280 nm in a Cary 5000 UV-Vis Spectrometer in a 1 cm quartz cuvette. Note that the absorption of GTP and GDP nucleotides at 280 nm is not negligible ($\epsilon_{280} \sim 7765$ $M^{-1}cm^{-1}$). Thus, the absorptivity of GTP and GDP must be accounted for when calculating the extinction coefficients of GTPase proteins. For some experiments with GTPase proteins where an accurate concentration was necessary, the RapidGold BCA assay (Pierce) was used according to the provided instructions. Protein refolding in SNase was assessed with circular dichroism spectroscopy using a Jasco J-815 spectrometer in 1 mm path length quartz cells and averaged over 5 scans. Mass spectrometry to confirm a 26 Da increase in mass due to the incorporation of the nitrile label was performed by the proteomics core facility at the University of Texas at Austin.

2.8: Fourier-Transform Infrared Spectroscopy

All FTIR spectra were collected in a Bruker Vertex 70 spectrometer using a liquid nitrogen-cooled indium antimonide (InSb) detector. Room temperature measurements were collected by injecting samples concentrated to 1-2 mM between two sapphire windows (Meller Optics) separated by 125 μm Teflon spacers (Bruker). 250-500 scans were collected with a resolution of 0.5 cm^{-1}. Temperature dependent FTIR spectra were collected in a similar cell with 100 μM Teflon spacers. 600 scans were collected for these samples to generate equivalent signal to noise ratios as the room temperature experiments. All spectra were baseline corrected using an in-house fitting program described previously.[30] All reported values are the average of at least three measurements.

2.9: Enzyme Kinetics

The initial rates of GTP hydrolysis by RasQ61X constructs were measured using a malachite green assay to detect the production of inorganic phosphate.[56] The hydrolysis product, P_i, was detected through the formation of a colorless phosphomolybdate complex under acidic conditions, which reacted with malachite green indicator to form a colored product that was quantified by UV-Vis absorption at 640 nm according to the reaction in Figure 2.1. The assay has a broad dynamic range (typically 1-200 μM) that was tailored to the reaction conditions based on the ratio of assay volume to malachite green detection reagent volume. A calibration curve is shown in Figure 2.2. The assay has the advantage of using GTP as the substrate instead of fluorescently labeled GTP, which introduces kinetic artifacts, or radiolabeled GTP, which has associated handling hazards and expenses.

The malachite green reagent was made by separately dissolving 500 mg of ammonium molybdate and 50 mg of malachite green oxalate into 25 mL of 1 N HCl, before mixing both aliquots together and vortexing the 50 mL solution for 1-2 min. The solution was then centrifuged at 3000 RPM for 5 min and the supernatant filtered through a PES filter to remove excess solid, resulting in a malachite green reagent that was stored at room temperature in a Falcon tube wrapped in foil for up to eight weeks. A 1 mM phosphate standard stock solution was made by drying the highest available purity K_3PO_4 in an oven at 110 °C overnight before dissolving in high purity water. Lower concentration standard solutions of K_3PO_4 for the calibration curve were serially diluted from the stock solution in kinetics buffer (50 mM Tris-HCl, 50 mM NaCl, 20 mM EDTA, 5 mM $MgCl_2$, 0.01% Triton X-100, pH 7.5) at the time of the experiment. The GTP substrate solution contained 40 μM GTP and 1 mM DTT in the kinetics buffer. To minimize contamination that increased the phosphate background, we used the highest purity GTP available. Each reaction was initiated by mixing 20 μL of 8 mM RasQ61X protein in kinetics buffer with

20 μL of GTP substrate solution for a final assay reaction solution of 4 μM RasQ61X and 20 μM GTP. Reactions were incubated at 37 °C from 0-8 hr by initiating the 8 hr reaction first and then adding subsequent reactions to the incubator at each time point. All reactions were then transferred to a black, optical-bottom 384-well plate (Thermo Scientific) and all stopped at the same time through the addition of the malachite green reagent. Reactions were performed at least in triplicate and each reaction vial had enough volume for three wells, resulting in at least nine measurements for each time point. Each well contained 10 μL of assay reaction and 30 μL of malachite reagent, and the optical response was linear through the entire range of standards (0-25 μM phosphate) as shown in Figure 2.2.

A.

1) Enzyme + GTP ⇋ [Enzyme • GTP] → [Enzyme • GDP] + P_i

2) PO_4^{3-} + 12 MoO_4^{2-} + 27 H^+ $\xrightarrow{H^+}$ $H_3PO_4(MoO_3)_{12}$ +12 H_2O

3) $H_3PO_4(MoO_3)_{12}$ + HMG^{2+} $\xrightarrow{H^+}$ [MG^+ • $H_2PO_4(MoO_3)_{12}$] + 2 H^+

B.

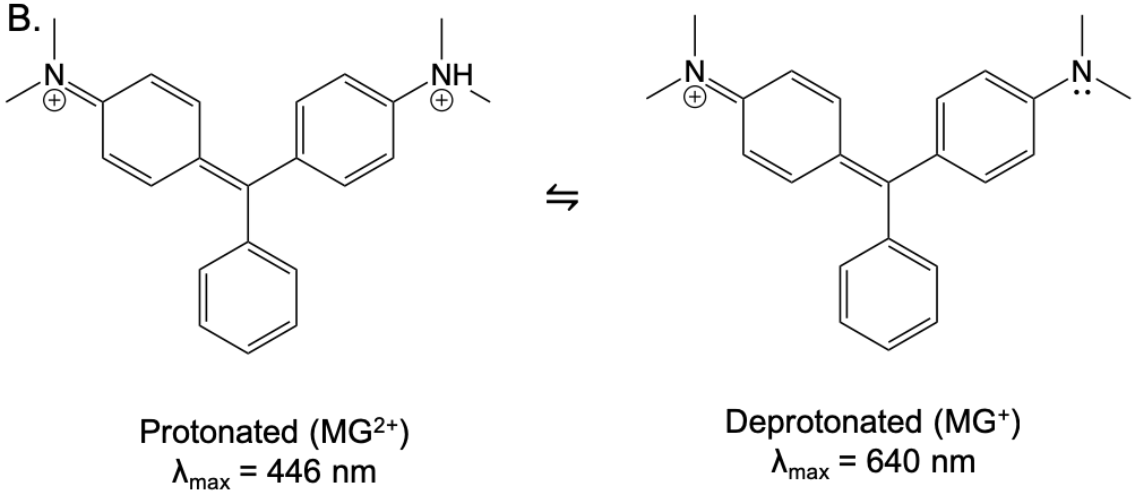

Protonated (MG^{2+})
λ_{max} = 446 nm

Deprotonated (MG^+)
λ_{max} = 640 nm

Figure 2.1: A) Scheme of the 3-step reaction that detects the phosphate product of intrinsic GTP hydrolysis by Ras. B) Structures of the protonated and deprotonated malachite green colorimetric reagent.

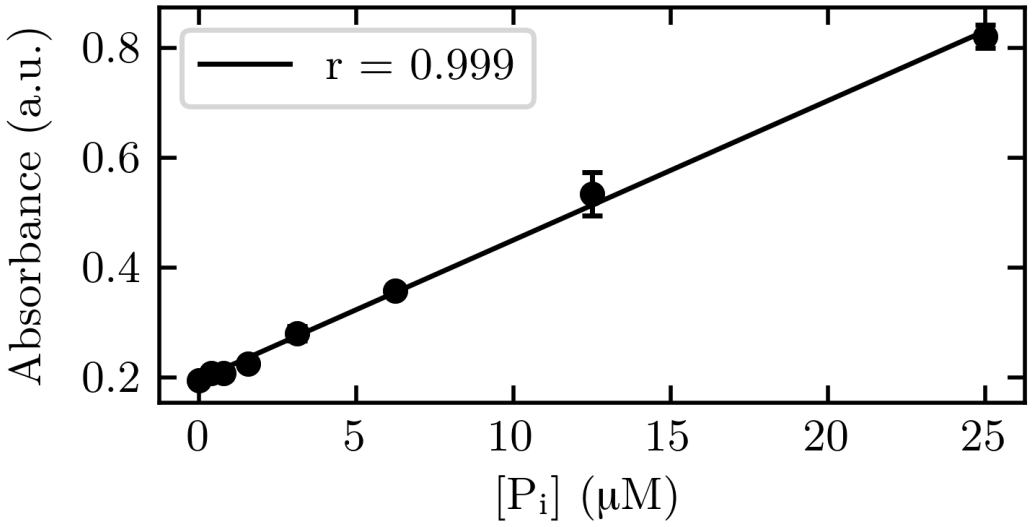

Figure 2.2: Calibration curve of the malachite green colorimetric assay collected from phosphate standards of 0.00, 0.39, 0.78, 1.56, 3.13, 6.25, 12.5, and 25 μM. The response is linear over the range of phosphate concentration measured in our experiments.

Absorption of the colored phosphomolybdate-malachite green complex was measured with a BioTek Synergy H4 plate reader at 640 nm using path length correction functionality to account for small differences in volume due to pipetting error.

Kinetics measurements of Arf activity were also measured as a control to ensure that individual mutants did not inhibit the Arf/Gea complex. These kinetic measurements were performed with a fluorescence assay in which Arf bound to GDP was pre-incubated with Gea in kinetics buffer in a black 96-well plate. The assay was initiated by spiking each well with varying concentrations of 2'-(or-3')-O-(N-Methylanthraniloyl) Guanosine 5'-Triphosphate (MANT-GTP), which is a fluorescently tagged GTP analog. The MANT-GTP was excited at 360 nm and the increase in fluorescence due to uptake was monitored at an emission wavelength of 440 nm.

Chapter 3: Comparing Vibrational Stark Effect Measurements to Protein Function in Oncogenic Ras Q61X Mutants

3.1: Publication Note

Portions of this chapter were adapted from the following publication:

Novelli, Elisa T.; First, Jeremy T.; Webb, Lauren J.; Quantitative Measurement of Intrinsic GTP Hydrolysis for Carcinogenic Glutamine 61 Mutants In H-Ras. *Biochemistry.* **2018**, 57 (44), 6356-6366 [ETN performed all experiments]

3.2: Introduction

The Ras superfamily of approximately 150 GTPases consists of signaling proteins that hydrolyze guanosine triphosphate (GTP) to guanosine diphosphate (GDP) to switch between ON (GTP-bound) and OFF (GDP-bound) states in a variety of signal transduction pathways.[57] There are multiple inputs and outputs in this catalytic cycle: 1) Ras-like GTPases interact with multiple downstream effector proteins to facilitate signaling in the ON state and propagate a signaling cascade; 2) GTPase activating proteins (GAPs) bind to Ras and facilitate GTP hydrolysis, converting Ras to the OFF state; and 3) exchange factor proteins (GEFs) bind to Ras to promote the exchange of GDP for GTP to return Ras to the ON state.[58, 59] A canonical member of this superfamily, p^{21}H-Ras (hereafter "Ras"), is part of a signaling pathway that regulates cell survival and proliferation.[44, 60-63] Mutations to Ras that slow hydrolysis and leave the protein in an ON state can lead to uncontrolled cell growth and tumorigenesis.[44] Indeed, a recent survey found mutations to the Ras family of genes appear in approximately 16% of cancer tumors, with some specific types such as pancreatic tumors showing far greater mutation frequencies.[44] Because of its role as a molecular switch, the oncogenic properties of Ras are intimately tied to the kinetics of the GTP hydrolysis reaction.

Since the discovery of Ras in 1964,[64] three key residues have been identified that, when mutated, are present in the vast majority of Ras induced tumor cells: G12, G13, and Q61.[44] The effects of mutations to the native glycine residues at positions 12 and 13 have been well studied and are largely considered to result from steric effects on the folding and dynamics of the enzyme near the active site.[65-67] However, the role of Q61 in the hydrolysis mechanism is more puzzling and has been debated continuously in the literature.[68, 69] In a crystal structure solved in 1990, Pai et al. observed a water molecule that was positioned for in-line nucleophilic attack on the leaving phosphate group and postulated that Q61 acts as a general base to deprotonate the attacking water molecule and activate it for GTP hydrolysis.[70] However, using theoretical calculations, Langen et al. demonstrated in 1992 that Q61 cannot act as the general base in such a mechanism because the activation energy for proton abstraction is too large to be consistent with the observed rate.[71] Further, in 2004, Shurki and Warshel[72] demonstrated that Q61 plays an indirect but significant role in the RasGAP-mediated mechanism of GTP hydrolysis by "pre-organizing" the active site of Ras to allow Arg789 of RasGAP (referred to as the "arginine finger") to insert into the active site and stabilize the transition state of the nucleophilic attack by water.[73] This RasGAP activity increases the hydrolysis reaction rate by a factor of 10^5.[63, 74] This mechanism of assisted hydrolysis has been further studied and characterized since.[59, 72, 75]

However, the affinity of RasGAP for Ras is three orders of magnitude lower than that of Ras and its downstream effectors,[76] and so in vivo Ras is primarily docked with a downstream effector. Because of this, therapeutic strategies for RasQ61X mutations must consider the protein when it is bound to its downstream effector, and thus when GTP hydrolysis only occurs through an intrinsic, not assisted, mechanism. The molecular-level details of this intrinsic mechanism of hydrolysis, however, have remained elusive.

In 2010, Buhrman et al. proposed a new mechanism for intrinsic hydrolysis involving two water molecules, in which the catalytic water shuttles a proton to a bridging water molecule that is stabilized by hydrogen bonds to Q61 and Y32,[77] as illustrated in Figure 3.1. This positively charged hydronium ion stabilizes the transition state in the intrinsic mechanism, partially fulfilling the role of the "arginine finger" in the RasGAP-assisted hydrolysis mechanism, although with much lower efficacy. From this perspective, the role of Q61 is to stabilize the hydronium ion, which in turn stabilizes the transition state. This mechanism was suggested based on the appearance of a crystallographic water molecule in the pdb structure 3K8Y,[77] but has not been confirmed through other experiments. However, it is further supported by the fact that, in separate work, the same group found that highly and moderately transforming (cancer causing) mutants of Q61 tended to be buried and occluded from solvent, while weakly and non-transforming (non-cancer causing) mutations were more solvent exposed.[78] This supports the idea that water is crucial to a properly functioning intrinsic hydrolysis mechanism. If this hypothesis is correct, then Q61 can be thought of as participating electrostatically, not chemically, in GTP hydrolysis, so a careful interrogation of the effects of the electric field in and around the active site at steady-state and during hydrolysis are important for proving this mechanism.

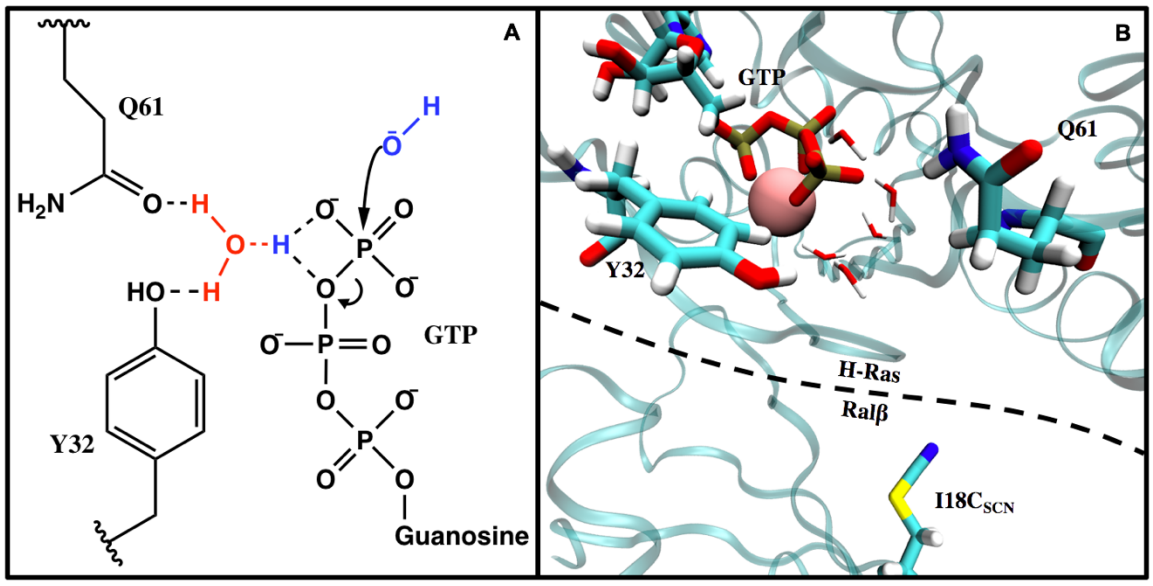

Figure 3.1: (A) A proposed multi-water mechanism of the intrinsic Ras GTPase reaction. The catalytic water (blue) shuttles a proton to a nearby, stabilized water (red) from the γ-phosphate. Adapted from ref 32 and 77. (B) A snapshot of the Ras/RalβI18C$_{SCN}$ interface. The ribbons in the background represent the backbone of the protein. The sticks represent the relevant residues in the system: Y32 of Ras, Q61 of Ras, GTP, and RalβI18C$_{SCN}$. The pink sphere is Mg^{2+} and the small sticks represent water in the active site.

Previous work in our group has made use of vibrational Stark effect (VSE) spectroscopy to interrogate the electric field of the active site of Ras constructs with mutations at position 61 (RasQ61X, where X represents a mutation from the native Gln residue).[32] In that work, a nitrile probe was strategically incorporated at position 18 of the Ras binding domain of the downstream effector RalGDS (hereafter, Ralβ) generating the construct RalβI18C_{SCN}, which denotes that the native isoleucine at position 18 was replaced with a cysteine, which was then post-translationally modified to cyanocysteine. Though a different protein, c-Raf kinase (Raf), is the primary downstream effector of Ras *in vivo*, Raf has been shown to alter some rates of intrinsic hydrolysis.[79] By docking RalβI18C_{SCN} with Ras, the nitrile group on RalβI18C_{SCN} was well positioned to report on electric field changes due to mutations to Q61 in and around the Ras active site, without affecting the intrinsic hydrolysis mechanism. A snapshot of this system based on the crystal structure 1LFD is shown in Figure 3.1.

While nitrile spectra have also been shown to report on solvation environments due to quantum mechanical effects of specific hydrogen bonding,[37, 80, 81] here we show that the solvent exposure and specific hydrogen bonding interactions of the nitrile on RalβI18C_{SCN} are identical between the Ras mutants. We therefore interpreted the shifts in vibrational frequency of the nitrile probe on Ralβ as changes in local electric field caused by mutations to Q61 in Ras across the protein-protein interface (~9 Å). Because a multi-water intrinsic hydrolysis mechanism, such as that proposed by Buhrman et al., relies on non-covalent stabilization of water in the active site, we compared the shifts in nitrile frequency to quantitative measurements of the ability of the side chain to interact with water. We observed correlations between the nitrile shifts and both the solvent accessible surface area (SASA) and the hydration potential of the residue at position 61.[32] Based on these results, we hypothesized that the identity of the residue at position 61 affects the rate of intrinsic

GTP hydrolysis through the noncovalent and electrostatic stabilization of water molecules according to each residue's affinity for water, supporting a multi-water mechanism, such as the hypothesized hydrolysis mechanism proposed in Figure 3.1.

In spite of the ongoing debate regarding the role of Q61 in the mechanism of intrinsic hydrolysis, there has not yet been a comprehensive quantitative examination of the role of Q61 mutations on the intrinsic hydrolysis rate. Though the literature has suggested that at least 17 Q61X intrinsic hydrolysis rates have been measured, most have not been explicitly reported and, to our knowledge, were measured only semi-quantitatively.[82] Fully quantitative intrinsic hydrolysis rate constants of RasQ61X mutations have only been reported for WT, E, H, and L.[83, 84] The original manuscript described in the publication note (Chapter 3.1) includes a significant number of MD simulations that were performed by Jeremy First. Those data are not included in this dissertation except where directly compared to experimental measurements for the purposes of discussion. In those cases, data resulting from those calculations will be identified in text and figure captions.

3.3: Adapting a Phosphate Colorimetric Assay for Ras

Intrinsic rates were measured using a malachite green colorimetric assay based on the binding of malachite green indicator to a phosphomolybdate complex formed from the phosphate product of the GTP hydrolysis reaction. This GTPase activity assay is useful because it is a sensitive and non-radioactive technique for detecting phosphate and has been successfully applied to other GTPase proteins.[56] The hypothesized mechanism for intrinsic GTP hydrolysis by Ras in Figure 3.1 proposes that the electric field created by the arrangement of amino acids at the Ras surface are critically important for enzyme function.

To determine the effect that each Q61X mutation had on the local electric field, it was necessary to determine the extent to which each mutation changed the rate of enzyme hydrolysis, which was not possible to construct from the literature. Various methods used previously on different RasQ61X mutants have not been comprehensive or quantitative, but generally it has been found that mutations to position 61 result in slower intrinsic GTP hydrolysis rates.[82, 83] We measured the initial rate of intrinsic hydrolysis of WT Ras and 18 mutants at position 61 to examine the role of the residue in the electrostatic stabilization of the proposed hydronium ion. To do this, we monitored the increase in concentration of phosphate over time for each mutant as measured using a malachite green colorimetric assay. Because the Ras-GTP complex has a K_d in the picomolar range, the addition of excess GTP to initiate the reaction resulted in a single exponential rise in the concentration of phosphate. In order to have a quantitative comparison between the mutants in our experiment, we used linear regression on the first five measurements of phosphate concentration (i.e., 0-80 min) which corresponds to the linear portion of the exponential curve. Representative curves are shown in Figure 3.2. We extracted the initial rates from the slope of the resulting fits, and all fits are shown in Figure 3.3. Initial rates for all mutants are reported in Table 3.1. The error is reported as the standard error of the linear regression. In some cases, we obtained a better fit with smaller error by omitting the first data point, because of low sensitivity of the zero time-point in colorimetric assays. In all cases, we report the fit that yielded the lowest standard error. We chose to measure the initial rate of the reaction rather than a fit of the observed rate over the entire exponential curve because some mutants do not appear to have reached equilibrium through the course of the 8 hr experiment, either because the mutant is too slow, or because the mutant protein no longer functions due to denaturation or aggregation. However, it should be noted that only the

Q61V construct visibly precipitated after 3 hr at 37 °C, and there was no other visible aggregation for any other mutant over the course of the 8 hr experiment.

Though the most common approach to enzyme kinetics is the Michaelis-Menten formalism,[85, 86] in this case the mutations at position 61 should affect the turnover rate of the enzyme (k_{cat}) and not the overall Michaelis constant (K_m). Because of this, measuring the initial rate at a single substrate concentration was be sufficient, given the number of constructs we investigated. Because initial rates depend on a variety of conditions including protein and substrate concentrations, buffer conditions, and temperature, all constructs were measured under exactly the same conditions, so they could be compared appropriately.

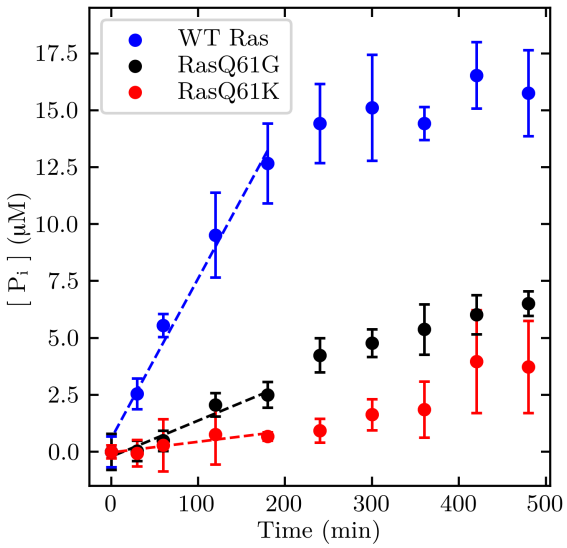

Figure 3.2: Representative kinetic measurements of 4 μM RasQ61X constructs reacted with 20 μM GTP over 8 hr; WT (blue), Q61G (black), and Q61K (red). The dashed lines represent the linear fit to the first five time points. The slope of the linear fit is the initial rate of the intrinsic hydrolysis reaction. The rates for each mutant are reported in Table 3.1.

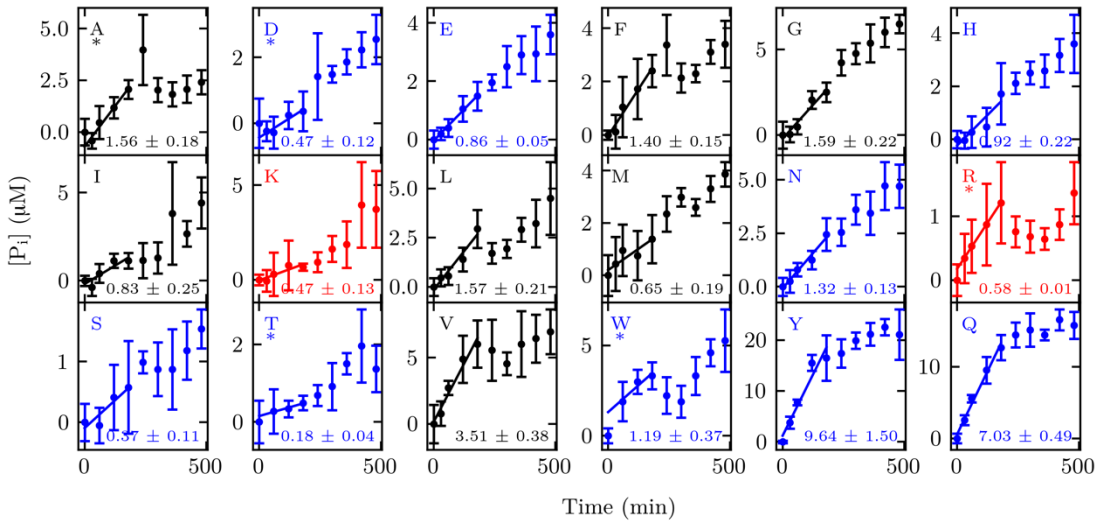

Figure 3.3: The production of inorganic phosphate, P_i, as a function of reaction time for all viable RasQ61X constructs. The identity of the amino acid at position 61 is shown in the upper left corner of each plot. The first five points were fit with a linear regression. The slope and standard error of the fit are displayed in the bottom-right corner of each window. If a lower standard error was obtained by omitting the first time point (0 min), then that fit is reported. Such cases are marked with an asterisk in the top-left corner. Blue: polar or negatively charged residues; red: positively charged residues; black: nonpolar residues.

Ras Construct	$\tilde{\nu}^a$ (cm^{-1})	Initial Rate (10^{-2} μM min^{-1})	SASA of: ($Å^2$) polar atoms	side chain
WT Ras[b]	2162.8 ± 0.2	7.03 ± 0.49	65 ± 15	98 ± 16
Residues with Charged Sidechains				
RasQ61D	2162.0 ± 0.1	0.47 ± 0.12	51 ± 7	77 ± 7
RasQ61E	2162.8 ± 0.2	0.86 ± 0.05	$60 \pm 10.$	91 ± 11
RasQ61K	2163.1 ± 0.2	0.47 ± 0.13	50 ± 17	114 ± 22
RasQ61R	2162.4 ± 0.1	0.58 ± 0.01	71 ± 24	121 ± 24
Residues with Polar Sidechains				
RasQ61H	2163.8 ± 0.2	0.92 ± 0.22	34 ± 6	108 ± 14
RasQ61N	2162.7 ± 0.2	1.32 ± 0.13	49 ± 13	76 ± 10
RasQ61S	2164.4 ± 0.1	0.37 ± 0.11	18 ± 9	47 ± 9
RasQ61T	2164.7 ± 0.2	0.18 ± 0.04	20 ± 9	59 ± 11
RasQ61W	2164.1 ± 0.2	1.19 ± 0.37	$18 \pm 10.$	151 ± 21
RasQ61Y	2163.5 ± 0.1	9.64 ± 1.50	36 ± 15	$130. \pm 25$
Residues with Nonpolar Sidechains				
RasQ61A	2162.0 ± 0.2	1.56 ± 0.18		
RasQ61F	2163.0 ± 0.2	1.40 ± 0.15	0 ± 0	114 ± 21
RasQ61G	2163.1 ± 0.1	1.59 ± 0.22		
RasQ61I	2164.0 ± 0.2	0.83 ± 0.25	0 ± 0	95 ± 9
RasQ61L	2163.2 ± 0.2	1.57 ± 0.21	0 ± 0	102 ± 14
RasQ61M	2162.6 ± 0.1	0.65 ± 0.19	0 ± 0	101 ± 20
RasQ61V	2163.9 ± 0.0	3.51 ± 0.38	0 ± 0	78 ± 11

Table 3.1: Vibrational frequencies of a nearby nitrile on RalβI18C_{SCN}, measured intrinsic initial rates of GTP hydrolysis, and computed SASA values of both the entire side chain as well as only the side chain polar atoms (N, O, and hydrogens bound to N or O) from MD simulation for 18 constructs of RasQ61X. Errors in the rate are reported as the standard error of the linear fit. Error in the SASA is reported as the standard deviation of the entire ensemble of structures. *a* Taken from ref. 32, *b* the identity of position 61 in wild-type Ras is Q.

3.4: GTP Hydrolysis Rates in Ras Q61X Mutants

In general, our results corroborate previously reported qualitative results that Q61X mutants tend to have significantly lower rates of intrinsic GTP hydrolysis with one notable exception: Q61Y had a faster initial rate ($9.64 \pm 1.50 \times 10^{-2}$ μM min^{-1}) than the WT ($7.03 \pm 0.49 \times 10^{-2}$ μM min^{-1}). However, all other Q61X mutant rates were slower than WT. Q61V had a moderate hydrolysis rate of $3.51 \pm 0.38 \times 10^{-2}$ μM min^{-1}. However, this construct precipitated after 3 hr, suggesting that while the initial rate was faster than other mutations, the protein was less stable. The other 14 mutants we measured had initial rates of intrinsic GTP hydrolysis of less than 2.00×10^{-2} μM min^{-1}.

In order to understand these results, we sorted the mutants into categories based on the polarity and ionizability of the side chain at position 61, factors which are expected to be significant for the ability to interact with and stabilize any catalytically important water molecules in and near the active site. Residues with positively charged side chains (K and R) had measured initial rates between 0.40×10^{-2} and 0.60×10^{-2} μM min^{-1}, a fifteen-fold decrease in intrinsic rate from WT. Residues with negatively charged side chains (D and E) had measured initial rates between 0.40 and 0.90×10^{-2} μM min^{-1}, a ten to twenty-fold decrease. For the nonpolar residues (A, F, G, I, L, M, and V), we measured initial rates between 0.6×10^{-2} and 1.6×10^{-2} μM min^{-1}, with the exception of V for which we measured a rate of 3.51×10^{-2} μM min^{-1}. Polar, uncharged residues (H, N, Q, S, T, W, and Y) varied much more significantly, the fastest of which were the WT (Q) measured at 7.03×10^{-2} μM min^{-1} and Y measured at 9.64×10^{-2} μM min^{-1}. Two of the larger polar residues (H and W) had measured rates of 0.92×10^{-2} μM min^{-1} and 1.19×10^{-2} μM min^{-1}, respectively. The smaller polar residues (S and T) were among the slowest mutants with rates of 0.37×10^{-2} μM min^{-1} and 0.18×10^{-2} μM min^{-1}, respectively. The remaining large polar mutant (N) which is the most chemically similar to the wild type Q, had a rate of 1.32×10^{-2} min^{-1},

approximately six times slower than the WT rate. Although the few published rate constants of intrinsic hydrolysis by RasQ61X mutants reported in the literature have been calculated using the Michaelis-Menten formalism, and therefore cannot be compared directly to our initial rate measurements, we report them here for convenience. John et al. reported rate constants of 2.8 x 10^{-2} min^{-1} for the WT Ras, and 0.2 x 10^{-2} min^{-1} for RasQ61H.[87] Krengel et al. reported an observed rate of 0.1 x 10^{-2} min^{-1} for RasQ61L.[83] RasQ61E has been reported to have a 10-fold slower hydrolysis rate than the WT;[82] however, Frech et al. reported a 20-fold faster intrinsic hydrolysis rate for RasQ61E when controlling for the 100-fold larger K_d values for the RasQ61E-GTP complex.[84]

Previously, our group used VSE spectroscopy to measure electric field changes due to the change in identity of the residue at RasQ61.[32] In those experiments, RasQ61X was docked to Ralβ$I18C_{SCN}$, which contained a cyanocysteine vibrational probe. The FTIR absorption frequencies from the nitrile group on the probe when docked to each Ras mutant are listed in Table 3.1. Though Ralβ docks to GTP-bound Ras with micromolar K_d, we did not expect it to have an effect on the Ras intrinsic hydrolysis rate. To confirm this, and in order to compare our rate results with the published VSE data, we measured the intrinsic hydrolysis rate of WT Ras alone versus WT Ras docked to Ralβ$I18C_{SCN}$ and observed no differences in the rate of intrinsic hydrolysis whether or not Ralβ$I18C_{SCN}$ was present (Figure 3.4).

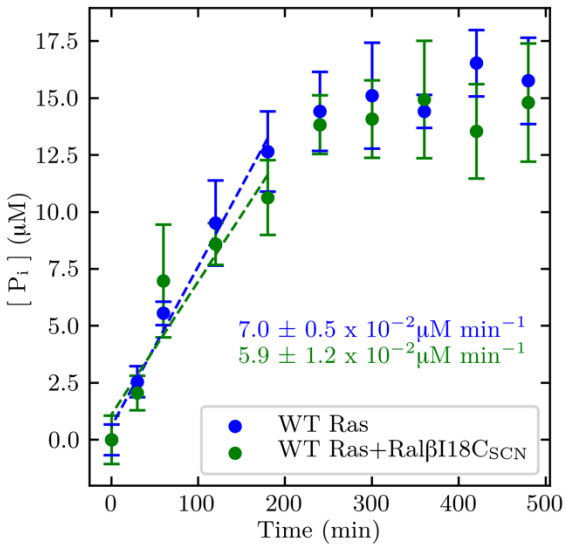

Figure 3.4: The concentration of the phosphate product of the intrinsic hydrolysis reaction for both WT Ras (blue) and WT Ras docked to RalβI18C$_{SCN}$ (green) over 8 hr. Linear regression fits are shown to the first five time points of each data set, and the slopes are displayed in the corresponding color. The intrinsic hydrolysis rate of WT Ras/RalβI18C$_{SCN}$ is within error of the intrinsic hydrolysis rate of WT Ras alone ($5.9 \pm 1.1 \times 10^{-2}$ μM min^{-1} and $7.0 \pm 0.5 \times 10^{-2}$ μM min^{-1} respectively).

3.5: Discussion

Because the proposed mechanism of intrinsic hydrolysis of GTP in Ras (Figure 3.1) relies on electrostatic stabilization of a transient hydronium ion in the active site, we plotted the measured vibrational frequencies from Stafford et al. against the measured initial rates of intrinsic hydrolysis (Figure 3.5).[32] Since hydrolysis rates change by nearly two orders of magnitude, it is useful to view these differences in rate on a logarithmic scale. For the polar and negatively charged residues, which are capable of stabilizing the proposed hydronium ion, the rates increased with increasing nitrile absorption frequency until ~2163 cm^{-1}, the approximate absorption energies of Ras containing both Q (i.e. WT) and Y at position 61, and then rapidly decreased with the continued increase in absorption frequency. This correlation was fit to a normal distribution with the residues capable of stabilizing the hydronium ion (the polar and negatively charged residues). For these data, residues that caused the nitrile absorption frequency to red-shift or blue-shift from ~2163 cm^{-1} decreased the rate.

Because nitrile groups have been shown to report on changes in solvation due to hydrogen bonding, we calculated the SASA of the nitrile on RalβI18C_{SCN} and the number of waters within a 5 Å sphere of the nitrile. These values were computed from MD simulations performed by Jeremy First,[88] and they were within error of each other for all of the Q61X mutants. Further, because the solvation effect is caused by changes in specific hydrogen bonding interactions,[89] we calculated the geometries of each observed hydrogen bond between the nitrile and solvent. Recently, we have shown that the geometry of these interactions can dominate the vibrational frequency.[90] In this case, however, the average angles and distances of the hydrogen bonding interactions were all within error of each other for each of the 18 mutant systems.

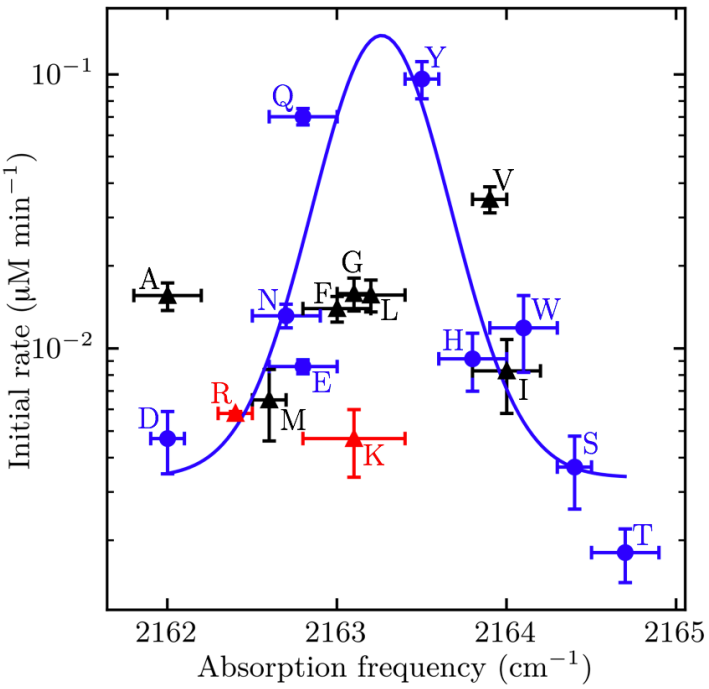

Figure 3.5: Vibrational frequencies of the nitrile on RalβI18C$_{SCN}$ against the log of the measured intrinsic rate of GTP hydrolysis. Blue: polar and negatively charged side chains; black: all nonpolar side chains; red: the two positively charged side chains. Blue line: normal distribution fit to the polar and the negatively charged side chains. All points that were excluded from the fit are marked with triangles.

Together, these data demonstrate that the perturbation to the solvation environment caused by the mutation has relaxed over the ~9 Å distance to the nitrile probe. We have previously demonstrated that in cases of similar hydrogen bonding environments, such as these systems, shifts in nitrile frequency agree with independent measurements of electric field.[26, 91] We therefore interpret the shifts in absorption frequency as a measure of change in electric field through the Stark equation as described in Chapter 1 of this dissertation.

The observation in Figure 3.5 supports the hypothesis that the role of Q61 is to provide an electrostatic contribution to the stabilization of water near the active site, and that Q61X mutants that do not provide the optimal electrostatic potential, i.e. all mutants studied besides Q and Y, are less effective at stabilizing the catalytic hydronium ion. Mutations that caused a deviation from the optimal field in either direction (measured as a red or blue shift in the nitrile vibrational frequency) disrupted the intrinsic mechanism and decreased the rate, except for residues that did not stabilize a hydronium ion, resulting in rates that are normally distributed about an optimal field.

For the residues that would be unable to stabilize the hydronium in the active site, no such trend was observed. Two of the uncorrelated residues are R and K, the two positively charged amino acids (red data points in Figure 3.5). These two side chains are incapable of stabilizing a hydronium ion due to Coulombic repulsion and are thus easily explained. The hydrophobic residues at position 61 display more interesting behavior, however, with a range of hydrolysis activity depending on the identity of the hydrophobic residue (black data points in Figure 3.5). For example, V has an intermediate initial rate of intrinsic hydrolysis ($3.51 \pm 0.38 \times 10^{-2}$ μM min^{-1}), while M has a very low initial rate ($0.65 \pm 0.19 \times 10^{-2}$ μM min^{-1}). Side chain size alone does not explain this observation; G, A, V, and L increase in molecular volume in that order, but the rates of GTP hydrolysis in those Q61X mutants do not follow the same trend.

In order to investigate the effect of side chain size we plotted the polar atom SASA and the side chain SASA for each mutant against the nitrile shift and the initial rate of GTP hydrolysis. As observed in Stafford et al., the SASA of the polar atoms are well correlated with the measured vibrational frequency of the nearby nitrile on RalβI18C_{SCN} (Figure 3.6a). With increased sampling and increased accuracy of the SASA calculation, our correlation (r = -0.89) is improved compared to the previous result.[32] Therefore, the measured field observed by the nitrile is a good measure of its ability to interact with water, and thus a good metric by which to evaluate the hypothesis of Buhrman et al. No correlation was observed between the polar atom SASA and the measured intrinsic rate, and when we measured the side chain SASA, we found that it did not correlate to the nitrile shifts However, we found that the SASA of the side chain was moderately correlated (Figure 3.6b, r = 0.81) to the measured initial rate of the side chains capable of stabilizing the hydronium ion (the polar and negatively charged residues), with the exception of W. Because of the unique chemical structure of W, the side chain SASA was extremely large, yet the large SASA of W did not translate to a large number of water molecules in the active site of the protein. This prompted us to calculate how many water molecules were actually present in the GTP binding site based on the identity of the residue at position 61.

While SASA is a convenient measure of the ability of a residue to interact with water, it lacks molecular level details of the interaction. Specifically, it does not address how much solvent is actually interacting with the residue. Instead, it only estimates the area of a residue that could interact with solvent. Because of this distinction and the observation that W interacted with a small number of waters, we calculated the number of waters that are confined to the active site around GTP from the MD simulations performed by Jeremy First. All waters that were within 5 Å of GTP's reactive terminal phosphate oxygen atom and within 5 Å of the side chain of Q61 were considered to be in the active site. We have

plotted the Boltzmann weighted average number of water molecules that met these criteria against the log of the measured intrinsic rate in Figure 3.7. We found that the number of waters in the active site was strongly correlated (s = 0.93) to the log of the measured intrinsic rate for residues that are capable of stabilizing the proposed hydronium ion, that is for polar residues and negatively charged residues. We interpret the observation of this strong correlation to mean that the ability of the residue at position 61 to interact with water impacts the intrinsic hydrolysis rate.

The positively charged residues (R and K) and the nonpolar residues (M F, V, L, and I) are not included in the linear regression fit. Interestingly, it appears that the three branched nonpolar residues I, L, and V do still fit this same trend (including these residues in the fit does not change the correlation). However, without a concrete reason to include I, L, and V and exclude M and F, we have decided to omit all nonpolar residues from the trend. Indeed, if we consider the hydration potential of each residue as reported by Wolfenden et al.,[92] which quantifies the free energy of the transfer of the side chain from the vapor phase to buffered water, this distinction becomes even more interesting. When calculated in a vacuum, M and F are the only hydrophobic residues for which the transfer from the vapor phase to the solution phase occurs spontaneously, with negative hydration potentials (-1.48 and -0.76 kcal mol^{-1}, respectively, at pH = 7), while under the same conditions, the other hydrophobic residues I, L, and V had positive hydration potentials (2.15, 2.28, and 1.99 kcal mol^{-1}, respectively, at pH = 7). This suggests that these two outliers have higher affinities for water and are changing the organization of water in the active site in some manner that is different from the other nonpolar residues.

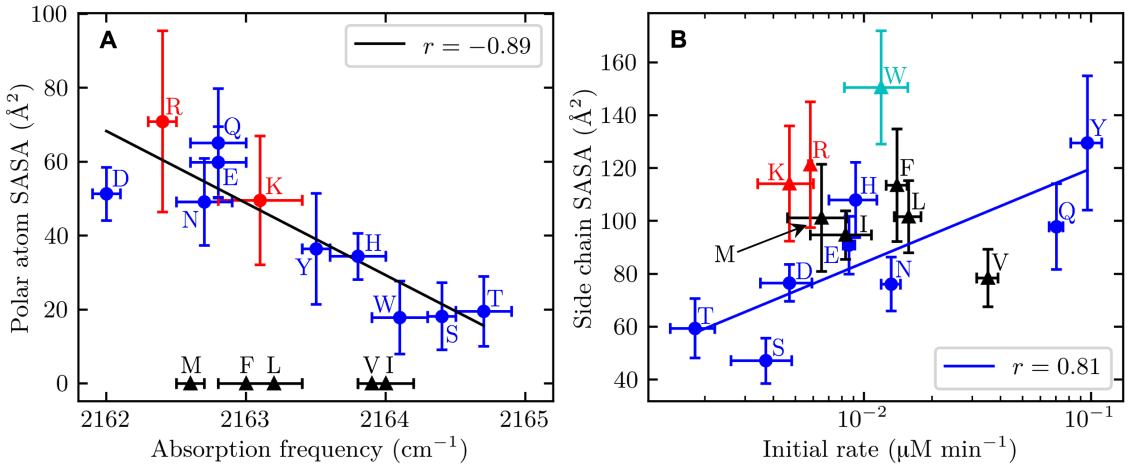

Figure 3.6: Boltzmann-weighted polar atom and side chain SASAs compared to experimentally measured values of nitrile absorption frequency and initial rate of intrinsic hydrolysis in RasQ61X mutants. A: The absorption frequency of the nitrile on RalβI18C$_{SCN}$ against the polar atom SASA of Q61X from ref 32. B: The initial rate of intrinsic hydrolysis against the side chain SASA of Q61X. Blue: polar or negatively charged side chain; red: positively charged side chains; black: nonpolar side chains. Triangles: residues not included in the linear regression. In panel B, W (cyan) is excluded from the polar residue group as discussed in the text. SASA values reported here were calculated from MD simulations performed by Jeremy First.

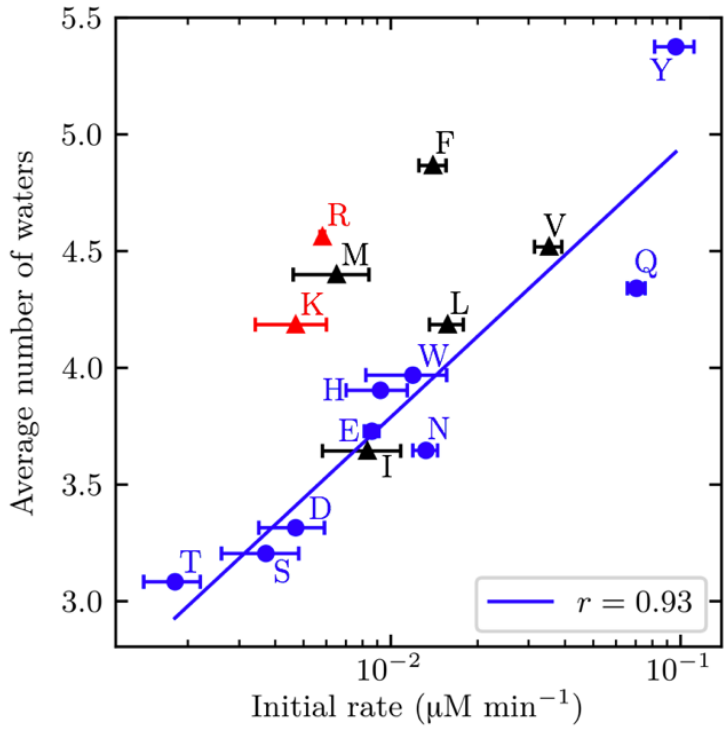

Figure 3.7: The Boltzmann-weighted average number of waters in the active site per frame against the measured intrinsic rate. The number of waters was calculated from each MD trajectory performed by Jeremy First. To be considered in the active site, each water needed to be within 5 Å of the Q61X side chain and within 5 Å of the terminal phosphate oxygen of GTP. Blue: all polar or negatively charged side chains. All other points are marked as triangles and are excluded from the fit. Red: positively charged side chains; black: nonpolar side chains.

It is interesting that the positively charged and nonpolar residues had nonzero intrinsic hydrolysis rates, despite being unable to stabilize the transient hydronium ion. Without more information, it is impossible to determine if the rates are merely shifted from the correlation in Figure 3.7, or if these mutants are hydrolyzing GTP through an alternative mechanism that does not rely on the stabilization of a hydronium in the transition state.

Nevertheless, these results strongly support a multi-water intrinsic hydrolysis mechanism, such as the one shown in Figure 3.1, in which Q61 electrostatically stabilizes a hydronium ion in the transition state caused by the nucleophilic attack of a basic water molecule. In the case of the mechanism proposed by Buhrman et al., the hydronium ion is thought to be located between Q61, the bridging oxygen to the γ-phosphate, and a terminal oxygen on the γ-phosphate. This location was originally proposed based on observations from a crystal structure which, by necessity, were obtained with the non-hydrolyzable GTP analog 5'-guanylylimidodiphosphate (GppNHp) in the binding site. It is generally thought that the conversion of the bridging oxygen to a nitrogen between the second and third phosphate is a fairly conservative change, and it has allowed for the study of GTPases in the ON state. In the case of the VSE measurements by Stafford et al., which also relied on GppNHp, there should be very little difference in the results between GTP-bound Ras and GppNHp-bound Ras because the only observable perturbation at this distance should be electrostatic. However, the effect on the hydrogen bonding network caused by the switch of an oxygen to a nitrogen in the phosphate region may not be negligible. Indeed, in every one of our simulations of Q61X constructs with GTP, the bridging oxygen accepts a hydrogen bond from the amide backbone of G12. However, this interaction is not present in the crystal structure of Buhrman et al. The replacement of GTP with GppNHp in the crystal structure replaces a hydrogen bond accepting oxygen (the bridging oxygen) with a hydrogen bond donating nitrogen, which could push G12 farther from the γ-phosphate,

providing room for a water to be observed in between G12 and GppNHp. In our simulations, however, the hydrogen bond between G12 and GTP brings the protein backbone too close to allow for a water in this location. Therefore, while our data supports a multi-water mechanism in which Q61 electrostatically stabilizes a hydronium ion, which in turn stabilizes the transition state, we hypothesize that the hydronium ion must be elsewhere.

Ultimately, the ability of each of these mutations to slow hydrolysis enough to convert Ras into an oncoprotein is based not only on its role in the intrinsic hydrolysis reaction, but also on the likelihood that the DNA mutation causing these changes could occur. It is therefore not surprising that the oncogenic mutants of RasQ61X are also the statistically most likely to occur because they require the mutation of only a single nucleotide. The E, K, L, and R codons are only a single base switch away from the WT Q; the work described here demonstrates that any one of those changes results in a drastic suppression of intrinsic hydrolysis, leading to oncogenic effects which have been cataloged elsewhere.[44, 67] It has been suggested by Cox et al. that therapeutic strategies targeting the intrinsic hydrolysis mechanism of Ras may need to be mutation-specific[46] and therefore require knowledge of the differences in the electrostatic contributions of these side chains. Our data set can be used to validate new computational models and inform future drug design efforts towards targeting the oncogenic forms of H-Ras.

3.6: Conclusions

We measured initial rates of intrinsic hydrolysis of GTP by WT Ras and 18 mutants of Q61. We compared the measured rates to previous measurements of nitrile probe frequency shift for each construct and found that polar and negatively charged residues, which are capable of stabilizing a hydronium ion, have initial rates that were

normally distributed around a central nitrile frequency of ~2163 cm^{-1}. Further, we compared the initial rates to the average number of waters in the binding site calculated from MD simulations and showed that the number of waters in the binding site was strongly correlated with the initial rate for residues that can stabilize a hydronium ion. These observations support a multi-water mechanism of intrinsic hydrolysis, such as that of Buhrman et al. These reported rates will guide pharmacological efforts to drug the intrinsic mechanism of Ras. We further postulated that the proposed location of the transition state hydronium ion cannot be located at the bridging oxygen based on the observation of a hydrogen bond between G12 and GTP that was not present in the crystal structures that used the non-hydrolyzable GTP analog, GppNHp. Together, these results form a data set that will be useful for validating computational models and potential future therapeutic strategies.

Chapter 4: Disagreement Between pKa and Nitrile Vibrational Probes of Electrostatics: Experiments and Simulations in Staphylococcal Nuclease Reveal the Importance of Local Interactions

4.1: Introduction

Electrostatic forces play a critical role in many biological phenomena, and are of long-standing interest to the biophysical community. In proteins, for example, many biochemical processes such as folding, catalysis, and intramolecular interactions are regulated by electric fields, resulting from the arrangement of partial charges on each of the many thousands of atoms within the protein structure.[1] The understanding of the molecular detail of the structure, dynamics, and function of proteins therefore depends on accurate, quantitative experiments and calculations of highly heterogeneous electric fields inherent in their structure.[93] However, because the Coulombic interactions between the partially charged atoms decay over relatively long distances compared to other intermolecular forces, the complexity of these interactions often make them extremely difficult to measure experimentally and predict computationally.

A common strategy for experimentally assessing the electrostatic environment in complex biological systems such as proteins is based on measuring the change in pK_a (ΔpK_a) of ionizable amino acid side chains in a buried, hydrophobic protein interior compared to the pK_a of the isolated amino acid in water.[2-5, 94] The local distribution of partial charges in the protein in the immediate area around the ionizable residue can electrostatically stabilize or destabilize the charged state of the amino acid relative to the neutral state. This electrostatic effect changes the ΔG of the proton transfer process and shifts the equilibrium according to eq 4.1:

$$\Delta\Delta G = \Delta \text{ p}K_a / \text{RT}\bullet\ln(10) \qquad \text{[Equation 4.1]}$$

where $\Delta\Delta G$ is the change in the free energy of the proton transfer reaction, R is the ideal gas constant, and T is the temperature. Experimentally, Δ pK_a values can be measured in a variety of ways, such as with NMR chemical shifts,[2, 5] and pH dependent thermodynamic stability experiments.[95] A large number of pK_a shifts of ionizable residues in a many proteins have been collected and reported.[96] In particular, Garcia-Moreno and coworkers systematically mutated several ionizable residues at 25 buried locations into a highly stable engineered variant of staphylococcal nuclease (Δ+PHS, hereafter referred to simply as "SNase"). Using these pK_a probes, the authors measured shifts of up to ~6 pH units, favoring the neutral state that reflected the solvent accessibility of the probe in the protein environment.[6, 94, 95, 97]

This dataset has since been used as a common target to validate different computational electrostatic models.[98, 99] A notable coordinated effort towards this goal, known as the pK_a Cooperative,[54] compared predicted pK_a shifts to the experimental pK_a shifts measured in SNase by the Garcia-Moreno group. Because of the complexity of the electrostatic environment in proteins, accurately modeling the effects of the electric fields requires either a prohibitively expensive calculation or a significant oversimplification of the physical properties of the system. Consequently, the inability of many of these models to accurately reproduce the measured pK_a shifts demonstrated the challenge for current computational strategies to adequately model electrostatic interactions in proteins. The computational results produced by the pK_a Cooperative were typically able to predict the direction of the pK_a shift but not the magnitude, and in some cases were off by several pH units, indicating substantial uncertainty in the equilibrium protonation state of the titratable residue.[98, 100] While these efforts show promise, particularly since they are benchmarked against a common experimental database, the measurement of a pK_a shift is, in itself, an oversimplification of the diverse interactions in a protein interior. One of the most

significant issues is that shifts in pK_a are not direct measurements of electric field. Instead, they represent a change in stability that is dependent on a variety of factors other than electrostatic stabilization, such as other interactions in the local protein environment like hydrogen bonding or salt-bridge stabilization of a charged state. Further, a measured pK_a value is a single scalar quantity that represents an ensemble average of a highly dynamic electrostatic environment.

Our laboratory has been interested in building a dataset with spectroscopic measurements that are directly correlated to electric field and could serve as an alternative benchmark for efforts to design, test, and validate computational models and strategies. Along with other laboratories, we have been pursuing the vibrational Stark effect (VSE) spectroscopy as an alternative to pK_a measurements to measure electric fields in biological systems.[12, 18-20, 28, 29, 80, 81, 89, 101-103] In particular, we measure the vibrational absorption spectra of nitrile moieties. Nitriles are convenient biomolecular probes because they are small, absorb in an uncluttered region of the protein vibrational spectrum, have reasonable oscillator strength, and can be incorporated virtually anywhere within a biomolecular structure.[15, 27, 28, 104] These advantages have allowed us to measure vibrational spectra of nitriles in lipid membranes, protein interiors, protein-protein interfaces, and protein active site.[25, 26, 29-33, 102] Shifts in the vibrational energy of nitrile groups can be directly related to a local electric field through the linear vibrational Stark equation:[105]

$$\Delta E = hc\Delta\nu = -\Delta\vec{\mu} \bullet \Delta\vec{F} \qquad \text{[Equation 4.2]}$$

where ΔE is the change in absorption energy of the chromophore in response to a change in local electric field, $\Delta\vec{F}$, and $\Delta\vec{\mu}$ is the difference dipole moment of the vibrational transition. For nitriles in particular, $\Delta\vec{\mu}$ has been well-characterized.[16-18] Through this equation we can directly interpret differences in vibrational energy as differences in the magnitude and direction of the local electric field in the immediate vicinity of the nitrile.

Previously, we have shown that, 1) the pK_a shifts on the fluorophore of superfolder green fluorescent protein (hereafter, GFP), 2) linear electronic Stark shift of the same probe, and 3) VSE shifts of a nearby nitrile probe all responded similarly to nearby point-mutations.[91] This led us to the conclusion that the vibrational spectra of nitrile probes could be used as an orthogonal measurement of electric field to pK_a shifts, augmenting the datasets used for benchmarking electrostatic models in future computational studies.

One major caveat to the above interpretation of nitrile spectra is that nitriles can accept hydrogen bonds, which causes frequency shifts that are inherently quantum mechanical and thus are not described by eq 4.2.[20] Moreover, the specific geometry of the hydrogen bonding interaction changes the magnitude and direction of the frequency shift. Ab initio calculations by Choi et al. showed that linear, σ-hydrogen bonds blue shift the nitrile frequency by withdrawing electron density from an antibonding orbital of the CN bond, and perpendicular, π-hydrogen bonds red shift the nitrile frequency by withdrawing electron density from a bonding orbital.[89] Recently, we demonstrated that these contributions from hydrogen bonding can dominate the observed frequency of nitrile probes in GFP,[90] and therefore interpretations of nitrile frequency according to eq 4.2 require careful control experiments, often coupled with molecular dynamics (MD) simulations, to reveal the extent of potential hydrogen bonding interactions.

This complication is not unique to nitrile vibrational probes, however, because pK_a probes are similarly affected by local interactions. The proton transfer process of a pK_a probe adds or removes a hydrogen that may be involved in hydrogen bonding. Nearby hydrogen bond interactions may preferentially stabilize either the charged or neutral state of the probe, affecting the observed ΔpK_a. Further, since all titratable amino acids have multiple potential hydrogen bond donors or acceptors, the stabilization effect of hydrogen bonding on either the charged or neutral state of a pK_a probe is likely more difficult to

predict than for nitriles, which only have one lone pair that may participate in hydrogen bonding.

Because both pK_a and nitrile probes are affected by hydrogen bonding interactions, it has been suggested that they are mostly measuring changes in the level of solvation.[36, 106, 107] While the level of solvation certainly plays a role in both the ΔpK_a measurements and vibrational frequencies of nitriles, the effect is likely more complicated for measurements of ΔpK_a, since the difference in solvation energy between the charged and the neutral state can be substantially different. However, the difference in solvation free energy between the ground and excited states of a nitrile is negligible. In our recent study of hydrogen bonding to nitriles in GFP, we attempted to resolve some of the challenges of the local effects. In that work, we demonstrated that the frequency temperature line slope (FTLS) of the nitrile absorption energy was a quantitative tool for measuring hydrogen bonding, as had been postulated by Adhikary et al.[90, 107] Further, we demonstrated the necessity of such a tool; in that system, the hydrogen bonding contribution to the nitrile frequency dominated the absorption frequency, and every single probe location experienced hydrogen bonding. Nevertheless, this work demonstrated that it is possible to account for the hydrogen bonding contribution to the nitrile absorption spectra, potentially allowing for the nitrile absorption energy to be interpreted according to eq 4.2.

Both pK_a and VSE measurements of electric field require a site-specific molecular probe. pK_a probes are limited in that they must be titratable and the probe must change its charge state during the measurements. Large scale conformational changes of the protein around the charged state can convolute the interpretation of the pK_a measurement.[6, 94, 97] By contrast, VSE probes are sensitive to more subtle electrostatic perturbations and only rely on a vibrational transition. While the dipole moment changes between the ground and excited vibrational states, this difference is significantly less perturbative to the protein

structure. Further, because nitrile groups are small, the insertion of a nitrile is minimally perturbative to the protein structure.[108]

Here, we report nitrile absorption measurements of ten nitrile locations in SNase (illustrated in Figure 4.1) at sites where previous pK_a shift measurements have been reported. We show that there is poor correlation between the nitrile absorption frequencies and the previously published ΔpK_a values at the same locations within the protein, indicating the inequality of these two data sets. We hypothesize that the differences between the two measurements are due to differences in the response of each molecular probe to local interactions. Using MD simulations and temperature-dependent FTIR experiments, we provide further evidence that the FTLS is a quantitative measurement of the hydrogen bonding status of nitrile probes. Consistent with our previous work,[90] we show that carefully controlling for hydrogen bonding to any nitrile probe is essential to interpreting its mean vibrational frequency. Overall, though we show that ΔpK_a and nitrile vibrational spectra are not equivalent and both strategies are convoluted by local effects such as hydrogen bonding, the information contained in the spectral line shapes of the nitrile are nonetheless valuable. Further, in the case of nitrile probes, additional experiments such as FTLS provide a diagnostic tool for quantifying the extent of hydrogen bonding *in situ*. The additional information contained in the line shape of nitrile vibrational spectra provide a more robust dataset that can be used to benchmark electrostatic models and improve the prediction and understanding of complex electric fields in biological systems.

This work includes a significant number of MD simulations that were performed by Jeremy First. Those data are not included in this dissertation except where directly compared to experimental measurements for the purposes of discussion. In those cases, data resulting from those calculations will be identified in text and Figure captions.

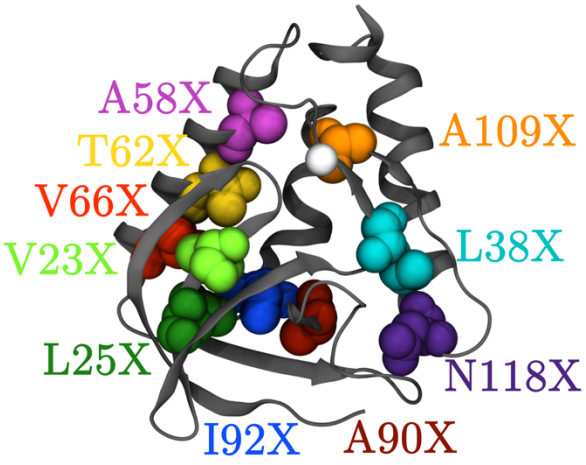

Figure 4.1: Locations of the nitrile probes in Staphylococcal Nuclease (SNase). Each location represented by the colored spheres was independently mutated to a cysteine, which was cyanylated through post-translational modification to cyano-cysteine (CNC). The first letter indicates the one letter code of the WT residue that was replaced by CNC, denoted by "X". The black ribbon shows the backbone of SNase, and the white sphere shows the location of the native Ca^{2+} ion.

4.2: Selecting and Characterizing Nitrile Probe Locations in SNase

Measuring the pK_a shifts of ionizable residues *in vitro* has long been a strategy for estimating electrostatic effects, such as apparent dielectric, in protein interiors. More recently, vibrational spectroscopy of nitriles placed site-specifically in proteins has been an alternative method for quantifying electrostatic effects in protein systems. In order to compare the merits of the two strategies, we incorporated nitrile probes into 10 separate locations in SNase (illustrated in Figure 4.1) for which there are already reported values of ΔpK_a. These 10 positions were chosen to represent the full range of pK_a shifts measured by Garcia-Moreno and coworkers, as well as to represent the spatial diversity in the interior of SNase. The nitrile-containing protein constructs were assessed with CD spectroscopy to ensure that the incorporation of the probe did not alter the overall structure of the protein. The resulting CD spectra, shown in Figure 4.2, show that the probe did not change the structure of the protein, as expected.

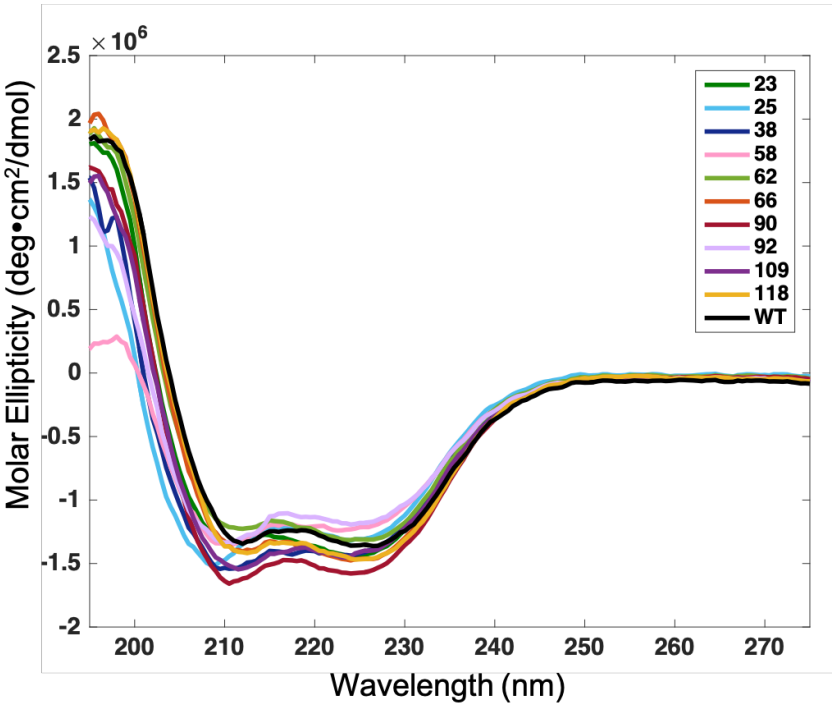

Figure 4.2: CD spectra of 11 constructs of SNase in deionized H_2O labeled by location of CNC probe.

4.3: Steady State FTIR Measurements of SNase Mutants

For each of the ten nitrile containing protein systems, FTIR spectra were collected, and representative spectra are shown in Figure 4.3. The mean frequencies for each nitrile location are given in Table 4.1. The most red-shifted peak, A90X, had a mean frequency of 2156.6 cm^{-1}. V66X was nearly as red-shifted with a mean frequency of 2157.1 cm^{-1}. The full width at half maximums (FWHM) of the spectra, which qualitatively describe the environmental heterogeneity experienced by a probe, were small: 4.2 cm^{-1} and 3.6 cm^{-1}, respectively. This suggests that the probes were in a homogeneous environment at those positions. A109X and T62X were relatively red-shifted with mean frequencies of 2158.6 cm^{-1} and 2159.6 cm^{-1}, respectively. The FWHMs of these two probe locations were larger than both A90X and V66X and were not well described by single Gaussians. A109X showed a broad absorption peak (8.2 cm^{-1}) and indications of multiple populations contributing to the overall spectrum. T62X was not quite as broad (5.3 cm^{-1}) but had a red-shifted shoulder compared to the main peak, suggesting that this probe experienced at least two different chemical environments. V23X and L25X had mean frequencies in the middle of our data set, at 2160.1 cm^{-1} and 2161.4 cm^{-1} respectively, and both peaks were fairly narrow with FWHMs of 4.1 cm^{-1} and 4.8 cm^{-1}, respectively. Interestingly, the top of the L25X peak appeared slightly wider than a single Gaussian, suggesting the possibility of two very close and equally represented peaks contributing to the overall line shape. L38X and I92X had similar mean frequencies (2161.7 cm^{-1} and 2162.0 cm^{-1}, respectively) but different line shapes. L38X had a very broad peak, with FWHM of 8.6 cm^{-1}, indicating significant heterogeneity in the environment sampled by the probe. By contrast, I92X had a narrow peak (4.5 cm^{-1}) suggesting that the probe experienced a homogeneous environment. The most blue-shifted peaks, N118X and A58X (2162.2 cm^{-1} and 2162.9 cm^{-1}, respectively) were both very broad (with FWHMs of 15.6 cm^{-1} and 14.9 cm^{-1},

respectively) and indicate significant heterogeneity in the environment or large movement of the probe.

4.4: Comparing Nitrile Frequencies to pK_a Shift of Ionizable Residues

Because pK_a shifts are often used as a proxy for electrostatics to benchmark computational methods, we compared ΔpK_a values of buried lysine and glutamate residues published by Garcia-Moreno and coworkers[6, 94] against the measured nitrile frequencies at those same locations as illustrated in Figure 4.1. Figure 4.4A compares the nitrile frequencies to the reported ΔpK_a of lysine incorporated at the same locations. Figure 4.4B compares the nitrile frequencies to the reported ΔpK_a of glutamate incorporated at the same locations. In both plots, the vertical dashed line represents the pK_a of the isolated amino acid in water, and the horizontal dashed line represents the nitrile frequency of MeSCN (the small molecule CNC analog) in water. Therefore, the distance from the dashed line on both axes represents the measured perturbation by the two different types of probes. If the nitrile probes and the pK_a probes measured the same perturbations, we would expect a correlation from least perturbed (where the two dashed lines cross) to most perturbed. In the case of the lysine probe in Figure 4.4A, there was no such correlation. In the case of the glutamate probe in Figure 4.4B, there is a slight trend with several outliers, suggesting that the pK_a probe and the nitrile probe are responding to the same environment but with different contributions from local interactions. This is further supported by the fact that lysine and glutamate, though both pK_a probes, experienced different ΔpK_as in the same locations. For reference, the pK_a shift of the two different pK_a probes are compared in Figure 4.4C. Because their charged states are opposite (a positive charge for lysine and a negative charge for glutamate), it is likely that in the same protein location they interact differently with the surrounding protein structure. Indeed, glutamate and lysine side chains

have different size, flexibility, hydrophobicity, hydration, polarity, hydrogen bonding potential, and charge density.[6, 109] In addition to the difference in charged state, lysine and glutamate can participate in different hydrogen bonds. The amine group on the side chain of lysine can donate up to three hydrogen bonds, while the carboxylate group of the glutamate side chain can accept multiple hydrogen bonds. These differences in possible local interactions likely lead to differences in the stability of the charged and neutral states between the two different pK_a probes, resulting in discrepancies in ΔpK_a which are directly related to electric field. While hydrogen bonding is difficult to measure *in situ* for such pK_a probes, the FTLS of nitrile probes may be used to assess the hydrogen bonding status.

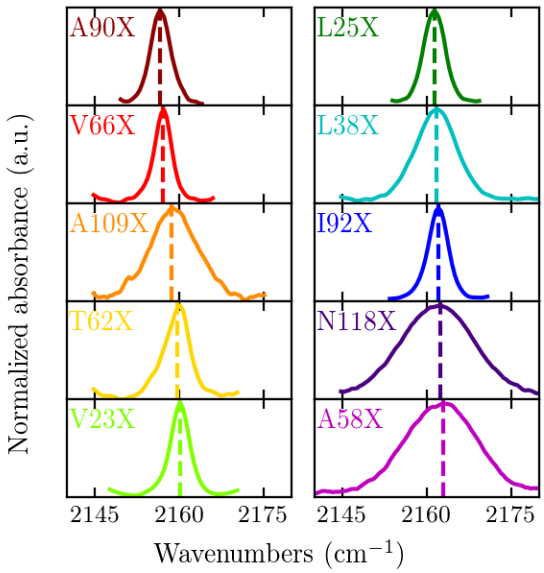

Figure 4.3: Representative FTIR absorption spectra of CNC incorporated at each of the ten locations shown in Figure 1 at room temperature, arranged from lowest mean frequency to highest mean frequency. The maximum absorbance of each spectrum was normalized to 1.

Amino acid position	Nitrile location			pK_a probe location	
	$\tilde{\nu}$ (cm^{-1})	FWHM (cm^{-1})	FTLS ($cm^{-1}/^{\circ}C$)	Lysine pK_a	Glutamate pK_a
A90X	2156.6	1.72	-0.011 ± 0.001	8.6	6.4
V66X	2157.0	1.376	-0.0083 ± 0.0025	5.6	8.5
A109X	2159.0	4.155	-0.022 ± 0.002	9.2	7.9
T62X	2159.6	2.252	-0.017 ± 0.003	8.1	7.7
V23X	2160.1	1.731	-0.0061 ± 0.0021	7.3	7.1
L25X	2161.4	1.897	-0.011 ± 0.003	6.3	7.5
L38X	2161.7	3.654	-0.027 ± 0.003	10.4	6.8
I92X	2162.0	1.681	-0.017 ± 0.001	5.3	9
N118X	2162.0	6.31	-0.049 ± 0.014	10.4	4.5
A58X	2162.6	6.262	-0.052 ± 0.010	10.4	7.7

Table 4.1: Collected nitrile mean vibrational absorption frequency, nitrile spectra FWHM, FTLS values, and pKa values for lysine and glutamate residues at 10 positions in SNase. pKa data adapted from refs 6 and 94.

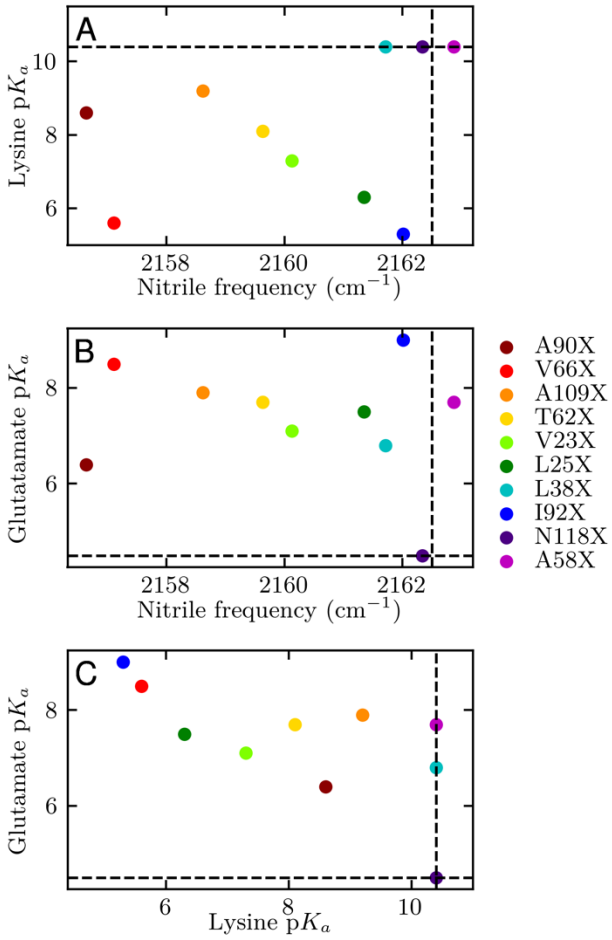

Figure 4.4: A) Reported values of pK_a shift of a Lysine residue at the 10 positions in SNase illustrated in Figure 1 compared to the measured vibrational frequency of a CNC probe at the same positions. B) Reported Values of pK_a shift of a Glutamate residue in the same positions compared to the nitrile vibrational frequencies. For A and B, the horizontal black dashed lines show the pK_a of glutamate and lysine free amino acids in water. The vertical dashed line shows the mean vibrational frequency of MeSCN in water. C) Comparison of pK_a shifts in the 10 positions in SNase as measured by lysine and glutamate pK_a probes. pK_a data adapted from refs 6 and 94.

4.5: Temperature Dependent FT-IR Measurements

In order to investigate the hydrogen-bonding environments of the different probe locations, we measured the FTLS of the nitrile probe in each location. Adhikary et al. postulated an empirical relationship between the ability of a nitrile probe to hydrogen bond and the dependence of the nitrile frequency on changes in temperature. This is due to the increase in hydrogen bond exchange and an accompanying decrease in hydrogen bond lifetime as temperature increases.[107] In systems with fewer hydrogen bonds to the nitrile, less exchange is observed and the resulting temperature dependence of the frequency shift, quantified as the FTLS, is smaller. We have previously shown that FTLS quantitatively describes the local hydrogen-bonding environment around a nitrile probe in the β-barrel of GFP.[90] As in GFP, the probe locations in SNase appear in the crystal structure (3BDC, Figure 4.1) to be buried so any contact with water is likely not bulk, but contact could still occur with multiple water molecules in a variety of orientations. To investigate this further, we measured the nitrile absorption frequency of each probe at 10 °C intervals from 5 °C to 35 °C. As expected, the change in vibrational frequency at each location was linear, and the slope of this linear dependence was taken to be the FTLS of each nitrile probe (Figure 4.5). The resulting FTLS values are listed in Table 4.1. For reference, we also plotted the frequency shift of MeSCN in both H_2O and DMSO, which allowed us to compare the measured FTLS of the nitriles in protein to the amount of hydrogen bonding the probe experiences in protic and aprotic environments, respectively.

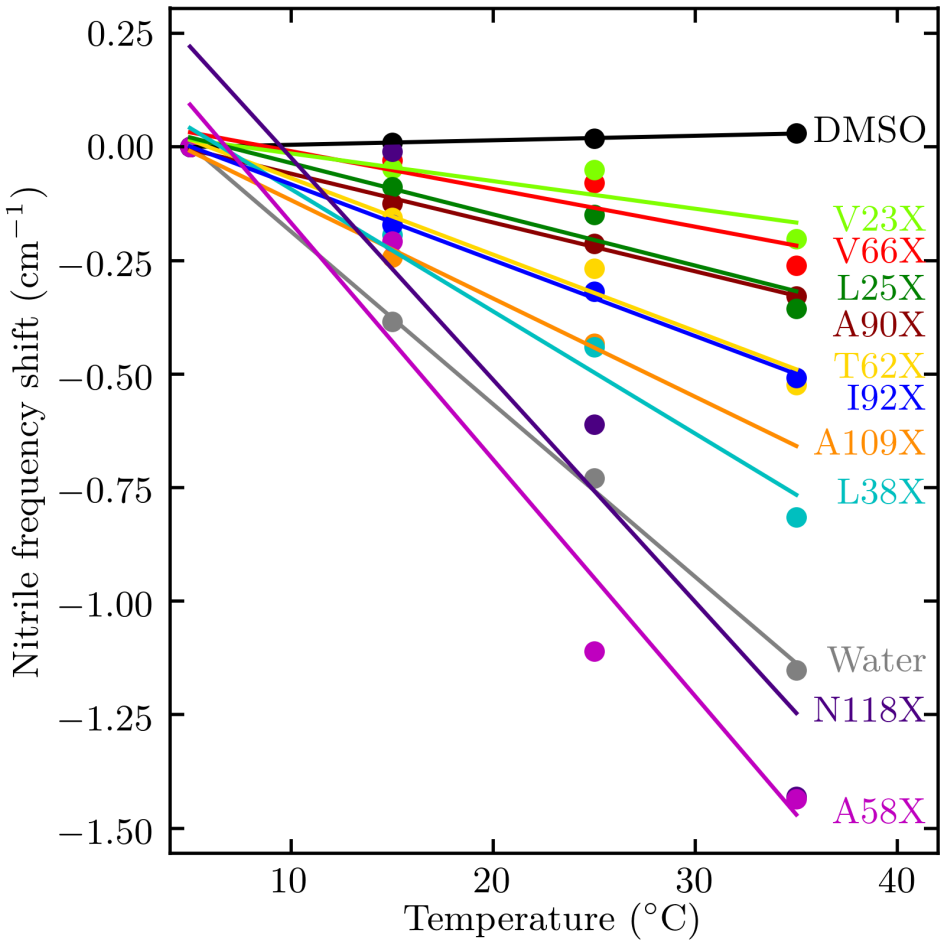

Figure 4.5: FTLS of each SNase construct. Nitrile frequency was measured at 5, 15, 25, and 35 ºC and the shift in the peak was fit to a linear regression. Measurements of MeSCN in DMSO (black) and water (grey) are used as standards to compare hydrogen bonding environment.

In the FTLS experiments, we interpret a more negative slope as more hydrogen bonding experienced by the probe and a smaller slope as less hydrogen bonding. Thus, V23X, V66X, A90X, and L25X, which have FTLS values of -0.0061, -0.0083, -0.011, and -0.0011 $cm^{-1}/^{o}C$, respectively, only experienced a small amount of hydrogen bonding. T62X and I92X (FTLS values of -0.017 $cm^{-1}/^{o}C$) experienced a moderate amount of hydrogen bonding. For the nitriles at positions A109X and L38X, the FTLS values were larger at -0.022 and -0.027 $cm^{-1}/^{o}C$, respectively, indicating more substantial hydrogen bonding experienced by the probe. Finally, the nitrile at positions A58X and N118X (-0.052 and -0.049 $cm^{-1}/^{o}C$) had FTLS values that were larger than that of water, indicating more hydrogen bonding than experienced by the probe in water. This is consistent with our observations in the previous study with GFP, where some nitrile probes had larger FTLS values than in water. In all of these cases, the probe was located in a flexible portion of the protein, which we hypothesize can sample more environments as temperature increases. This increased flexibility results in more hydrogen bonding exchange than a small molecule nitrile in water.

The FTIR mean vibrational frequency, the FWHM of the nitrile spectra, and the FTLS studies offered an experimental, steady-state method for measuring and assessing the local environment of the nitriles. Indeed, when plotted against each other, the FTLS and FWHM have an excellent correlation (Figure 4.6, $r = 0.98$) demonstrating that these two measurements could be responding to similar interactions. However, to investigate the molecular level details in each of these different environments (such as different hydrogen-bonding environments or different local electric fields), Jeremy First performed 100 ns MD simulations on each of the ten nitrile containing proteins systems and on the WT SNase protein. We calculated the geometric profiles of hydrogen bonding interactions present in the MD simulations. The nitriles at positions N118X and A58X had a broad distribution of

hydrogen bonding geometries that were donated from water molecules, consistent with partially solvent-exposed residues or interaction with unstructured water. I92X and V66X experienced far fewer hydrogen bonds to solvent (less than 1500 occurrences each out of 25,000 frames analyzed) that were also broadly distributed. This indicated a low level of interaction with unrestrained water. A90X, L25X, A109X, V23X and L38X experienced few hydrogen bonds to solvent (less than 600 occurrences each). Finally, T62X experienced a significant amount of hydrogen bonding (over 17,000 occurrences) with a narrow distribution of θ_1. Upon inspection, this population was found to result from a structural water that was stabilized by hydrogen bonding to the amide Ns of both I18 and D19 and to the carboxyl O of T22. The water molecules in this interaction were found to be extremely stable and did not exchange. For example, in one instance the hydrogen-bound water molecule had a residence time of over 40 ns.

Likewise, the nitriles experienced a range of hydrogen bonding interactions from nearby protein donors. The nitriles at positions L38X, A109X, and N118X experienced a significant amount of hydrogen bonding (over 3000 observations) from nearby protein donors. The nitrile at positions A58X and L25X experienced a small amount of hydrogen bonding from protein (less than 1700 occurrences). The nitriles at positions V23X, A90X, V66X, I92X, and T62X experienced almost no hydrogen bonding interactions from protein (less than 400 occurrences each). It is important to note that in all probe locations the nitrile was observed to be involved in some hydrogen bonding interactions, either with water or with the protein itself. This is likely true for pK_a probes in these same positions. Crystal structures of several pK_a probes incorporated into SNase show instances where the probe is in a position to accept or donate a hydrogen bond to a nearby residue or crystallized water.[110]

As discussed above, the FTLS of the nitrile vibrational energies can be used to measure the hydrogen-bonding environment of the nitrile location, providing an experimental diagnostic to mitigate this complication. We compared the absolute number of hydrogen-bonding observations throughout the 100 ns MD trajectories performed by Jeremy First against the experimental FTLS. Note that we did not consider the structural hydrogen bond from water for the nitrile at position T62 mentioned above. Because of the long-lived nature of these hydrogen bonds, we reasoned that, over the temperature range investigated with the FTLS experiments, this hydrogen bond likely does not exchange. Excluding this interaction, we observed a strong linear relationship (r = -0.82) between the experimental FTLS and the number of hydrogen bonds observed in simulations (Figure 4.7). While we had previously observed a correlation between the hydrogen bonding environment and the FTLS in GFP, here we observed a similar correlation in a different protein with different nitrile probes. Further, GFP has a water filled β-barrel structure, while SNase has a more compact globular structure. The fact that we observe the same relationship in such structurally different proteins provides further evidence of the relationship between FTLS and hydrogen bonding and gives us further confidence that FTLS may be used as a quantitative diagnostic tool of subtle differences in the hydrogen-bonding environment in a variety of protein systems.

Though these probes are all buried in the supposedly hydrophobic interior of the protein according to the crystal structure, the FTLS indicated that all of the probes experience some amount of hydrogen bonding. More interestingly, a few of the probes experienced a significant amount of hydrogen bonding, in which donors were either protein atoms or water molecules. This suggests that even in the most buried environments, nitriles will accept hydrogen bonds from the best available donor. We hypothesized that, in this system, the majority of the heterogeneity experienced by this probe was due to hydrogen

bonding. This is further supported by the excellent correlation *(r* = 0.98) between FWHM and FTLS shown previously in Figure 4.6, suggesting that our hypothesis was correct, and the line shapes for these nitrile spectra were overwhelmingly determined by hydrogen bonding.

The apparent lack of correlation between the ΔpK_a values reported by Garcia-Moreno and coworkers and the nitrile frequencies in the same positions (Figure 4.4A and 4.4B), suggests that these two types of probes did not respond equally to the same interactions. Given that the lysine and glutamate pK_a probes were not related to each other for several of the locations studied here (Figure 4.4C), this suggests that local interactions play a significant and varied role in how the shifts reported by all three probes can be interpreted. In particular, the two different pK_a probes were only in good agreement for locations that were exposed to bulk-like solvent hydrogen bonding (N118X) or very little hydrogen bonding (A190X, V66X, V23X, L25X, and I92X). In these environments, it is likely that the glutamate and lysine pK_a probes interacted similarly with their surroundings. The two different pK_a probes were in poor agreement for locations that had significant hydrogen bonding, but not to bulk-like solvent (A109X, T62X, L38X, and A58X). In these locations, it is likely that glutamate and lysine are interacting differently with their surroundings. Though ΔpK_a measurements give only a single scalar value, we have demonstrated that nitrile spectra have peak widths that reflect local interactions, which our MD simulations capture *in silico*, in a manner that can be quantified through the FTLS.

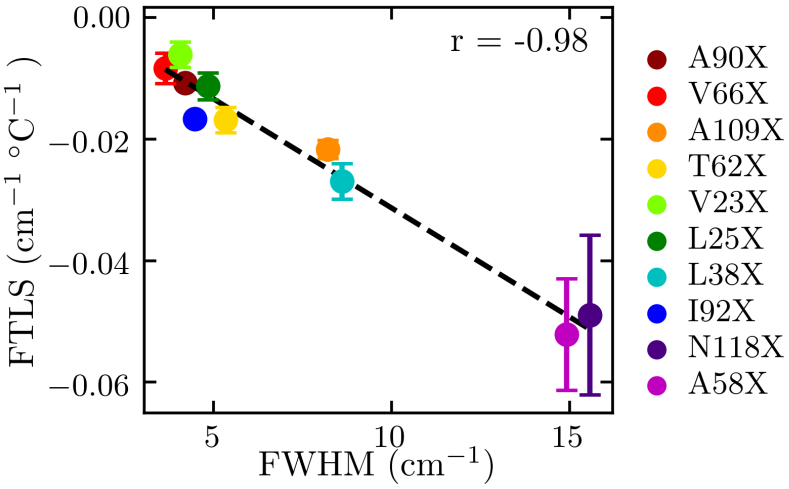

Figure 4.6: FTLS plotted against the FWHM of the experimental nitrile spectra. The dashed line represents a linear regression fit of the data.

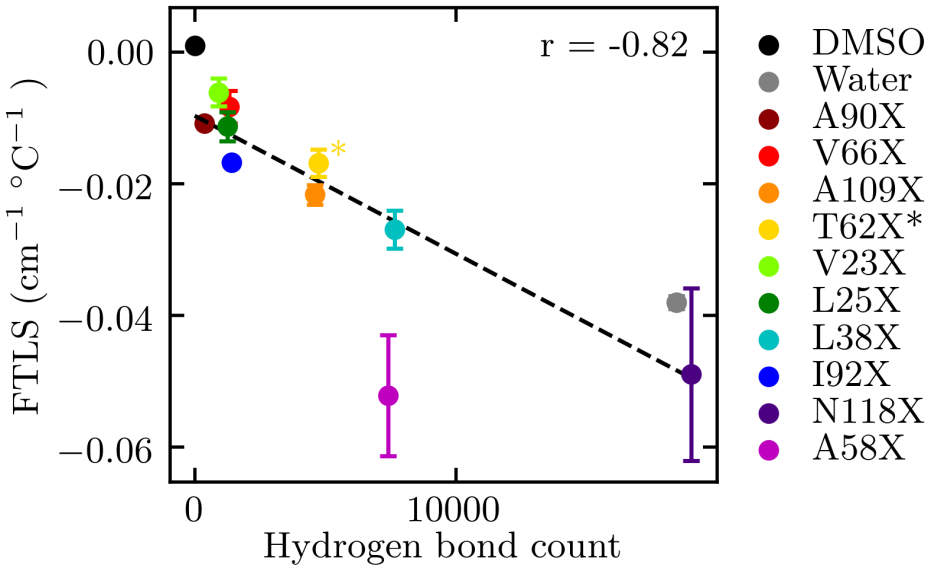

Figure 4.7: FTLS vs Hydrogen bond count calculated from 100ns MD simulations performed by Jeremy First. The dashed line represents a linear regression.

Together, this demonstrates that VSE could be a powerful reporter of electric field as long as hydrogen bonding can be quantified and accounted for. It is unclear at this point how to quantify a hydrogen bonding component within the parameters of the Stark equation. However, the work here demonstrates that hydrogen bonding can be accounted for empirically as a control. In systems where there is a single nitrile location reporting on different perturbations, it is reasonable to interpret nitrile shifts as reporters of field as long as the hydrogen bonding experienced by the probe is consistent in each state. For measurements in proteins, this is likely only possible when the nitrile location remains constant and perturbations are made around the nitrile probe. We have previously shown that this strategy can effectively measure differences in electric field by comparing to an independent reporter of field,[26] and we have used this strategy to measure electrostatic contributions from oncogenic mutations in p21H-Ras.[32, 88] In more complex experimental simulations, FTLS and MD simulations are convenient methods that can be used to confirm the consistency of hydrogen bonding.

4.6: Conclusions

The apparent lack of correlation between the ΔpK_a values reported by Garcia-Moreno and colleagues and the nitrile frequencies in the same positions, suggests that these two types of probes are not responding equally to the same interactions. Given that the lysine pK_a probes and the glutamate pK_a probes were not correlated to each other suggests that these two pK_a probes respond to local environment differently; local environment clearly plays a significant role in how the shifts reported by all three probes are interpreted. Though ΔpK_a measurements give only a single scalar value, we have demonstrated that nitriles have a line shape that reflects on the local interactions in a manner that can be quantified with FTLS. We have also shown that MD simulations performed by Jeremy

First capture these local interactions *in silico.* While nitrile probes and pK_a electrostatic probes respond differently to local interactions, nitrile vibrational spectra have the distinct advantage in that they can, 1) be directly related to electric field through the Stark equation, 2) offer additional information from the spectral line shape that indicates contributions from subpopulations of the probe, and 3) their local interactions can be quantitatively accounted for with additional control experiments. This indicates that libraries of nitrile spectra are a valuable resource for validating computational models and, when properly controlled for, for reporting quantitative information about electric field in proteins. Further investigation of decoupling local interactions from overall electronic contributions to the nitrile spectra will allow for a greater understanding and increased predictability of the complex electric fields that dominate biological systems.

Chapter 5: Development of the Arf/ARNO/Brefeldin-A System for Investigating Inhibition of Protein-Protein Interactions

5.1: Introduction

ADP Ribosylation Factor 1 (Arf) is a GTPase in the Ras superfamily which contains proteins that regulate cell proliferation and vesicle transport.[111] Though GTPases are relatively small, they bind to multiple effector proteins which control GTPase cycling as described in Chapters 1 and 3. Interest in these small GTPases and their various effectors began with the discovery of the Ras oncogene, which was quickly followed by work on many related proteins in the superfamily. Arf was discovered as part of a study of cholera toxin in 1986 in which the authors found that Arf acted as a protein cofactor necessary for efficient ADP ribosylation, though Arf is now known for diverse signaling activity. This and many other subsequent discoveries of Ras-like GTPases led to the proteins being organized into subfamilies, the Arf subfamily being primarily responsible for regulation of intracellular traffic. This subfamily of proteins is unique among the Ras superfamily because they undergo a much larger conformational change during GDP/GTP exchange than any of the other subfamilies, which has implications for future drug discovery efforts.[58]

Arf alone cannot execute its many responsibilities in the cell. Instead it binds with different protein factors to regulate each task. The interaction of the Arf subfamily proteins with their GEFs are the most well understood of the regulatory pathways. Specifically, the Arf1 exchange factor Gea1p (Gea) in *Saccharomyces cerevisiae* (yeast) has been successfully crystallized and studied over the past twenty years. The smaller human equivalent called ARNO has also been explored in depth more recently. All Arf subfamily GEFs contain a conserved Sec7 domain of approximately 200 amino acids, and this domain is the portion that interacts directly with Arf subfamily GTPases. GEFs such as Gea bind

to Arf in its GDP bound OFF state, and disrupt the nucleotide binding pocket on Arf to cause the disassociation of GDP.[112] High concentrations of GTP in healthy cells result in GTP quickly binding to the site, destabilizing the Arf-GEF interaction thus completing the exchange. The catalytic cycle of Arf is illustrated in Figure 5.1.

The Arf subfamily is responsible for the regulation of intracellular traffic and the formation of vesicles used for transport between cellular organelles, particularly the Golgi body and the endoplasmic reticulum. The fact that both Arf and Gea proteins each have two genes that are functionally redundant highlights their importance for healthy cell function. Fluorescence experiments have shown that Arf is located in the Golgi apparatus, and mutations to Arf have shown widespread phenotype changes, highlighting its ubiquity. The varied biological roles of Arf subfamily proteins include regulating the membrane association of coat proteins and the regulation of phospholipid synthesis for membrane trafficking. Though each Arf subfamily protein may carry out a slightly different role, the overarching purpose of these proteins is to regulate the creation and movement of vesicles in cellular organelles. This job is so important that incubation of the Golgi body with Brefeldin A (BFA, a known Arf/GEF complex interfacial inhibitor) for less than 10 min causes the organelle to entirely disassemble.[113]

Arf is a relatively small globular protein of about 160 amino acids consisting of multiple α-helix and β-sheet motifs. It has a stable switch I region conserved in Ras superfamily proteins that is crucial for interacting with their respective nucleotide exchange factor proteins. The Sec7 domain of Gea, the portion of the protein used in our experiments, is about 200 amino acids long and the secondary structure consists of only helices and random coils. It has been established that the Sec7 domain is the only part of Gea that executes exchange activity, though it has been suggested that the remaining domains of Gea and other GEFs could directly or indirectly contribute to specificity.[114] The binding of

these two proteins is accomplished by engaging the switch I and switch II regions of Arf by locking them into hydrophobic grooves between helices in the Sec7 domain (Figure 5.2). There are two mechanisms that this enzyme complex is concerned with in this context: 1) its nucleotide exchange (removing GDP and allowing new GTP to bind); and 2) its inhibition by BFA which prevents the complex from dissociating creating a dead end in the catalytic cycle.

Nucleotide exchange of *in vivo* Arf that is bound to GDP occurs through a multistep process (shown in Figure 5.2) that begins when the n-terminal helix tail locks the β-strands between switch 1 and switch 2, which blocks exchange until the enzyme binds to a membrane The N-terminal tail helix is amphipathic which releases the β-strands to bind to the membrane.[115, 116] As the β-strands shift, they change the conformation of Arf so it can bind GTP. GEFs, like Gea and ARNO, bind to Arf to catalyze the removal of the more tightly bound GDP, allowing GTP to bind to Arf. The Sec7 domain carries a conserved glutamate at the end of a helix that crosses the binding plane. This 'glutamic finger' dislodges a Mg^{2+} ion in the nucleotide binding site, disrupting GDP binding and creating a free binding site for GTP.[117] Arf can then dissociate from the membrane freely and continue the cycle. *In vitro*, the amphipathic helix tail on Arf is often cleaved, as it is in this work, so that the regulation of the cycle is not dependent on binding to a membrane. The most important residue for nucleotide exchange is not in the Arf binding site, but instead is the glutamate (E197 on Gea) that electrostatically disrupts the binding site.[117] Studies have determined that a charge reversal mutation to lysine at this position prevents nucleotide exchange but not the binding of the GEF, and the resulting Arf-GDP-GEF intermediate can be trapped. Models of the binding site indicate that the Mg^{2+} in the binding site interacts with the terminal phosphate group of GDP and assists in stabilizing other amino acids at the phosphate region of the binding pocket.

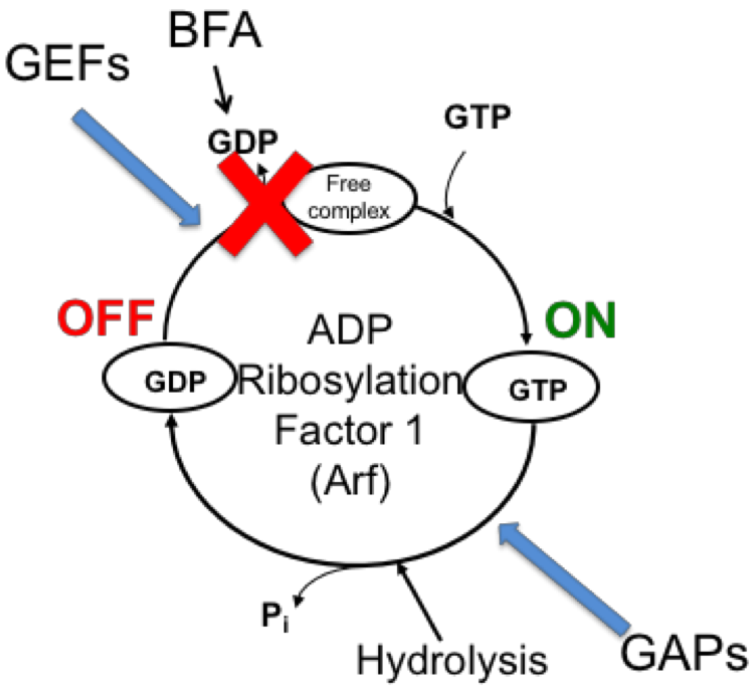

Figure 5.1: Catalytic cycle of the interactions of Arf with GAP and GEF binding partner proteins. BFA inhibits this cycle by binding to the interface between the Arf and GEF and stabilizing the transient protein-protein complex.

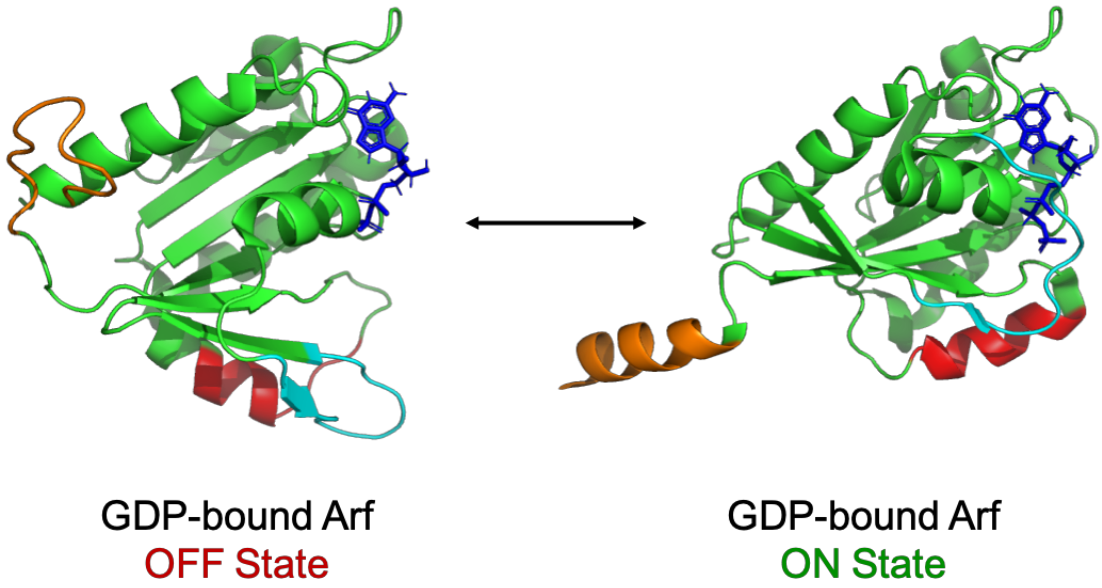

Figure 5.2: Arf Crystal structure before and after nucleotide (blue) switch, showing reorganization of switch I (cyan) and switch II (red). *In vivo,* an N-terminal helix region (orange) that is exposed when the structure converts from the OFF state (left) to the ON state (right) allows the protein to associate with the cell membrane.

Interfacial inhibition occurs when an inhibitor molecule binds selectively to an interface between either a protein and DNA or between two proteins. It is analogous to an inhibitor that targets a transition state, but in this case the transition state is the transient binding of two proteins which come together to perform a specific task and then dissociate. The inhibitors trap complexes in a specific state that prevents them from carrying out their catalytic purpose.[118] They target these interfaces specifically, making use of temporary structural motifs and electrostatics to create a drug binding site that otherwise does not exist. Interfacial inhibitors represent a relatively new and very interesting set of drug targets. Large faces of proteins are typically thought of as being nearly undruggable because of their large size and lack of features.[118] Instead, drug discovery has largely focused on targeting ligand binding sites. This strategy becomes impossible with proteins like GTPases. The sheer number of proteins that cleave GTP to GDP all with relatively similar binding motifs makes the toxicity of any possible lead or analog unviable. Interfacial inhibition represents nature's solution to targeting a protein interface. The specificity the drug requires to bind only to the correct protein and not to other proteins is accomplished by the target protein itself binding to another protein. The pocket formed when two proteins bind is highly specific, and the natural products that have been found to inhibit them are equally as specific.

BFA inhibits the nucleotide exchange process by stabilizing a hydrophobic pocket at the interface of Arf and Gea.[119] Two-thirds of BFA is in contact with Arf and one third with Gea, and nearly all the interactions are with hydrophobic residues, though there are a three hydrogen bonds that orient the molecule.[120] A two-dimensional representation of the binding site is shown in Figure 5.3. The 5-member ring is sandwiched between two aromatic side chains, while its unique 13-member lactone ring undergoes almost no conformational change upon binding. BFA binds only to the complex and not to either

protein individually, because the two aromatic rings that stabilize the 5-membered rings, from a tyrosine and tryptophan residue respectively are only available for binding when the inter-switch region is opened and the nucleotide exchange process has started. The pocket is closed by hydrophobic coils in both Arf and Gea, suggesting that BFA binds the 5-membered ring first with polar interactions followed by the pocket closing around it, meaning the pocket opens on the opposite side from the aromatic residues.[58]

This binding model is supported by systematic mutations to specific binding site residues which can confer BFA sensitivity in ARNO or confer BFA resistance in Gea. These studies showed that BFA interacts directly with only the aromatic tyrosine and tryptophan residues which create both polar contacts and aromatic stabilization of the 5-membered ring. The rest of the residues form hydrophobic interactions with the larger 13-membered ring of BFA and to some extent are necessary so that the size of the pocket is maintained. Further experiments to modify BFA to determine possible analogs have shown that both oxygen atoms that make the hydrogen bonds are necessary to the specificity and activity of BFA, and other derivatives that change the shape of the lactone ring are also unviable.[117] In this case it can be reasonably concluded that the activity and specificity of BFA is a result of such an exact structural and chemical fit, and the failure of BFA derivatives shows the precision that would be required in rationally designing an interfacial inhibitor.

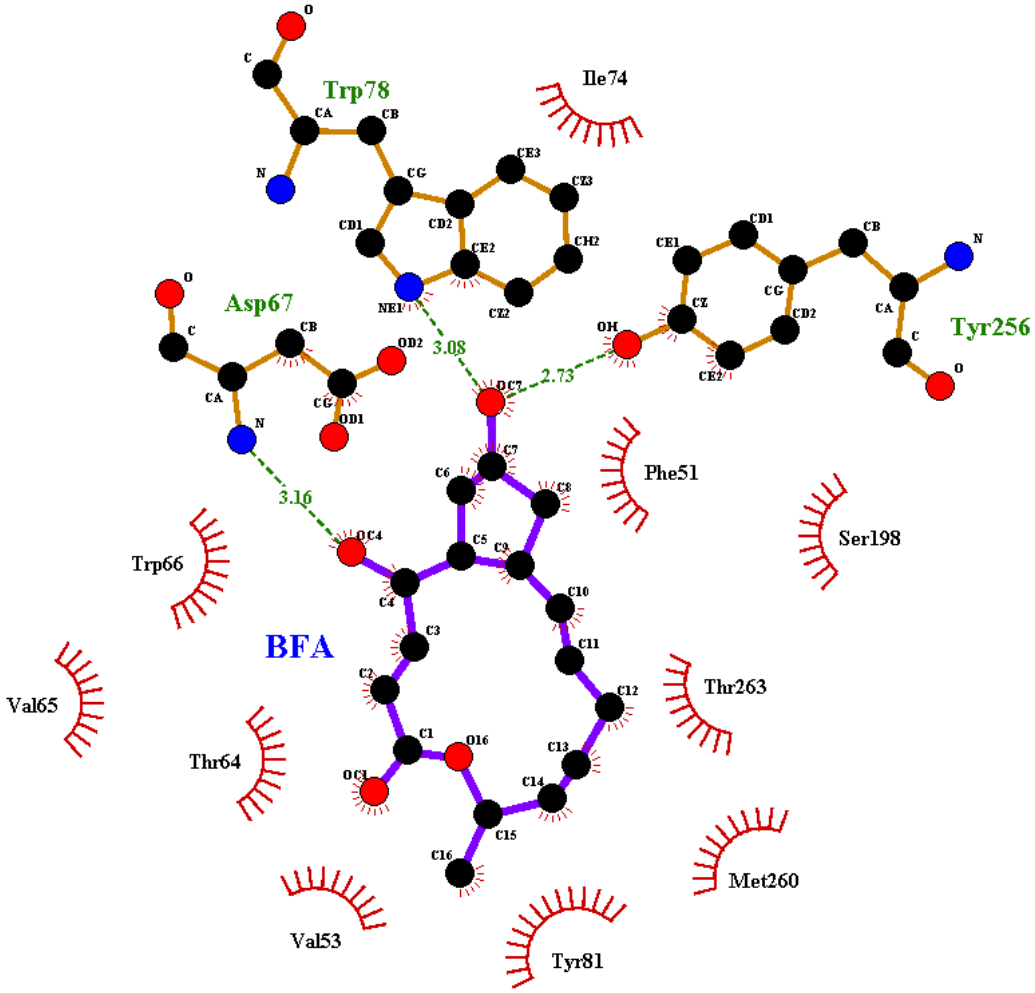

Figure 5.3: Two-dimensional representation of BFA bound to the interface between Arf and Gea. The asparagine at position 67 on Arf, the tryptophan at position 78 on Arf, and the tyrosine at position 256 on Gea form three hydrogen bonds on the smaller 5-membered ring of BFA while several residues on both proteins form hydrophobic contacts that sandwich the larger 13-membered ring of BFA.

Though BFA demonstrates the utility of interfacial inhibition, it is not a practical drug lead. Yeast Gea is sensitive to BFA, but the human Arf exchange factor ARNO is not.[119] Understanding which residues are essential for BFA sensitivity is a question that has dominated the work on this enzyme system in the last decade. Several residues and combinations of residues have been discovered to confer varying amounts of BFA sensitivity on ARNO, including the version used here called ARNO4M, which contains four BFA-sensitizing mutations, F190Y, A191S, S198D, and P208M. This information will be important for targeting not just Arf but the entire Ras superfamily because these enzymes regulate cell division.

The purpose of this work is to use our group's expertise in VSE spectroscopy to interrogate the electrostatic mechanisms of Arf/GEF binding and inhibition with BFA. Here, we placed nitrile probes on both sides of the protein-protein interface to measure electric field. The nitrile probe's response to the perturbations of protein docking and inhibition can be related to electric field through the Stark equation (equation 1.2). By incorporating probes in many locations in the protein area of interest, the combined results will contribute to an electrostatic map of the Arf/GEF catalytic cycle which will help elucidate the specific interactions and general properties that make BFA an effective interfacial inhibitor. In a broader sense, understanding how the structure and electrostatic field of BFA can inhibit a protein interface will yield valuable information about designing and validating new interfacial drug candidates to treat difficult diseases that have not otherwise been targeted successfully.

5.2: Results and Discussion

Our goal was to place nitrile probes on both sides of the Arf/Gea interface and observe the electrostatic effects of protein binding and interfacial inhibition with a nitrile vibrational probe. Several probe locations were chosen on Arf and Gea, as shown in Figure 5.4, which were incorporated into the protein as described in Chapter 2. For each probe, we aimed to measure vibrational spectra of the probe-containing protein monomer, the docked complex, and the complex inhibited by BFA. First, we measured the vibrational frequency of the nitrile probe incorporated into three monomeric Arf constructs as described in Chapter 2: Arf F51C_{SCN}, Arf I74C_{SCN}, and Arf L21C_{SCN} (Figure 5.5). All three probes have absorption frequencies around 2161.5 cm^{-1} and peak widths around 14.5 cm^{-1}, although the spectrum of position 51 is slightly wider or contains a shoulder. All of these frequencies are characteristic of a nitrile probe in a solvent exposed environment, which is expected for these positions in Arf when the protein is in its monomeric form.

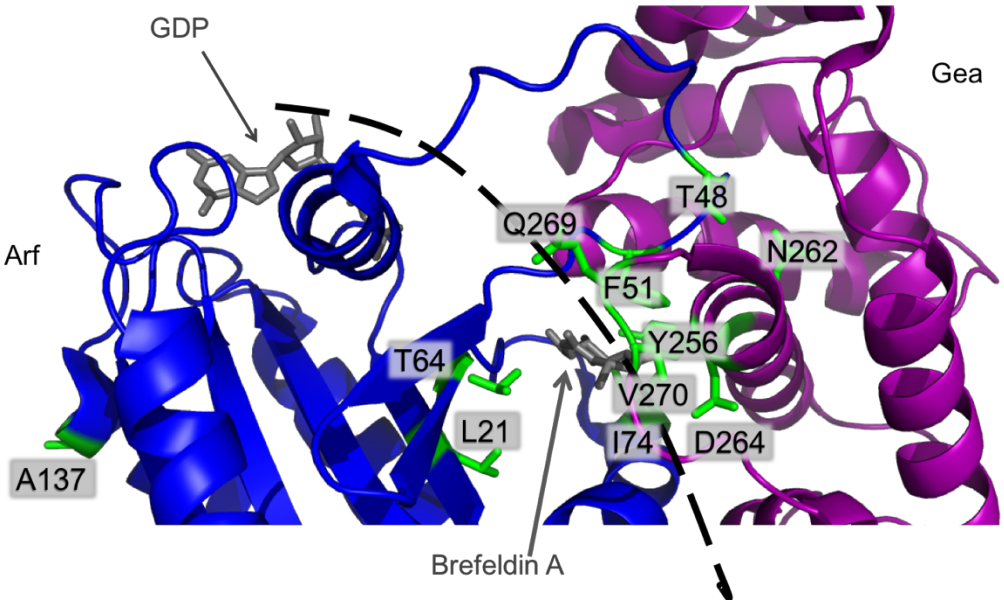

Figure 5.4: Crystal structure of Arf/Gea protein complex (pdb: 1RE0) with the locations of nitrile probes labeled. GDP is labeled in the binding site of Arf and BFA is labeled at the interface between Arf (blue) and Gea (pink). The dashed line shows the interface between the two proteins.

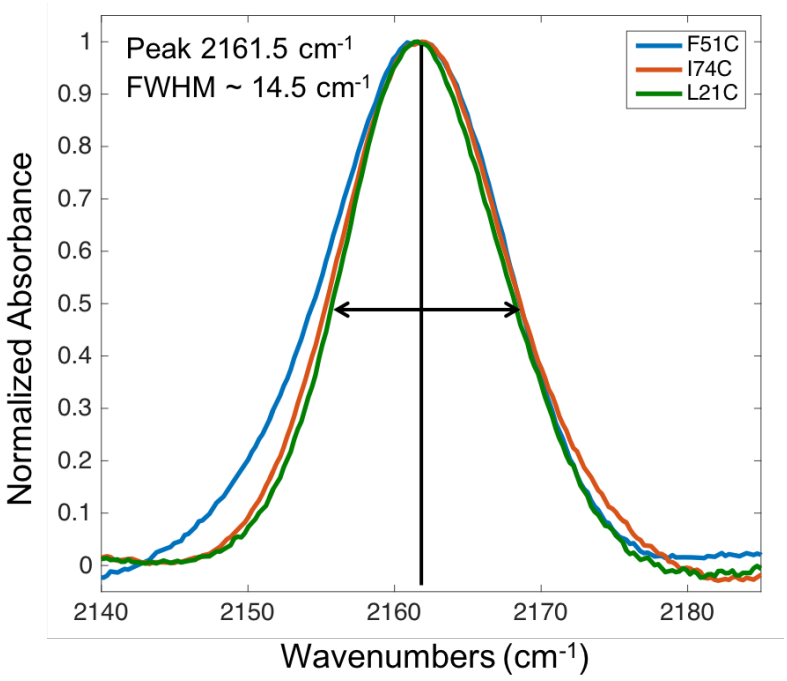

Figure 5.5: FTIR spectra of the nitrile stretching frequency in three constructs of Arf labeled with a nitrile probe. The blue line shows the absorption spectrum of the nitrile probe at position 51, the orange line shows nitrile at position 74, and the green line shows the nitrile at position 21.

Next, we aimed to combine Arf and Gea into a complex by incubating the two proteins at a 2:1 ratio, in which the more abundant protein (in this case Gea) does not contain the probe. This ensures that the equilibrium is sufficiently in favor of the complex to avoid inadvertently measuring probe frequencies on unbound Arf. These results for the probe at position 51 in Arf are shown in Figure 5.6. Compared to the monomer, the nitrile frequency in the docked complex blue-shifted by 2.45 cm^{-1} and the spectrum broadened by 4 cm^{-1}. We expected that the peak would narrow and redshift as the probe environment went from solvent exposed in the monomeric form to buried in the docked complex. Instead, the peak blue shifted and broadened, which are both suggestive of hydrogen bonding to the probe. Hydrogen bonds are known to complicate the interpretations of Stark shifts, and previous work in our group has demonstrated that shifts due to hydrogen bonding can dominate in certain conditions making direct interpretation of electrostatics significantly more difficult. Further work characterizing the hydrogen bonding to nitrile probes, similar to strategies used with SNase in Chapter 4, are necessary.

To investigate whether the probes were affecting the structure or docking of the proteins, we performed kinetics experiments with a fluorescently labeled nucleotide as described in Chapter 2. Figure 5.7 shows a sample time course measurement. We expected an increase in fluorescence as Gea catalyzes the removal of GDP from the Arf binding site and new, fluorescently labeled GTP is taken up in the binding site, indicating a completed catalytic cycle. Fluorescence increases as the labeled GTP moves from a quenching buffer environment to the buried non-quenching environment of the protein active site. Table 5.1 shows the observed rates measured for the WT and three mutant constructs of Arf. For WT Arf we measured a turnover rate of $0.82 \pm 0.02 \times 10^{-2}$ s^{-1}. For Arf F51C_{SCN}, Arf I74C_{SCN}, and Arf L21C_{SCN}, we measured rates of $2.5 \pm 0.6 \times 10^{-2}$ s^{-1}, $1.3 \pm 0.1 \times 10^{-2}$ s^{-1}, and $1.08 \pm 0.06 \times 10^{-2}$ s^{-1}, respectively.

All three mutated forms of Arf that we measured had faster GDP to GTP exchange rates in the presence of Gea than the WT. This was an unexpected result because we generally assume that nature has done a better job optimizing a particular cellular process than any alternative we engineer. However, there is at least one example from our work with Ras where an engineered mutant had a faster measured rate than the WT. Further work is necessary to confirm these measurements and measure the rates of additional mutants.

5.3: Future Directions

Because of significant experimental challenges related to the instability of Gea, we have transitioned from using Gea to using ARNO as the GEF of interest in these systems. Originally, Gea was the preferred choice because it is the native target of BFA when complexed to Arf. However, Gea was limited by its instability as well as the fact that it does not exist in humans, so any detailed understanding might not translate well to human GEFs. ARNO is the human GEF that interacts most frequently with Arf, but it is insensitive to BFA. However, there are four known mutations to ARNO that confer sensitivity to BFA, F190Y, A191S, S198D, andP208M, which results in the ARNO4M construct. We have redesigned the genes to contain both a TEV protease cleavage site and a thrombin cleavage site to enable a faster and more streamlined purification protocol that puts less stress on the proteins. The new genes for both of these proteins are now in routine use in our lab. To minimize the instability issues that Gea suffered from, we have made a significant effort towards optimizing the expression and purification protocols of these proteins, as described in Chapter 2. In spite of these challenges, our group is now well positioned to measure electrostatics in this system moving forward.

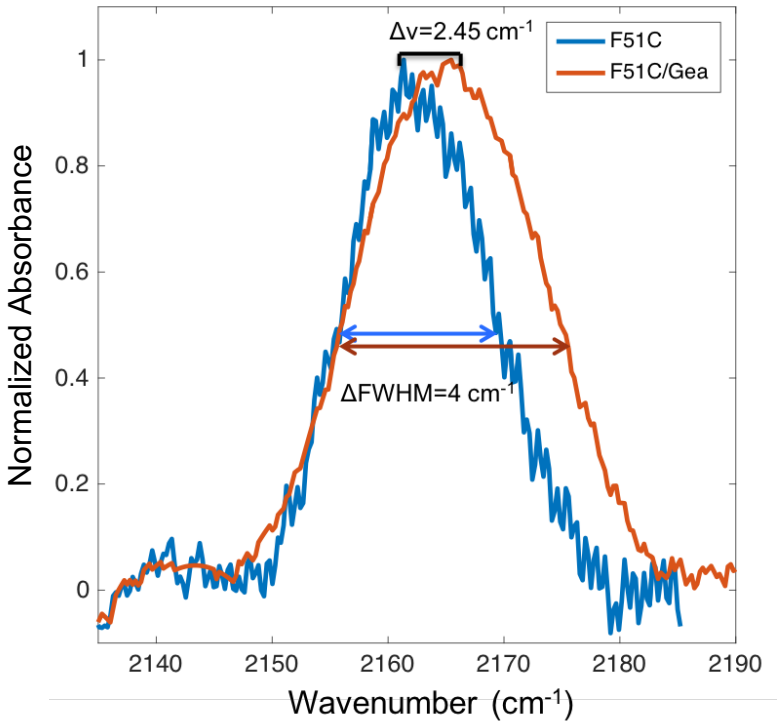

Figure 5.6: Nitrile absorption spectra for Arf at position 51 in monomeric form (blue) and in a docked complex with Gea (orange)

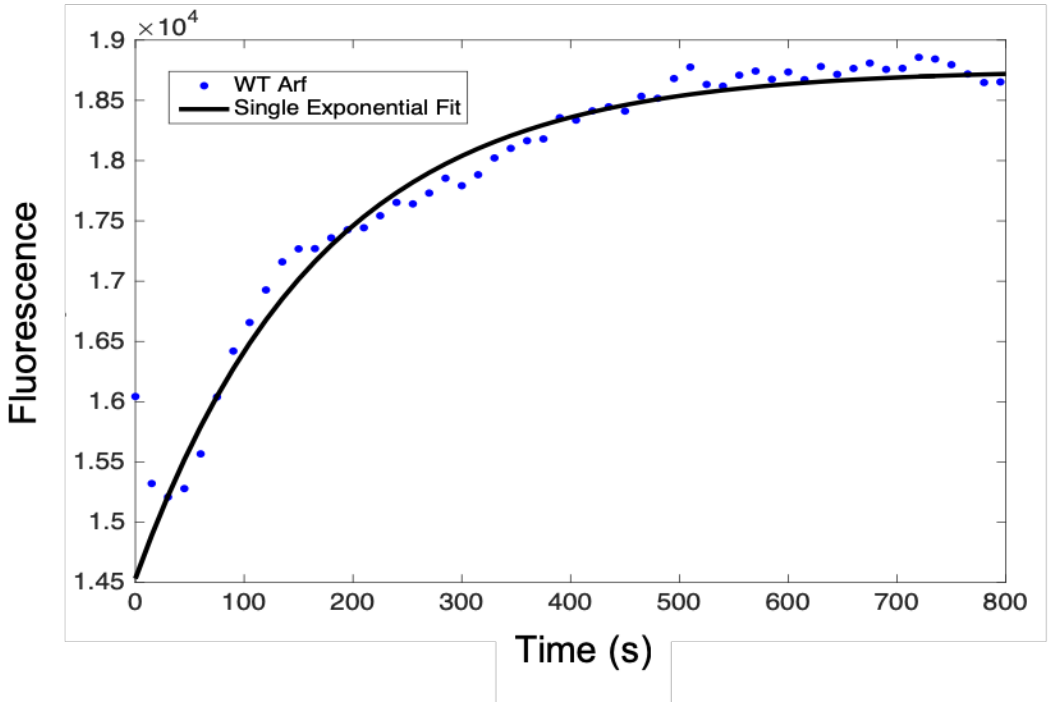

Figure 5.7: Kinetic trace for the WT Arf reaction with Gea to remove GDP from the binding site.

Mutant	Obs. Rate (10^{-2} s^{-1})
WT Arf	0.82 ± 0.02
F51C	2.5 ± 0.6
I74C	1.3 ± 0.1
L21C	1.08 ± 0.06

Table 5.1: Measured rates for WT Arf and three mutants containing nitrile probes at different positions in Arf.

5.4: Conclusions

Repeatedly creating many probe positions on Arf, ARNO, and BFA will result in an experimental electrostatic map of the binding process of BFA to the Arf/ARNO interface. These data will be coupled with a computational model already developed by our laboratory that will both guide and learn from these experiments; information from the MD model can predict useful nitrile probe locations, and information from the experiments can guide the development of computational electrostatic models of proteins. Further, this information is invaluable to the understanding of the interfacial inhibition by Brefeldin A, which is currently the best example from nature of the inhibition of the docked complex of two proteins. Any information gained about the mechanism of BFA can help guide the development of criteria to design interfacial drugs, and lend insight to how we might combat diseases that result from atypical interactions between these proteins. Furthermore, we can use the information gained from this system and apply it to other systems in the Ras superfamily, which collectively are implicated in many diseases. The successful completion of these experiments will give insight into the basic chemistry and physics of interfacial interactions of proteins, the understanding of which are crucial to designing better drugs to modulate their function.

Chapter 6: Exploring Native Mass Spectrometry as a Tool for Investigating Non-Covalent Interactions in Proteins

6.1: Introduction

Recently developed techniques in mass spectrometry have enabled the study of intact proteins in their native conformations in a manner which preserves electrostatically-bound species, making it an excellent complimentary tool to VSE spectroscopy and other investigations of non-covalent interactions in proteins.[121] Native mass spectrometry (native-MS) uses native-like aqueous buffers in well-established electrospray ionization schemes to transfer whole intact (folded) proteins or complexes into the gas phase. Mass analysis for native structures requires tandem MS techniques, and the Brodbelt group at UT Austin has pioneered the pairing of Native-MS with Ultraviolet Photodissociation (UVPD) techniques to generate robust data from an intact protein.[122] They have demonstrated that the combination of native electrospray and UVPD is capable of identifying and characterizing binding sites of substrates in protein complexes as well as determining structural changes in proteins due to mutation. What follows in this chapter are two examples of Native mass spectrometry experiments performed in collaboration with the Brodbelt group that directly inform our electrostatic experiments, and demonstrate the utility of Native MS as a crucial tool in understanding non-covalent interactions from a structural perspective. Data reported here were collected by members of the Brodbelt group from samples prepared by ETN in close collaboration and are attributed to specific individuals in the captions.

6.2: Assessing Nucleotide Binding Status in GTPase Proteins

The identity of the nucleotide bound to a GTPase dictates the signaling ON or OFF state and is associated with structural changes that affect downstream binding and

membrane affinity. Therefore, knowing which nucleotide a GTPase protein is bound to during experiments is crucial to correctly interpreting data. Contrary to practices in the field, the binding status of a GTPase protein during expression and purification cannot be assumed, but in spite of this many protocols proceed without confirming which nucleotide is bound at the time of experiment. Central to this issue is the intrinsic hydrolysis rate of GTPases. We showed in Chapter 2 that intrinsic rates vary significantly between different mutants of the same H-Ras protein.[88] Furthermore, intrinsic rates of different types of GTPases are not consistent across the Ras-superfamily. This affects nucleotide binding because, though GTP is likely more abundant in the *E. coli* cells in which the proteins are expressed, once the cells are lysed and purification begins, there is no consistent source of GTP to shift the equilibrium towards the GTP-bound state. For this reason, many published protocols have assumed that the purified protein must have then hydrolyzed all available GTP and the protein is then bound to GDP.[123]

A second challenge arises when a protocol requires exchanging the nucleotide, either to incorporate a fluorescent-tagged or radio-labeled GTP or GDP analog, or to change the portion of the catalytic cycle being measured (GTP hydrolysis and signaling vs nucleotide exchange). A variety of protocols exist to perform this task ranging from simple incubation to processing with alkaline phosphatase to remove bound nucleotide and replace it with the desired nucleotide.[124]

Because of repeated experimental challenges using published protocols, we hypothesized that the assumption of complete GTP hydrolysis during the expression and purification process was incorrect for the Arf protein we were working with. Our group was also interested in validating published protocols and comparing to our protocol for exchanging nucleotides in GTPases. Because most labeling protocols could only measure the labeled nucleotide (with fluorescence, for example) but not the percent of total protein

with the proper nucleotide incorporated, there were few protocols available for solving the particular issue of ensuring that all of our protein contained the correct nucleotide. Published protocols for establishing nucleotide binding status were based on HPLC experiments in which the protein was separated from the nucleotide by precipitating protein with ethanol, and then analyzing the nucleotide content of the supernatant.[124, 125] This protocol makes several assumptions, including that ethanol could precipitate all the protein in the sample, and that all nucleotide would remain solvated in spite of the strong electrostatic interactions holding the nucleotide to the protein. For these reasons we needed to design a better, more quantitative approach to addressing these problems.

With collaborators in the Brodbelt group, we turned to native mass spectrometry because it can maintain the non-covalent interactions binding the nucleotide and the protein together, it can distinguish between GTP and GDP by mass, and it can be performed on existing samples without further processing that could convolute results. The resulting mass spectra are shown in Figure 6.1. We demonstrated that after protein expression and purification, Arf was still bound almost entirely to GTP, even though many existing protocols operate on the assumption that the protein will have hydrolyzed GTP to GDP by the time purification is complete. Further we demonstrated that the 3x molar excess of nucleotide added in incubation protocols previously used by our group and other groups was insufficient to completely exchange all nucleotides in Arf samples. Instead, we showed that an excess of 100x molar nucleotide is required to shift the equilibrium enough to exchange the nucleotides completely. These results demonstrate the importance of confirming the relative nucleotide concentrations in GTPase protein samples, and also highlights the value of native mass spectrometry as a companion strategy for investigations involving non-covalent interactions.

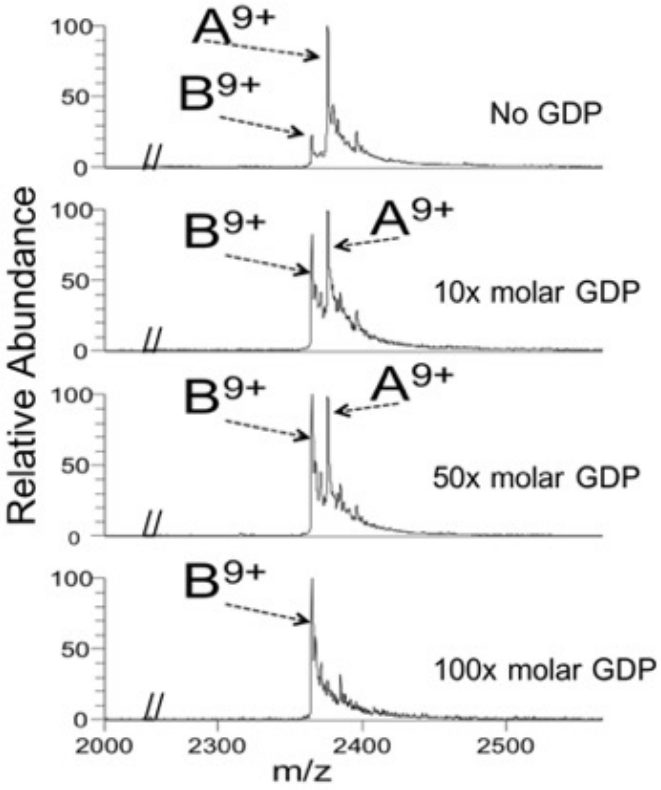

Figure 6.1: Mass spectra of natively sprayed Arf protein incubated with increasing amounts of GDP. The A state is the protein bound to GTP and the B state is the protein bound to GDP. Mass spectra collected by Ryan Parker in the Brodbelt group from samples prepared by ETN.

The top panel indicates the relative amounts of bound GTP and GDP after expression and purification when no exchange was attempted. The A state which corresponds to Arf-GTP has a significantly higher abundance than the Arf-GDP ion. This demonstrates that most of the protein after purification was still bound to GTP and therefore we cannot assume that the protein will hydrolyze GTP by the time purification is complete, contradicting many established practices. The remaining panels show the mass spectra of Arf bound to either GTP or GDP after the protein has been incubated with EDTA, dithiothreitol, and GDP for 90 min and $MgCl_2$ for an additional 30 min (our standard exchange protocol). There is not complete exchange from GTP bound Arf to GDP bound Arf until there is 100x molar excess of GDP in solution. This demonstrates that previous protocols in our group that used only 3x molar excess GDP were likely not completely exchanging the nucleotide as expected. Following this experiment, all nucleotide exchange protocols in our group were updated to reflect this new information.

This conclusion is important because it demonstrates that: 1) The assumption that all GTPases will be bound to GDP following purification is invalid, and likely different GTPases will hydrolyze GTP during purification at different rates. And 2) native ESI-UVPD MS can be used in an extremely straightforward manner to assess nucleotide binding status in the process of an experiment without separate processing, dramatically simplifying the necessary experimental procedure to verify the incorporation of the correct nucleotide.

6.3: Assessing Metal Binding Status in SNase

The unique capabilities of native-spray ESI-UVPD mass spectrometry and our mutual interest in non-covalent interactions led to a productive collaboration between the Webb and Brodbelt groups in which we investigated the metal binding status of metal-

containing proteins with mass spectrometry. Metal ions bound to proteins are crucial to many diverse biological processes.[126, 127] It is estimated that approximately 30-40% of known proteins require metal ions to stabilize their structures in the context of folding and substrate binding or to assure proper function.[128] Metals play a number of roles: 1) they act as Lewis acids, providing reactivity in catalytic processes; 2) they facilitate redox chemistry with multiple oxidation states;[126] and 3) they may coordinate multiple sites in a protein and act as cross-linking agents.[129] Deciphering all the diverse roles and identities as well as the resulting structures and functions of all metalloproteins in the human proteome remains a significant challenge.[130] In addition to the fundamental interest in understanding the biological diversity of metalloproteins, there has also been growing interest in engineered metalloproteins suitable for targeted applications such as cleanup of heavy metals from the environment or for improved photosynthetic or catalytic activity.[131, 132] In each of these cases, determining the sequences of metal binding motifs in proteins and how they contribute to the selectivity of metal recognition are key problems.

We analyzed the metal binding of SNase when bound to the native Calcium and several trivalent lanthanide atoms. The metal center and surrounding secondary structure form the oligonucleotide binding (OB) motif, conserved among many nucleases.[133, 134] It has been previously shown that the Ca^{2+} ion can be replaced with several trivalent lanthanide ions without changing the structure of the protein, though catalytic activity is halted.[52] This suggests possible applications in metal capture for environmental cleanup applications given the status of certain lanthanide elements as environmental toxins.[135, 136] Additionally, lanthanides are commonly used as luminescent substitutes for calcium ions in spectroscopy studies, as lanthanides bind with the same affinity to the same sites in proteins as calcium and have similar coordination chemistry.[137] Lanthanide ions in spectroscopy studies have utility as site-specific probes as well as acting as spectroscopic

rulers to determine the distance between lanthanide binding sites.[138] In this work we demonstrated that native electrospray mass spectrometry coupled with UVPD is capable of identifying metal binding sites in proteins in a routine manner that could potentially be applied to proteins for which crystal structures are not readily available in order to better understand and exploit protein-metal interactions.

First, we showed that the native calcium ion could be exchanged with trivalent lanthanide ions using an incubation strategy described in Chapter 2.6 and in section 6.3 above, with the exception that we found metal ion switching required 1000x molar excess in order to be observed consistently with MS. The resulting mass spectra are shown in Figure 6.2**.** We compared the apo (no metal) protein (panel A) to the native calcium bound protein (panel B) and various constructs we generated with metal ion exchange (panels C-G). The change in mass due to the incorporation of increasingly heavier metal atoms is clearly visible on the spectra, and suggests that this strategy will be useful in elucidating the identity of bound metals.

To ensure that the binding of non-native metal species did not alter the protein structure, we further validated our system by measuring the CD spectra of each construct. The resulting spectra (Figure 6.3) demonstrate that changing the identity of the metal in the binding site did not alter the secondary structure of the protein, consistent with previously published results. Further work from the Brodbelt group demonstrated that fragmentation methods using UVPD were able to deduce the location of the metal binding site by identifying residues whose fragmentation was suppressed, which was compared against the crystal structures for validation. The resulting forthcoming publication also analyzed Azurin and Calmodulin for their interactions to metals, and demonstrated that Native ESI coupled to UVPD could be used routinely to identify metal binding sites in proteins. This is important for assessing the metal binding capacity of unknown proteins

or proteins for which a crystal structure is difficult to obtain. Finding the identity of a bound metal can give clues to the function of an unknown protein. Further, there are many proteins without a solved crystal structure, such as intrinsically disordered proteins or membrane bound proteins, for which this strategy might be beneficial.

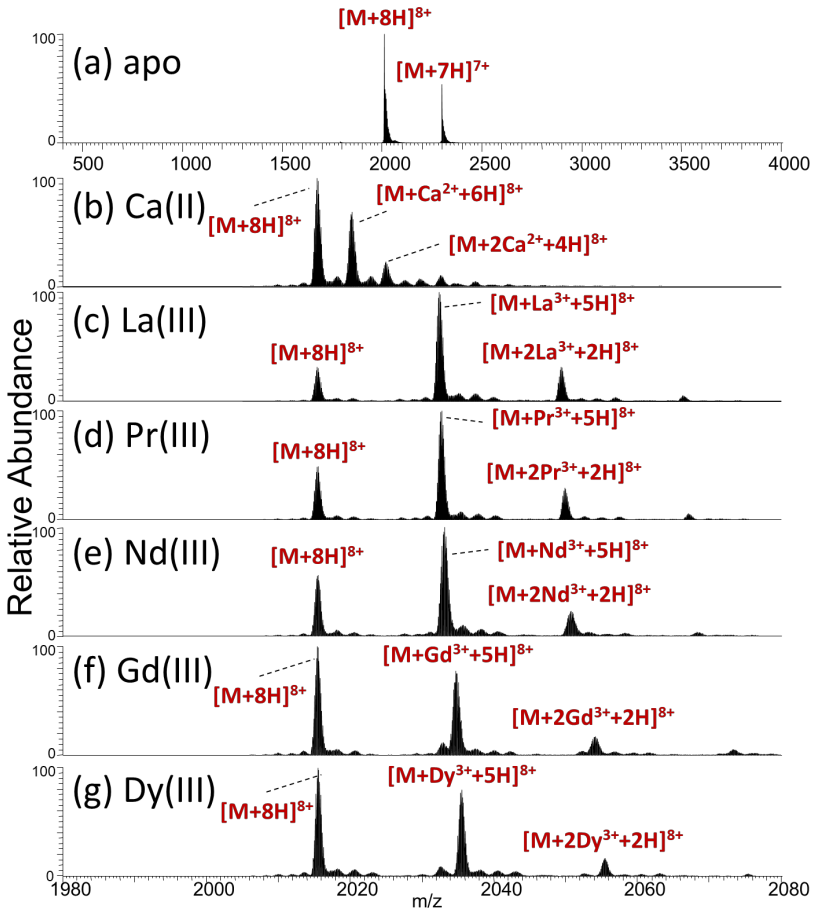

Figure 6.2: Mass spectra of SNase either without a metal in the binding site (a), bound to a native Ca^{2+} ion (b), or bound to a series of lanthanide ions (c-g). Mass spectra were collected by Dr. Christopher Crittenden in the Brodbelt group from samples prepared by ETN.

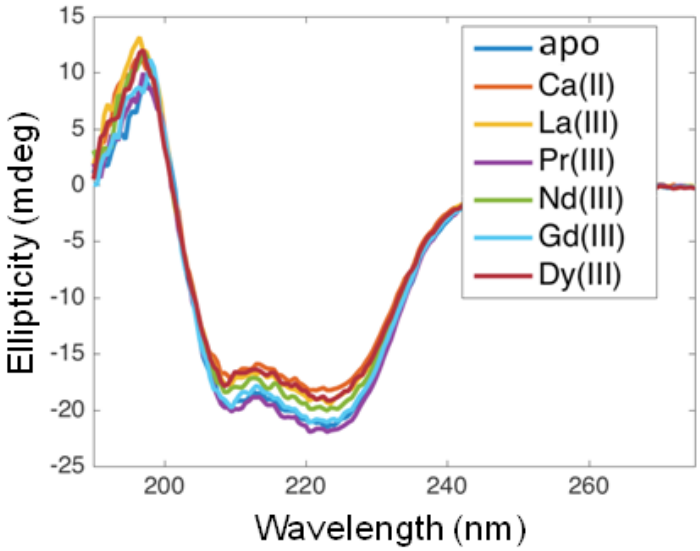

Figure 6.3: CD spectra of SNase bound to the native calcium, different lanthanide metals, and metal-free (apo). No differences were observed in the CD spectra of apo SNase compared to the metal complexes.

6.4: Conclusions and Future Work

These efforts collectively demonstrate the utility of Native ESI-UVPD MS for investigations into non-covalent interactions, particularly as complimentary experiments for spectroscopic measurements like VSE where structural changes to the system cannot be easily measured and controlled for. We showed that this method can easily identify non-covalently bound GTP or GDP in the active site of GTPases without requiring further processing or extra steps to isolate the small molecule. This suggests future experiments where it would be possible to quantify changes in the relative concentration of GTP and GDP in order to assess hydrolysis or exchange rates in these proteins. Indeed, the use of MS for enzyme kinetics is a recent development in the field made possible by improvements in MS technology.

Additionally, we showed that Native ESI-UVPD MS can reliably identify the metal binding site in proteins. In addition to the importance of this technique for assessing unknown protein structures, this methodology could be used for future experiments to evaluate how mutations to proteins alter metal binding and affect protein function. Previous work in the Brodbelt group has already demonstrated that structural changes due to mutations can be observed with MS. Assessing the electrostatic perturbations caused by these mutations and the resulting change in metal binding could be useful for learning to engineer better metalloproteins for the capture of toxic metals in the environment. Ultimately, the information available from the combination of highly detailed structural analysis with MS and the measurement of electrostatic perturbations with VSE is a powerful method for relating structure, function, and electric field in a more detailed manner than previously possible.

References

1. Honig, B.; Nicholls, A., Classical electrostatics in biology and chemistry. *Science* **1995,** *268* (5214), 1144.
2. Markley, J., Observation of histidine residues in protein by nuclear magnetic resonace spectroscopy. *Accounts of Chemical Research* **1975,** *8*, 70-80.
3. Forsyth, W. R.; Antosiewicz, J. M.; Robertson, A. D., Empirical relationships between protein structure and carboxyl pKa values in proteins. *Proteins: Structure, Function, and Genetics* **2002,** *48* (2), 388-403.
4. Langsetmo, K.; Fuchs, J. A.; Woodward, C., The conserved, buried aspartic acid in oxidized Escherichia coli thioredoxin has a pKa of 7.5. Its titration produces a related shift in global stability. *Biochemistry* **1991,** *30* (30), 7603-7609.
5. Bradbury, J. H.; Scheraga, H. A., Structural Studies of Ribonuclease. XXIV. The Application of Nuclear Magnetic Resonance Spectroscopy to Distinguish between the Histidine Residues of Ribonuclease1. *Journal of the American Chemical Society* **1966,** *88* (18), 4240-4246.
6. Isom, D. G.; Castañeda, C. A.; Cannon, B. R.; García-Moreno E, B., Large shifts in pKa values of lysine residues buried inside a protein. *Proceedings of the National Academy of Sciences* **2011,** *108* (13), 5260-5265.
7. Lockhart, D. J.; Boxer, S. G., Magnitude and direction of the change in dipole moment associated with excitation of the primary electron donor in Rhodopseudomonas sphaeroides reaction centers. *Biochemistry* **1987,** *26* (3), 664-668.
8. Lockhart, D. J.; Boxer, S. G., Stark effect spectroscopy of Rhodobacter sphaeroides and Rhodopseudomonas viridis reaction centers. *Proceedings of the National Academy of Sciences* **1988,** *85* (1), 107.

9. Lockhart, D. J.; Kirmaier, C.; Holten, D.; Boxer, S. G., Electric field effects on the initial electron-transfer kinetics in bacterial photosynthetic reaction centers. *The Journal of Physical Chemistry* **1990,** *94* (18), 6987-6995.

10. Oh, D. H.; Boxer, S. G., Electrochromism in the near-infrared absorption spectra of bridged ruthenium mixed-valence complexes. *Journal of the American Chemical Society* **1990,** *112* (22), 8161-8162.

11. Park, E. S.; Boxer, S. G., Origins of the Sensitivity of Molecular Vibrations to Electric Fields: Carbonyl and Nitrosyl Stretches in Model Compounds and Proteins. *The Journal of Physical Chemistry B* **2002,** *106* (22), 5800-5806.

12. Park, E. S.; Thomas, M. R.; Boxer, S. G., Vibrational Stark Spectroscopy of NO Bound to Heme: Effects of Protein Electrostatic Fields on the NO Stretch Frequency. *Journal of the American Chemical Society* **2000,** *122* (49), 12297-12303.

13. Pierce, D. W.; Boxer, S. G., Stark effect spectroscopy of tryptophan. *Biophys. J.* **1995,** *68* (4), 1583-1591.

14. Steffen, M. A.; Lao, K.; Boxer, S. G., Dielectric Asymmetry in the Photosynthetic Reaction Center. *Science* **1994,** *264* (5160), 810.

15. Webb, L. J.; Boxer, S. G., Electrostatic Fields Near the Active Site of Human Aldose Reductase: 1. New Inhibitors and Vibrational Stark Effect Measurements. *Biochemistry* **2008,** *47* (6), 1588-1598.

16. Andrews, S. S.; Boxer, S. G., Vibrational Stark Effects of Nitriles I. Methods and Experimental Results. *The Journal of Physical Chemistry A* **2000,** *104* (51), 11853-11863.

17. Andrews, S. S.; Boxer, S. G., Vibrational Stark Effects of Nitriles II. Physical Origins of Stark Effects from Experiment and Perturbation Models. *The Journal of Physical Chemistry A* **2002,** *106* (3), 469-477.

18. Suydam, I. T.; Boxer, S. G., Vibrational Stark Effects Calibrate the Sensitivity of Vibrational Probes for Electric Fields in Proteins. *Biochemistry* **2003,** *42* (41), 12050-12055.

19. Fried, S. D.; Boxer, S. G., Measuring Electric Fields and Noncovalent Interactions Using the Vibrational Stark Effect. *Accounts of Chemical Research* **2015,** *48* (4), 998-1006.

20. Slocum, J. D.; Webb, L. J., Measuring Electric Fields in Biological Matter Using the Vibrational Stark Effect of Nitrile Probes. *Annual Review of Physical Chemistry* **2018,** *69* (1), 253-271.

21. Chattoraj, M.; King, B. A.; Bublitz, G. U.; Boxer, S. G., Ultra-fast excited state dynamics in green fluorescent protein: multiple states and proton transfer. *Proceedings of the National Academy of Sciences* **1996,** *93* (16), 8362.

22. Bublitz, G.; King, B. A.; Boxer, S. G., Electronic Structure of the Chromophore in Green Fluorescent Protein (GFP). *Journal of the American Chemical Society* **1998,** *120* (36), 9370-9371.

23. Franzen, S.; Moore, L. J.; Woodruff, W. H.; Boxer, S. G., Stark-Effect Spectroscopy of the Heme Charge-Transfer Bands of Deoxymyoglobin. *The Journal of Physical Chemistry B* **1999,** *103* (16), 3070-3072.

24. Ludlam, C. F.; Arkin, I. T.; Liu, X. M.; Rothman, M. S.; Rath, P.; Aimoto, S.; Smith, S. O.; Engelman, D. M.; Rothschild, K. J., Fourier transform infrared spectroscopy and site-directed isotope labeling as a probe of local secondary structure in the transmembrane domain of phospholamban. *Biophys. J.* **1996,** *70* (4), 1728-1736.

25. Shrestha, R.; Cardenas, A. E.; Elber, R.; Webb, L. J., Measurement of the Membrane Dipole Electric Field in DMPC Vesicles Using Vibrational Shifts of p-Cyanophenylalanine and Molecular Dynamics Simulations. *The Journal of Physical Chemistry B* **2015,** *119* (7), 2869-2876.

26. Slocum, J. D.; Webb, L. J., Nitrile Probes of Electric Field Agree with Independently Measured Fields in Green Fluorescent Protein Even in the Presence of Hydrogen Bonding. *Journal of the American Chemical Society* **2016,** *138* (20), 6561-6570.

27. Fafarman, A. T.; Webb, L. J.; Chuang, J. I.; Boxer, S. G., Site-Specific Conversion of Cysteine Thiols into Thiocyanate Creates an IR Probe for Electric Fields in Proteins. *Journal of the American Chemical Society* **2006,** *128* (41), 13356-13357.

28. Getahun, Z.; Huang, C.-Y.; Wang, T.; De León, B.; DeGrado, W. F.; Gai, F., Using Nitrile-Derivatized Amino Acids as Infrared Probes of Local Environment. *Journal of the American Chemical Society* **2003,** *125* (2), 405-411.

29. Stafford, A. J.; Ensign, D. L.; Webb, L. J., Vibrational Stark Effect Spectroscopy at the Interface of Ras and Rap1A Bound to the Ras Binding Domain of RalGDS Reveals an Electrostatic Mechanism for Protein−Protein Interaction. *The Journal of Physical Chemistry B* **2010,** *114* (46), 15331-15344.

30. Ragain, C. M.; Newberry, R. W.; Ritchie, A. W.; Webb, L. J., Role of Electrostatics in Differential Binding of RaIGDS to Rap Mutations E30D and K31E Investigated by Vibrational Spectroscopy of Thiocyanate Probes. *Journal of Physical Chemistry B* **2012,** *116* (31), 9326-9336.

31. Walker, D. M.; Wang, R.; Webb, L. J., Conserved electrostatic fields at the Ras-effector interface measured through vibrational Stark effect spectroscopy explain the difference in tilt angle in the Ras binding domains of Raf and RalGDS. *Physical Chemistry Chemical Physics* **2014,** *16* (37), 20047-20060.

32. Stafford, A. J.; Walker, D. M.; Webb, L. J., Electrostatic Effects of Mutations of Ras Glutamine 61 Measured Using Vibrational Spectroscopy of a Thiocyanate Probe. *Biochemistry* **2012,** *51* (13), 2757-2767.

33. Shrestha, R.; Anderson, C. M.; Cardenas, A. E.; Elber, R.; Webb, L. J., Direct Measurement of the Effect of Cholesterol and 6-Ketocholestanol on the Membrane Dipole Electric Field Using Vibrational Stark Effect Spectroscopy Coupled with Molecular Dynamics Simulations. *The Journal of Physical Chemistry B* **2017,** *121* (15), 3424-3436.

34. Ritchie, A. W.; Webb, L. J., Optimizing Electrostatic Field Calculations with the Adaptive Poisson–Boltzmann Solver to Predict Electric Fields at Protein–Protein Interfaces II: Explicit Near-Probe and Hydrogen-Bonding Water Molecules. *The Journal of Physical Chemistry B* **2014,** *118* (28), 7692-7702.

35. Ritchie, A. W.; Webb, L. J., Understanding and Manipulating Electrostatic Fields at the Protein–Protein Interface Using Vibrational Spectroscopy and Continuum Electrostatics Calculations. *The Journal of Physical Chemistry B* **2015,** *119* (44), 13945-13957.

36. Adhikary, R.; Zimmermann, J.; Dawson, P. E.; Romesberg, F. E., IR Probes of Protein Microenvironments: Utility and Potential for Perturbation. *ChemPhysChem* **2014,** *15* (5), 849-853.

37. Fafarman, A. T.; Sigala, P. A.; Herschlag, D.; Boxer, S. G., Decomposition of Vibrational Shifts of Nitriles into Electrostatic and Hydrogen-Bonding Effects. *Journal of the American Chemical Society* **2010,** *132* (37), 12811-12813.

38. Zhang, W.; Markiewicz, B. N.; Doerksen, R. S.; Smith, I. I. I. A. B.; Gai, F., CN stretching vibration of 5-cyanotryptophan as an infrared probe of protein local environment: what determines its frequency? *Physical Chemistry Chemical Physics* **2016,** *18* (10), 7027-7034.

39. Colicelli, J., Human RAS superfamily proteins and related GTPases. *Science's STKE: signal transduction knowledge environment* **2004,** *2004* (250), RE13.

40. Wennerberg, K.; Rossman, K. L.; Der, C. J., The Ras superfamily at a glance. *Journal of Cell Science* **2005,** *118* (5), 843.

41. Bokoch, G. M.; Der, C. J., Emerging concepts in the Ras superfamily of GTP-binding proteins. *The FASEB Journal* **1993,** *7* (9), 750-759.

42. Huang, L.; Hofer, F.; Martin, G. S.; Kim, S. H., Structural basis for the interaction of Ras with RalGDS. *Nature structural biology* **1998,** *5* (6), 422-6.

43. Vigil, D.; Cherfils, J.; Rossman, K. L.; Der, C. J., Ras superfamily GEFs and GAPs: validated and tractable targets for cancer therapy? *Nature Reviews Cancer* **2010,** *10*, 842.

44. Prior, I. A.; Lewis, P. D.; Mattos, C., A Comprehensive Survey of Ras Mutations in Cancer. *Cancer Research* **2012,** *72* (10), 2457-2467.

45. Fernández-Medarde, A.; Santos, E., Ras in cancer and developmental diseases. *Genes & cancer* **2011,** *2* (3), 344-358.

46. Cox, A. D.; Fesik, S. W.; Kimmelman, A. C.; Luo, J.; Der, C. J., Drugging the undruggable RAS: Mission Possible? *Nature Reviews Drug Discovery* **2014,** *13*, 828.

47. Chen, J.; Lu, Z.; Sakon, J.; Stites, W. E., Increasing the thermostability of staphylococcal nuclease: implications for the origin of protein thermostability11Edited by J. A. Wells. *Journal of Molecular Biology* **2000,** *303* (2), 125-130.

48. García-Moreno, B. E.; Dwyer, J. J.; Gittis, A. G.; Lattman, E. E.; Spencer, D. S.; Stites, W. E., Experimental measurement of the effective dielectric in the hydrophobic core of a protein. *Biophysical chemistry* **1997,** *64* (1-3), 211-224.

49. Cuatrecasas, P.; Fuchs, S.; Anfinsen, C. B., Catalytic properties and specificity of the extracellular nuclease of Staphylococcus aureus. *Journal of Biological Chemistry* **1967,** *242* (7), 1541-1547.

50. Heins, J. N.; Suriano, J. R.; Taniuchi, H.; Anfinsen, C. B., Characterization of a Nuclease Produced by Staphylococcus aureus. *Journal of Biological Chemistry* **1967,** *242* (5), 1016-1020.

51. Castaneda, C. A.; Fitch, C. A.; Majumdar, A.; Khangulov, V.; Schlessman, J. L.; García-Moreno, B. E., Molecular determinants of the pKa values of Asp and Glu residues in staphylococcal nuclease. *Proteins: Structure, Function, and Bioinformatics* **2009,** *77* (3), 570-588.

52. Furie, B.; Eastlake, A.; Schechter, A. N.; Anfinsen, C. B., The interaction of the lanthanide ions with staphylococcal nuclease. *Journal of Biological Chemistry* **1973,** *248* (16), 5821-5825.

53. Flynn, R. L.; Zou, L., Oligonucleotide/oligosaccharide-binding fold proteins: a growing family of genome guardians. *Critical Reviews in Biochemistry and Molecular Biology* **2010,** *45* (4), 266-275.

54. Nielsen, J. E.; Gunner, M.; García-Moreno, E., The pKa Cooperative: A collaborative effort to advance structure-based calculations of pKa values and electrostatic effects in proteins. *Proteins: Structure, Function, and Bioinformatics* **2011,** *79* (12), 3249-3259.

55. Tropea, J. E.; Cherry, S.; Waugh, D. S., Expression and Purification of Soluble His6-Tagged TEV Protease. In *High Throughput Protein Expression and Purification: Methods and Protocols*, Doyle, S. A., Ed. Humana Press: Totowa, NJ, 2009; pp 297-307.

56. Quan, A.; Robinson, P. J., Rapid Purification of Native Dynamin I and Colorimetric GTPase Assay. In *Methods in Enzymology*, Academic Press: 2005; Vol. 404, pp 556-569.

57. Bourne, H. R.; Sanders, D. A.; McCormick, F., The GTPase superfamily: conserved structure and molecular mechanism. *Nature* **1991,** *349* (6305), 117-127.

58. Cherfils, J.; Zeghouf, M., Regulation of Small GTPases by GEFs, GAPs, and GDIs. *Physiological Reviews* **2013,** *93* (1), 269-309.

59. Khrenova, M. G.; Grigorenko, B. L.; Kolomeisky, A. B.; Nemukhin, A. V., Hydrolysis of Guanosine Triphosphate (GTP) by the Ras·GAP Protein Complex: Reaction Mechanism and Kinetic Scheme. *The Journal of Physical Chemistry B* **2015,** *119* (40), 12838-12845.

60. Cox, A. D.; Der, C. J., The dark side of Ras: regulation of apoptosis. *Oncogene* **2003,** *22*, 8999.

61. Downward, J., Targeting RAS signalling pathways in cancer therapy. *Nature Reviews Cancer* **2003,** *3*, 11.

62. Repasky, G. A.; Chenette, E. J.; Der, C. J., Renewing the conspiracy theory debate: does Raf function alone to mediate Ras oncogenesis? *Trends in Cell Biology* **2004,** *14* (11), 639-647.

63. Shields, J. M.; Pruitt, K.; McFall, A.; Shaub, A.; Der, C. J., Understanding Ras: 'it ain't over 'til it's over'. *Trends in Cell Biology* **2000,** *10* (4), 147-154.

64. Harvey, J. J., An Unidentified Virus which causes the Rapid Production of Tumours in Mice. *Nature* **1964,** *204* (4963), 1104-1105.

65. Bos, J. L., Ras Oncogenes in Human Cancer: A Review. *Cancer Research* **1989,** *49* (17), 4682.

66. Eccleston, J. F.; Moore, K. J.; Morgan, L.; Skinner, R. H.; Lowe, P. N., Kinetics of interaction between normal and proline 12 Ras and the GTPase-activating proteins, p120-GAP and neurofibromin. The significance of the intrinsic GTPase rate in determining the transforming ability of ras. *Journal of Biological Chemistry* **1993,** *268* (36), 27012-27019.

67. Hobbs, G. A.; Der, C. J.; Rossman, K. L., RAS isoforms and mutations in cancer at a glance. *Journal of Cell Science* **2016,** *129* (7), 1287.

68. Carvalho, A. T. P.; Szeler, K.; Vavitsas, K.; Åqvist, J.; Kamerlin, S. C. L., Modeling the mechanisms of biological GTP hydrolysis. *Archives of Biochemistry and Biophysics* **2015,** *582*, 80-90.

69. Kamerlin, S. C. L.; Sharma, P. K.; Prasad, R. B.; Warshel, A., Why nature really chose phosphate. *Quarterly Reviews of Biophysics* **2013,** *46* (1), 1-132.

70. Pai, E. F.; Krengel, U.; Petsko, G. A.; Goody, R. S.; Kabsch, W.; Wittinghofer, A., Refined crystal structure of the triphosphate conformation of H-ras p21 at 1.35 A resolution: implications for the mechanism of GTP hydrolysis. **1990,** *9* (8), 2351-2359.

71. Langen, R.; Schweins, T.; Warshel, A., On the mechanism of guanosine triphosphate hydrolysis in ras p21 proteins. *Biochemistry* **1992,** *31* (37), 8691-6.

72. Shurki, A.; Warshel, A., Why does the Ras switch "break" by oncogenic mutations? *Proteins: Structure, Function, and Bioinformatics* **2004,** *55* (1), 1-10.

73. Scheffzek, K.; Ahmadian, M. R.; Kabsch, W.; Wiesmüller, L.; Lautwein, A.; Schmitz, F.; Wittinghofer, A., The Ras-RasGAP complex: structural basis for GTPase activation and its loss in oncogenic Ras mutants. *Science* **1997,** *277* (5324), 333-339.

74. Schweins, T.; Geyer, M.; Scheffzek, K.; Warshel, A.; Kalbitzer, H. R.; Wittinghofer, A., Substrate-assisted catalysis as a mechanism for GTP hydrolysis of p21ras and other GTP-binding proteins. *Nature structural biology* **1995,** *2* (1), 36-44.

75. Grigorenko, B. L.; Nemukhin, A. V.; Topol, I. A.; Cachau, R. E.; Burt, S. K., QM/MM modeling the Ras–GAP catalyzed hydrolysis of guanosine triphosphate. *Proteins: Structure, Function, and Bioinformatics* **2005,** *60* (3), 495-503.

76. Vogel, U. S.; Dixon, R. A. F.; Schaber, M. D.; Diehl, R. E.; Marshall, M. S.; Scolnick, E. M.; Sigal, I. S.; Gibbs, J. B., Cloning of bovine GAP and its interaction with oncogenic ras p21. *Nature* **1988,** *335* (6185), 90-93.

77. Buhrman, G.; Holzapfel, G.; Fetics, S.; Mattos, C., Allosteric modulation of Ras positions Q61 for a direct role in catalysis. *Proceedings of the National Academy of Sciences* **2010,** *107* (11), 4931-4936.

78. Buhrman, G.; Wink, G.; Mattos, C., Transformation Efficiency of RasQ61 Mutants Linked to Structural Features of the Switch Regions in the Presence of Raf. *Structure* **2007,** *15* (12), 1618-1629.

79. Buhrman, G.; Kumar, V. S. S.; Cirit, M.; Haugh, J. M.; Mattos, C., Allosteric Modulation of Ras-GTP Is Linked to Signal Transduction through RAF Kinase. **2011,** *286* (5), 3323-3331.

80. Oh, K.-I.; Choi, J.-H.; Lee, J.-H.; Han, J.-B.; Lee, H.; Cho, M., Nitrile and thiocyanate IR probes: Molecular dynamics simulation studies. *The Journal of chemical physics* **2008,** *128* (15), 154504.

81. Waegele, M. M.; Tucker, M. J.; Gai, F., 5-Cyanotryptophan as an infrared probe of local hydration status of proteins. *Chemical Physics Letters* **2009,** *478* (4), 249-253.

82. Der, C. J.; Finkel, T.; Cooper, G. M., Biological and biochemical properties of human rasH genes mutated at codon 61. *Cell* **1986,** *44* (1), 167-176.

83. Krengel, U.; Schlichting, I.; Scherer, A.; Schumann, R.; Frech, M.; John, J.; Kabsch, W.; Pai, E. F.; Wittinghofer, A., Three-dimensional structures of H-ras p21 mutants: Molecular basis for their inability to function as signal switch molecules. *Cell* **1990,** *62* (3), 539-548.

84. Frech, M.; Darden, T.; Pedersen, L.; Foley, C.; Charifson, P.; Anderson, M.; Wittinghofer, A., Role of glutamine-61 in the hydrolysis of GTP by p21H-ras: an experimental and theoretical study. *Biochemistry* **1994,** *33* (11), 3237-3244.

85. Johnson, K. A.; Goody, R. S., The Original Michaelis Constant: Translation of the 1913 Michaelis–Menten Paper. *Biochemistry* **2011,** *50* (39), 8264-8269.

86. Michaelis, L.; Menten, M. L., Die Kinetik der Invertinwirkung. *Biochemische Zeitschrift* **1913,** *49*, 333-369.

87. John, J.; Frech, M.; Wittinghofer, A., Biochemical properties of Ha-ras encoded p21 mutants and mechanism of the autophosphorylation reaction. *Journal of Biological Chemistry* **1988,** *263* (24), 11792-11799.

88. Novelli, E. T.; First, J. T.; Webb, L. J., Quantitative Measurement of Intrinsic GTP Hydrolysis for Carcinogenic Glutamine 61 Mutants in H-Ras. *Biochemistry* **2018,** *57* (44), 6356-6366.

89. Choi, J.-H.; Oh, K.-I.; Lee, H.; Lee, C.; Cho, M., Nitrile and thiocyanate IR probes: Quantum chemistry calculation studies and multivariate least-square fitting analysis. **2008,** *128* (13), 134506.

90. First, J. T.; Slocum, J. D.; Webb, L. J., Quantifying the Effects of Hydrogen Bonding on Nitrile Frequencies in GFP: Beyond Solvent Exposure. *The Journal of Physical Chemistry B* **2018,** *122* (26), 6733-6743.

91. Slocum, J. D.; First, J. T.; Webb, L. J., Orthogonal Electric Field Measurements near the Green Fluorescent Protein Fluorophore through Stark Effect Spectroscopy and pKa Shifts Provide a Unique Benchmark for Electrostatics Models. *The Journal of Physical Chemistry B* **2017,** *121* (28), 6799-6812.

92. Wolfenden, R.; Andersson, L.; Cullis, P. M.; Southgate, C. C., Affinities of amino acid side chains for solvent water. *Biochemistry* **1981,** *20* (4), 849-855.

93. Warshel, A., Energetics of enzyme catalysis. *Proceedings of the National Academy of Sciences* **1978,** *75* (11), 5250.

94. Isom, D. G.; Castañeda, C. A.; Cannon, B. R.; Velu, P. D.; García-Moreno E, B., Charges in the hydrophobic interior of proteins. *Proceedings of the National Academy of Sciences* **2010,** *107* (37), 16096-16100.

95. Isom, D. G.; Cannon, B. R.; Castañeda, C. A.; Robinson, A.; García-Moreno E, B., High tolerance for ionizable residues in the hydrophobic interior of proteins. *Proceedings of the National Academy of Sciences* **2008,** *105* (46), 17784-17788.

96. Grimsley, G. R.; Scholtz, J. M.; Pace, C. N., A summary of the measured pK values of the ionizable groups in folded proteins. *Protein Science* **2009,** *18* (1), 247-251.

97. Harms, M. J.; Schlessman, J. L.; Sue, G. R.; García-Moreno E, B., Arginine residues at internal positions in a protein are always charged. *Proceedings of the National Academy of Sciences* **2011,** *108* (47), 18954-18959.

98. Alexov, E.; Mehler, E. L.; Baker, N.; M Baptista, A.; Huang, Y.; Milletti, F.; Erik Nielsen, J.; Farrell, D.; Carstensen, T.; Olsson, M. H., Progress in the prediction of pKa values in proteins. *Proteins: structure, function, and bioinformatics* **2011,** *79* (12), 3260-3275.

99. Liu, J.; Swails, J.; Zhang, J. Z. H.; He, X.; Roitberg, A. E., A Coupled Ionization-Conformational Equilibrium Is Required To Understand the Properties of Ionizable Residues in the Hydrophobic Interior of Staphylococcal Nuclease. *Journal of the American Chemical Society* **2018,** *140* (5), 1639-1648.

100. Arthur, E. J.; Yesselman, J. D.; Brooks, C. L., Predicting extreme pKa shifts in staphylococcal nuclease mutants with constant pH molecular dynamics. *Proteins: Structure, Function, and Bioinformatics* **2011,** *79* (12), 3276-3286.

101. McMahon, H. A.; Alfieri, K. N.; Clark, K. A. A.; Londergan, C. H., Cyanylated Cysteine: A Covalently Attached Vibrational Probe of Protein−Lipid Contacts. *The Journal of Physical Chemistry Letters* **2010,** *1* (5), 850-855.

102. Walker, D. M.; Hayes, E. C.; Webb, L. J., Vibrational Stark effect spectroscopy reveals complementary electrostatic fields created by protein-protein binding at the interface of Ras and Ral. *Physical Chemistry Chemical Physics* **2013,** *15* (29), 12241-12252.

103. Johnson, M. N. R.; Londergan, C. H.; Charkoudian, L. K., Probing the Phosphopantetheine Arm Conformations of Acyl Carrier Proteins Using Vibrational Spectroscopy. *Journal of the American Chemical Society* **2014,** *136* (32), 11240-11243.

104. Kirshenbaum, K.; Carrico, I. S.; Tirrell, D. A., Biosynthesis of Proteins Incorporating a Versatile Set of Phenylalanine Analogues. *ChemBioChem* **2002,** *3* (2-3), 235-237.

105. Fafarman, A. T.; Boxer, S. G., Nitrile Bonds as Infrared Probes of Electrostatics in Ribonuclease S. *The Journal of Physical Chemistry B* **2010,** *114* (42), 13536-13544.

106. Simonson, T.; Carlsson, J.; Case, D. A., Proton Binding to Proteins: pKa Calculations with Explicit and Implicit Solvent Models. *Journal of the American Chemical Society* **2004,** *126* (13), 4167-4180.

107. Adhikary, R.; Zimmermann, J.; Dawson, P. E.; Romesberg, F. E., Temperature Dependence of CN and SCN IR Absorptions Facilitates Their Interpretation and Use as Probes of Proteins. *Analytical Chemistry* **2015,** *87* (22), 11561-11567.

108. Dippel, A. B. O., Gregory M.; Maurici, Nicole; Liskov, Melanie T.; Brewer, Scott H.; Phillips-Piro, Chrisitne M., Probing the effectiveness of spectroscopic reporter unnatural amino acids: a structural study. *Acta Crystallographica Section D* **2016,** *72*, 121-130.

109. Harms, M. J.; Castañeda, C. A.; Schlessman, J. L.; Sue, G. R.; Isom, D. G.; Cannon, B. R.; García-Moreno E, B., The pKa Values of Acidic and Basic Residues Buried at the Same Internal Location in a Protein Are Governed by Different Factors. *Journal of Molecular Biology* **2009,** *389* (1), 34-47.

110. Robinson, A. C.; Schlessman, J. L.; García-Moreno E, B., Dielectric Properties of a Protein Probed by Reversal of a Buried Ion Pair. *The Journal of Physical Chemistry B* **2018,** *122* (9), 2516-2524.

111. Wennerberg, K.; Rossman, K. L.; Der, C. J., The Ras superfamily at a glance. *Journal of Cell Science* **2005,** *118* (5), 843-846.

112. Peyroche, A.; Jackson, C. L., Functional analysis of ADP-ribosylation factor (ARF) guanine nucleotide exchange factors Gea1p and Gea2p in yeast. *Regulators and Effectors of Small Gtpases, Pt E* **2001,** *329*, 290-300.

113. Kahn, R. A., The protein cofactor necessary for ADP-ribosylation of Gs by cholera toxin is itself a GTP binding protein. *The Journal of biological chemistry* **1986,** *261* (17), 7906.

114. Jackson, C. L.; Casanova, J. E., Turning on ARF: the Sec7 family of guanine-nucleotide-exchange factors. *Trends in Cell Biology* **2000,** *10* (2), 60-67.

115. Antonny, B.; Beraud-Dufour, S.; Chardin, P.; Chabre, M., N-Terminal Hydrophobic Residues of the G-Protein ADP-Ribosylation Factor-1 Insert into Membrane Phospholipids upon GDP to GTP Exchange. *Biochemistry* **1997,** *36* (15), 4675-4684.

116. Liu, Y.; Kahn, R. A.; Prestegard, J. H., Dynamic structure of membrane-anchored Arf•GTP. *Nature Structural & Molecular Biology* **2010,** *17*, 876.

117. Renault, L.; Guibert, B.; Cherfils, J., Structural snapshots of the mechanism and inhibition of a guanine nucleotide exchange factor. *Nature* **2003,** *426* (6966), 525-530.

118. Pommier, Y.; Cherfils, J., Interfacial inhibition of macromolecular interactions: nature's paradigm for drug discovery. *Trends in Pharmacological Sciences* **2005,** *26* (3), 138-145.

119. Peyroche, A.; Antonny, B.; Robineau, S.; Acker, J.; Cherfils, J.; Jackson, C. L., Brefeldin A Acts to Stabilize an Abortive ARF–GDP–Sec7 Domain Protein Complex: Involvement of Specific Residues of the Sec7 Domain. *Molecular Cell* **1999,** *3* (3), 275-285.

120. Zeeh, J. C.; Zeghouf, M.; Grauffel, C.; Guibert, B.; Martin, E.; Dejaegere, A.; Cherfils, J., Dual specificity of the interfacial inhibitor brefeldin A for Arf proteins and Sec7 domains. *Journal of Biological Chemistry* **2006,** *281* (17), 11805-11814.

121. O'Brien, J. P.; Li, W.; Zhang, Y.; Brodbelt, J. S., Characterization of Native Protein Complexes Using Ultraviolet Photodissociation Mass Spectrometry. *Journal of the American Chemical Society* **2014,** *136* (37), 12920-12928.

122. Brodbelt, J. S., Photodissociation mass spectrometry: new tools for characterization of biological molecules. *Chemical Society Reviews* **2014,** *43* (8), 2757-2783.

123. Zeeh, J. C.; Antonny, B.; Cherfils, J.; Zeghouf, M., In Vitro Assays to Characterize Inhibitors of the Activation of Small G Proteins by Their Guanine Nucleotide Exchange Factors. In *Methods in Enzymology*, William E. Balch, C. J. D.; Alan, H., Eds. Academic Press: 2008; Vol. Volume 438, pp 41-56.

124. Smith, S. J. M.; Rittinger, K., Preparation of GTPases for Structural and Biophysical Analysis. In *GTPase Protocols: The Ras Superfamily*, Manser, E.; Leung, T., Eds. Springer New York: Totowa, NJ, 2002; pp 13-24.

125. Rubio, I.; Pusch, R.; Wetzker, R., Quantification of absolute Ras-GDP/GTP levels by HPLC separation of Ras-bound [32P]-labelled nucleotides. *Journal of Biochemical and Biophysical Methods* **2004,** *58* (2), 111-117.

126. Liu, J.; Chakraborty, S.; Hosseinzadeh, P.; Yu, Y.; Tian, S.; Petrik, I.; Bhagi, A.; Lu, Y., Metalloproteins Containing Cytochrome, Iron–Sulfur, or Copper Redox Centers. *Chemical Reviews* **2014,** *114* (8), 4366-4469.

127. Shi, W.; Chance, M. R., Metallomics and metalloproteomics. *Cellular and Molecular Life Sciences* **2008,** *65* (19), 3040-3048.

128. Shi, W.; Chance, M. R., Metalloproteomics: forward and reverse approaches in metalloprotein structural and functional characterization. *Current Opinion in Chemical Biology* **2011,** *15* (1), 144-148.

129. Chou, C.-C.; Martin-Martinez, F. J.; Qin, Z.; Dennis, P. B.; Gupta, M. K.; Naik, R. R.; Buehler, M. J., Ion Effect and Metal-Coordinated Cross-Linking for Multiscale Design of Nereis Jaw Inspired Mechanomutable Materials. *ACS Nano* **2017,** *11* (2), 1858-1868.

130. Andreini, C.; Bertini, I.; Rosato, A., Metalloproteomes: A Bioinformatic Approach. *Accounts of Chemical Research* **2009,** *42* (10), 1471-1479.

131. Waldron, K. J.; Robinson, N. J., How do bacterial cells ensure that metalloproteins get the correct metal? *Nature Reviews Microbiology* **2009,** *7* (1), 25-35.

132. Lu, Y.; Yeung, N.; Sieracki, N.; Marshall, N. M., Design of functional metalloproteins. *Nature* **2009,** *460* (7257), 855-862.

133. Theobald, D. L.; Mitton-Fry, R. M.; Wuttke, D. S., Nucleic Acid Recognition by OB-Fold Proteins. *Annual Review of Biophysics and Biomolecular Structure* **2003,** *32* (1), 115-133.

134. Arcus, V., OB-fold domains: a snapshot of the evolution of sequence, structure and function. *Current Opinion in Structural Biology* **2002,** *12* (6), 794-801.

135. Pagano, G.; Aliberti, F.; Guida, M.; Oral, R.; Siciliano, A.; Trifuoggi, M.; Tommasi, F., Rare earth elements in human and animal health: State of art and research priorities. *Environmental Research* **2015,** *142*, 215-220.

136. Cook, E. C.; Featherston, E. R.; Showalter, S. A.; Cotruvo, J. A., Structural Basis for Rare Earth Element Recognition by Methylobacterium extorquens Lanmodulin. *Biochemistry* **2019,** *58* (2), 120-125.

137. Brittain, H. G.; Richardson, F. S.; Martin, R. B., Terbium (III) emission as a probe of calcium(II) binding sites in proteins. *Journal of the American Chemical Society* **1976,** *98* (25), 8255-8260.

138. Kilhoffer, M.-C.; Demaille, J. G.; Gerard, D., Terbium as luminescent probe of calmodulin calcium-binding sites. **1980,** *116* (2), 269-272.